

A method to couple non-conforming finite element meshes

**submitted as doctoral dissertation for obtaining the
academic degree of doctor of technical sciences at the
Graz University of Technology**

by

Gebhard Josef Wallinger

**Supervisor/First reviewer: Prof. Oszkár Bíró
Second reviewer: Prof. Herbert de Gersem**

Graz, 2019

Acknowledgements

This work has been developed during the past five years along my lecturing work at the Institute of Fundamentals and Theory in Electrical Engineering at the Graz University of Technology. I would like to take the opportunity to thank all my companions who have helped me and inspired me during this time.

First, I would like to thank Prof. Oszkár Bíró for his constructive guidance, extensive expertise and feedback during the last years. Beside that I am thankful for the opportunities and free space provided to gather experiences in different fields of expertise.

My deepest thanks go to my colleagues at the Institute of Fundamentals and Theory in Electrical Engineering. Without them, it would have been half as fun and inspiring to work. Thank you again for the friendly working environment and for turning the past years into an unforgettable time.

I also have to thank my friends who have accompanied me beside my work. They have not only supported me in sports activities, they have also created a place of retreat and excellent environment to recover.

Finally, I would like to thank my parents Aloisia and Franz Wallinger for enabling me this career and for their continuous support. Additionally, I would like to thank also my sister and brother for their support and stimulating discussions.

In the end, I wish to thank Lydia for her patience, trust in my work and me, love and moral support during the last years. This thesis is dedicated to her and our still unborn child.

“In tranquillitate vis!”

Abstract

In the design process of electromechanical devices today, the requirements on appropriate design tools are increasing. Due to the high precision and increased level of model complexity, numerical simulations with the aid of the finite element method are indispensable for such design processes. The ability to couple two domains where either the overall mesh becomes non-conforming through independent mesh topologies or relative movement between the two domains is a prerequisite in modern software packages. Treating the relative movement is still a hot topic and a challenging task, especially if three-dimensional models are considered. This thesis presents a finite element method to couple two disjoint domains with independent meshes that are allowed to become non-conforming along the coupling surface.

The investigated non-conforming mesh method is based on an interpolation technique in the sense of a master/slave principle. The degrees of freedom associated with slave nodes that are defined along the coupling interface become interpolated by those of the corresponding master nodes. As this non-conforming mesh method introduces no additional unknowns to the resulting equation system, the advantages of the finite element method are preserved. The application to various three dimensional problems, ranging from static domain coupling to time transient analysis of motion induction, verifies this and demonstrates the reliability of the non-conforming mesh method. Compared to reference methods, the non-conforming mesh method achieves high accuracy and good agreement with results obtained otherwise.

By means of detailed error and accuracy analyses, the limits of the method are addressed and improvements are made. Regarding these limits, a guideline for the appropriate use of the non-conforming mesh method is developed.

Keywords: eddy current, electromagnetic modelling, finite element method, interpolation technique, motion induction, non-conforming mesh, sliding surface

Kurzfassung

Heutzutage stellt die fortschreitende Entwicklung von elektromechanischen Geräten immer größer werdende Anforderungen an entsprechende Entwicklungspakete. Im speziellen sind numerische Simulationen mit Hilfe der Finiten-Elemente-Methode durch die geforderte Genauigkeit und Komplexität der Modelle vom Entwicklungsprozess nicht mehr wegzudenken. Die Kopplung zweier Problemgebiete wo entweder durch unterschiedliche Diskretisierung oder durch relative Bewegung zwischen den Gebieten das gesamte finite Elementgitter nicht konform wird, ist mittlerweile eine standardisierte Anforderung an entsprechende Softwarepakete. Besonders herausfordernd ist der Fall der relativen Bewegung, vor allem wenn dreidimensionale Modelle berücksichtigt werden müssen. In dieser Arbeit wird eine Finite-Elemente-Methode präsentiert, welche die Kopplung zweier unabhängiger Problemgebiete behandelt. Hierbei ist es erlaubt, dass die zugehörigen Elementgitter entlang einer Kopplungsfläche nicht konform werden.

Der vorgestellten Methode liegt eine Interpolationsmethode im Sinne eines Master/Slave-Prinzips zugrunde. Es werden hierbei die Freiheitsgrade der Slave-Knoten, welche entlang der Kopplungsfläche definiert wurden, mit jenen Freiheitsgraden der Master-Knoten interpoliert. Da bei dieser Methode keine weiteren unbekannt Variablen, welche im Gleichungssystem berücksichtigt werden müssen, eingeführt werden, bleiben die Vorteile der Finiten-Elemente-Methode erhalten. Die Erhaltung dessen wurde durch Anwendung auf Probleme hinsichtlich rein statischer Gebietskopplung oder zeitabhängiger Analyse der Bewegungsinduktion bestätigt. Im Weiteren konnte die Zuverlässigkeit, sowie die Genauigkeit der Methode im Vergleich mit Referenzmethoden gezeigt werden.

Mit Hilfe der durchgeführten Fehleranalysen und Genauigkeitsanalysen konnten die Grenzen der Methode aufgezeigt und Verbesserungen durchgeführt werden. Im Anbetracht der ermittelten Grenzen lässt sich ein Leitfaden zur Anwendung der vorgestellten Methode ableiten.

Schlagwörter: Wirbelströme, elektromagnetische Modellierung, finite Elemente Methode, Interpolationsmethode, Bewegungsinduktion, nicht konforme Elementgitter, Bewegungsfläche/Kopplungsfläche

Statutory Declaration

I declare that I have authored this thesis independently, that I have not used other than the declared sources/resources and that I have explicitly marked all material, which has been quoted either literally or by content from the used sources. The text document uploaded to TUGRAZonline is identical to the present doctoral dissertation.

Eidesstattliche Erklärung

Ich erkläre an Eides statt, dass ich die vorliegende Arbeit selbstständig verfasst, andere als die angegebenen Quellen/Hilfsmittel nicht benutzt und die den benutzten Quellen wörtlich und inhaltlich entnommenen Stellen als solche kenntlich gemacht habe. Das in TUGRAZonline hochgeladene Textdokument ist mit der vorliegenden Dissertation identisch.

Graz,

.....

Signature

Contents

1	Introduction	1
1.1	Aim of the work	3
1.2	Scientific contributions	4
1.3	Structure of the work	5
2	Review of relevant research work	6
2.1	Traditional methods	7
2.2	Modern methods	8
2.3	Conclusion	11
3	Fundamentals	12
3.1	Electromagnetic field	13
3.1.1	<i>Maxwell's equations</i>	13
3.1.2	<i>Faraday's law of induction</i>	14
3.2	Problem definitions	17
3.2.1	<i>Magneto-static problem</i>	17
3.2.2	<i>Quasi-static eddy current problem</i>	18
3.3	Method of weighted residuals	20
3.4	Space discretization using finite elements	23
3.5	Time discretization	28
3.6	A potential formulation for magneto-static problems	29
3.7	Potential formulations for eddy current problems	31
3.7.1	<i>A, V-A formulation</i>	31
3.7.2	<i>T, Φ-Φ formulation</i>	32
4	Non-conforming mesh connection method	34
4.1	Coupling of nodes/potentials	34
4.2	Reformulating the Galerkin equations of the magneto-static field problem	38
4.3	Error analysis	41
4.4	Periodic boundary condition	50
5	Taking account of motion	54
5.1	Problem definition	54
5.1.1	<i>Motional eddy currents – stationary framework</i>	54
5.1.2	<i>Motional eddy currents – moving framework</i>	55
5.1.3	<i>T, Φ-Φ formulation for motional eddy currents</i>	56
5.2	Accuracy analysis	59
5.2.1	<i>Planar problem – plane motion</i>	60
5.2.2	<i>Cylindrical problem – rotational motion</i>	66
5.2.2.1	Copper shell I: equal mesh density	68
5.2.2.2	Copper shell II: different mesh density	74
5.2.3	<i>A special problem arising in case of cylindrical sliding surfaces</i>	76
6	Discussion and conclusion	83
6.1	Recapitulation of obtained findings	83
6.2	Suggestions	84
6.3	Conclusion	84
	Appendix A: Source field calculation for complex conductor structures	86
	Bibliography	91
	List of Publications	97
	List of figures	98
	List of tables	102

1 Introduction

Numerical simulations and analysis with the aid of the finite element method have become indispensable in the design process of various electromechanical devices due to the high precision required and the increased level of model complexity. Prominent representatives of such electromechanical devices are electrical machines whose model complexity and non-linear material parameters make analytical models practically useless and demand a dedicated modelling process. In general, the numerical analysis of electrical machines is an expensive task involving the building of a precise finite element model with a high level of detail and leading to time-consuming computations. Nevertheless, this kind of numerical analysis is more essential than ever today with the increasing demand on electrical machines (e.g. various mobile applications as cars, bikes, etc.). Therefore, the usability of numerical simulations with the aid of the finite element method has to be enhanced in order to give effective support to optimization processes of such electrical drives.

The numerical analysis of an electrical machine must include the ability to take account of the motion of the rotor with respect to the stator, a basic phenomenon for the operation of these devices. It is desirable that the finite element mesh of the two parts is fixed, resulting in the overall mesh to become non-matching with hanging nodes along a certain surface called sliding surface. The position of the sliding surface is naturally selected in the air gap of the electrical machine. In classical finite element analysis, hanging nodes are not allowed and the conformity of the finite element mesh has to be guaranteed. In the past decades several different approaches have been introduced to treat this problem. First methods have meshed several models with different rotor positions, or executed local re-meshing in case the mesh would become too distorted due to rotor movement. However, this method exhibits extensive pre-processing as well as enormous computational costs in addition to the drawback of distorted elements and loss of accuracy [37]. To overcome this difficulty of exhaustive pre-processing and enormous computational costs in case of time transient simulations, it is favourable to allow the two meshes of the fixed stator and moving rotor to become non-conforming with hanging nodes along the sliding surface. Once non-conforming meshes are allowed, it becomes possible to build separate finite element meshes and, furthermore, powerful methods for numerical simulations can be introduced. The most popular and successfully implemented methods are the method with Lagrange multipliers as well as the mortaring method, with both techniques imposing the essential interface conditions at the sliding surface in a weak sense [37], [40].

In most common computational tools for calculating electromagnetic fields, a magnetic vector potential is introduced to describe the fields. Unfortunately, in three-dimensional problems, this leads to high computational costs, because it results in a large number of degrees of freedom and because the use of edge elements is mandatory. Therefore, frequently, two-dimensional models are employed to keep computational efforts relatively limited, with the drawback of disabling to cover necessary model details like skewing (although special approximate methods are available to take this into account [102]) or end regions. If a three-dimensional model has to be used, the computational time increases and the numerical modelling becomes overly expensive.

For the reasons addressed above, continuous improvements of existing methods are made and are still ongoing. Owing to the recent development of computational resources and powerful mathematical techniques, numerical simulation methods that have been less in focus in the past years become attractive again. This thesis presents an alternative numerical method, which is simple to implement, able to deal with any kind of relative motion between both domains, and able to couple domains with different discretizations.

1.1 Aim of the work

The present thesis aims to provide a fundamental analysis of the non-conforming mesh method, which is based on the interpolation technique [45] that has been less in focus in the past decades. This non-conforming mesh method is well suited to decrease the computational burden when time transient simulations of three-dimensional problems are carried out. The advantageous use of the magnetic scalar potential in non-conducting regions e.g. the air gap of an electrical machine, and a current vector potential in conducting regions [7] decreases computational costs significantly and enables the use of the interpolation technique. Furthermore, the two independent finite element meshes of the disjoint domains are free to move without loss of the benefits of underlying finite element method.

The objectives of the present thesis are to show up the limits of the non-conforming mesh method and to give a kind of guideline how to use this technique for different user applications. The possible cases to be considered are static coupling of disjoint domains, and coupling when relative movement (planar or rotational) is taken into account. Each of these cases are treated by means of numerical examples and analysed. For analysis purposes, the investigated numerical examples are kept simple and are thus of academic nature. After identifying a problem in case of cylindrical structures in time transient simulations, the coupling strategy has been improved and validated.

Beside this validation of the investigated approach, the non-conforming mesh method has been implemented in the in-house software EleFAnT3D (Electromagnetic Field Analysis Tool 3D) that has been mainly developed by Prof. Oszkár Bíró over the past three decades. The implementation took place in a systematic process. First, a static solver for electric or magnetic problems has been adopted for the use with non-conforming meshes. Hereby, essential knowledge about implementation strategies has been gained. Second, a time transient solver was re-coded to take account of planar or rotational movement as well as to consider motional induction. Incidentally, several adaptations to pre- and post-processing and software packages have been necessary.

1.2 Scientific contributions

The scientific results of this thesis have been presented in various international conferences and have been published in prestigious journals as listed below. These published contributions [P1]-[P10], summarize the main findings and development steps of present thesis.

- The simple method of interpolating slave nodes with corresponding master nodes defined on an interface, where two meshes are allowed to become non-conforming has been investigated for an electrostatic field problem. This first implementation step has been presented in [P1], and marks the beginning of the development of the non-conforming mesh method.
- An error analysis of the non-conforming mesh method has been applied to a cylindrical structure imitating the air gap region of an electrical machine. The numerical solutions have been compared to a known analytical solution for different experiments. It has been shown that the error decreases with the same rate as the classical finite element method if the number of elements is increased. Moreover, the error behaviour has been analysed in case of increasing relative displacement between two domains. These findings have been presented in [P2] and published in [P3].
- A possibility to take account of periodic boundary conditions within the framework of the non-conforming mesh method has been presented for the example of a standard electrical machine with six poles in [P4]. Here, the static magnetic flux density and field intensity have been compared in case of a conforming mesh and in case of a non-conforming mesh.
- The non-conforming mesh method has been applied to time transient problems and has been first presented in [P5]. By means of a simple example, the calculation of motion induced eddy currents with the non-conforming mesh method have been demonstrated.
- As a continuation of [P5], the non-conforming mesh method has been applied to a voltage driven induction machine. The early results of this investigation have been presented in [P6] and [P7]. It could be shown that the obtained stator currents compare very well with the results obtained by a reference software.
- Regarding to cylindrical structures, a special problem arises owing to the refinement of the discretization of the domains along the sliding surface. The issue of geometrical errors have been treated and presented in [P8] and published in [P10]. According to these findings, the coupling strategy has been improved for the case where cylindrical structures need to be taken into account.

1.3 Structure of the work

The present thesis contains six chapters comprising all necessary development steps as well as basic details that underlay the investigated non-conforming mesh method. This chapter 1 introduces and motivates the present work. The aim of the work has been outlined as well as the scientific contributions have been pointed out.

In chapter 2 relevant literature is reviewed that deals with coupling of two independent finite element meshes of two disjoint domains. The review concentrates on methods based on the finite element method. These methods are classified into two groups: classical methods and modern methods.

The theoretical background including fundamental laws and, following from this, relevant potential formulations are given in chapter 3. The basic concept of the finite element method, subdivided into the discussion of Galerkin's approach, as well as space and time discretizations, is given as well.

Chapter 4 introduces the non-conforming mesh method. Here, the coupling of the potentials as well as the reformulated equation system in case of a magneto-static problem is presented. Thereafter, an error analysis is carried out based on the example of a cylindrical structure imitating the air gap of an electrical machine.

The extension to quasi-static eddy current problems is given in chapter 5. After introducing an approach to take account of motional induced eddy currents, the quasi-static eddy current formulation is adopted for the non-conforming mesh method. The validation of the introduced method is carried out for different examples. Time transient simulations regarding to planar movement and rotational movement are investigated. In each case, the transient behaviour of the induced eddy currents are analysed and compared to reference methods. The problem of geometrical errors due to cylindrical structures in rotational movement is also treated.

Chapter 6 concludes the present work, discussing the investigated method. Finally, an outlook and suggestions for further studies are given.

2 Review of relevant research work

In this chapter, a brief survey of relevant methods that take account of relative motion between a stationary and a moving domain is given. The review concentrates on methods based on the finite element method (FEM) as they are more convenient for such problems. The methods are classified into a class of techniques that preserve the conformity of the overall finite element mesh under movement and, additionally, into a class of methods where two independent meshes (both of them are fixed to their frame of reference) are allowed to become non-conforming along a so-called sliding surface (slip surface). The moving domain is then free to move at any defined position without distorting the initial mesh topology.

Most of the methods have been developed with similar problems to face, e.g. computational power. Therefore, continuous improvements in terms of applicability, numerical robustness and computational costs are investigated and still ongoing. This fact is highlighted by the vast amount of literature that can be found. Thus, a small selection of remarkable literature only is cited in this section.

For the sake of completeness it is noted that another possibility besides the methods listed below is constituted by the boundary element method (BEM) [103]. As the pure BEM which is based on integral techniques is not the first choice for electromagnetic problems especially if non-linear material properties are considered, the coupling of FEM-BEM has been investigated [105], [106]. Here, the non-solid domains, e.g. air, are modelled with BEM whereas the solid domains are modelled with FEM. Recent advances demonstrate the possible use of this FEM-BEM coupling to treat electrical machine problems [104]. However, compared to pure finite element approaches, the coupling with FEM-BEM is more complex and the resulting system matrix demands special treatment for solving. Beside that, the issue of non-simply connected domains still requires some further development [104]. Thus, the applicability to electromagnetic problems e.g. electrical machines is still limited.

2.1 Traditional methods

Re-meshing/ Adaptive meshing:

At the beginning of the analysis of rotating electrical machinery, different finite element models of the electrical machine were needed to take account of different rotor positions. This kind of analysis demands much effort on pre-processing, and has the drawback to be restricted to steady state analysis only [59], [60]. To reduce the tremendous pre-processing, software packages were developed in which the stator and rotor are separated for mesh generation and reassembled for a certain rotor position [61]. Nevertheless, the analysis of the dynamical behaviour of electrical machines challenges the modelling of continuous rotor movement. First ideas to deal with this problem are presented in e.g. [62], [63]. In these works, a step-by-step movement of the rotor is executed, where the air gap is remeshed only. While moving the rotor, the mesh becomes distorted and loses its integrity. Therefore, the Delaunay criterion [64], [65] for adaptive remeshing is used to preserve the integrity of the air gap mesh and guarantees the conformity of the overall mesh. The use of this method decreases the computational burden significantly, since the mesh of the stator and rotor are kept fixed in their own reference frame over the considered period. However, the obtained system matrices need to be recalculated after each time step.

Moving band technique:

The moving band technique introduced by [66] follows the idea given in [62] with the difference that the air gap domain is subdivided into a single layer of a regular finite element mesh. As the stator and rotor mesh is fixed in their own frame, the numbering of the nodes can be kept constant along the so-called moving band in the air gap. This yields the advantage that the specific part of the system matrix which corresponds to the moving band need to be recalculated at each time step only. While moving the rotor, the mesh of the moving band becomes distorted and will be remeshed if the distortion of the mesh becomes too large [67], [68].

2.2 Modern methods

Air-Gap element – Fourier method:

In contrast to the previously described methods, the air-gap element approach avoids extensive pre-processing and costly remeshing of the air gap domain. This air-gap element approach or so-called Fourier method was first introduced and pioneered by [70], [71]. Here, the uniform part of the air gap is modelled by a single air-gap element (macro element) providing a constant topology during rotor movement. In this special air-gap element, the exact solution of the governing differential equation can be written as a Fourier series. The Fourier coefficients are related to the nodes and boundary conditions along the stator and rotor side of the air-gap element. Hence, the air-gap element increases the system matrix bandwidth significantly, which results in higher computational effort.

Overlapping element method:

The overlapping element method originates in the work of [75] for two-dimensional problems, is capable to couple two disjoint domains having independent meshes regardless to element size. Independent of the method proposed in [75], a similar approach was introduced by [76] to take account of the rotor movement for analysing electrical machines. In recent years, the overlapping element method was extended to three-dimensional problems and for different types of elements: hexahedral meshes [77], [80], tetrahedral elements and prisms [78], [79]. The overlapping element method allows two disjoint meshes of a stationary and moving domain to overlap along the surface where these domains intersect. Here, the nodes associated to the surface of the stationary domain are projected to the intersecting surface of the moving domain and vice versa. Therefore, virtual elements are created along the sliding surface without introducing additional degrees of freedom. The virtual nodes are solely used to define continuous shape functions to approximate the nodal degrees of freedom in the overlapping area. Hence, the sparsity and symmetry of the system matrix is preserved by the overlapping element method.

Interpolation method and locked step approach:

Similar to the overlapping element method, the interpolation method is capable of coupling two independent finite element meshes of two disjoint domains along a so-called sliding surface regardless of the element type used (nodal or edge based). The interpolation method was developed by [45] for three dimensional problems and successfully applied to real world problems, e.g. [39], [46], [47], [81], [82]. By this interpolation method, the degrees of freedom associated to nodes or edges become interpolated in a master/slave principle. According to this master/slave principle, master and slave nodes/edges have to be defined along the sliding surface where the meshes of the two disjoint domains become non-conforming. In this method, the properties of the classical finite element method are preserved as no additional constraints

or degrees of freedom are introduced. In the work of [47], the interpolation method is extended to higher order interpolation to improve the precision of the interpolation.

A method constituting a special case of the interpolation method is the locked step approach [69]. If the time step is chosen in a way that the rotor displacement is equal or at least a multiple to the element length of the regular mesh in the air gap, the special case of the locked step is arrived at. By doing so, the mesh in the air gap becomes conformal at each time step, providing highest accuracy and all advantages of the classic finite element method. However, as only discrete rotor shifts are allowed, a sufficient number of elements in the air gap have to be chosen.

Lagrange multiplier method:

The Lagrange multiplier method was first introduced by [37] for two-dimensional problems and afterwards extended to three-dimensional problems in the work of [38] and similarly in [83]. The Lagrange multiplier method is a very general approach and, indeed, widely used in many finite element codes and applications, e.g. [84] - [87]. To couple two independent meshes along a suitable surface (sliding surface), the Lagrange multiplier method introduces additional constraints to guarantee physical continuity between the domains with independent meshes. The additional constraints are incorporated into the original functional of the problems to be analysed. These additional equations lead to an ill-conditioned and non-positive definite system matrix. Hence, solving this equation system is problematic [39]. The set of Lagrange multipliers can be obtained by two approaches. First, the Lagrange multipliers can be interpolated on the sliding surface with the aid of the appropriate basis functions (nodal or edge). Second, eliminating the Lagrange multipliers from the functional, leads to a positive definite system matrix [39].

Mortaring methods:

The mortar element method is another class of techniques that is able to couple two independent meshes regardless to their element size or type. A definition of the mortar element method for three-dimensional problems is extensively described in [40], and in a more compact form in [46]. The mortar element method is, again, widely used in finite element codes and is applicable to many electromechanical problems due to its generalised formulation [88]. Similar to the Lagrange method, the essential interface conditions are imposed weakly with the aid of the variational method at the sliding surface. Hereby, the potentials of one domain, e.g. moving domain, are expressed by those potentials of the stationary domain. However, the Lagrange multipliers are eliminated from the additional equations, which adds a dense matrix block to the overall equation system. Indeed, the system matrix is still symmetric and positive definite. Beside this classic mortaring method, a very similar method is known as Nitsche-type mortaring method [41] - [43]. Here, the interface conditions are imposed weakly without introducing additional unknowns, e.g. Lagrange multipliers. The two disjoint domains are treated individually and the symmetry of the resulting equation system is retained by adding a symmetrisation term [89]. Thus, the characteristics of the classic finite element method are preserved

Discontinuous Galerkin approach:

The Discontinuous Galerkin approach originally developed for mechanical problems [90] - [92] and for elliptical problems in [93], provides an alternative approach to couple non-conforming meshes in case of electromagnetic field problems. The applicability is shown by the work of [94], [95] as well as in the recently published works [96], [97]. In this approach, the boundary constraints between the two disjoint domains are enforced in a weak sense by numerical fluxes, which are fixed functions of the unknowns. Therefore, no additional unknowns are introduced. However, as the numerical fluxes are defined point-wise on each element edge, the number of degrees of freedom is increased. Since this method is a pure finite element method, the sparsity of the system matrix is preserved.

2.3 Conclusion

The previously listed methods are more or less applicable to the analysis of the dynamical behaviour of electrical machines. As the computational power was a limiting factor in earlier days, some of the developed methods seemed to be not feasible enough. Independently, from a numerical viewpoint, advantages and drawbacks are obtained as well. Apparently, the re-meshing of the air-gap domain [62] as well as the moving band method [66] introduce a numerical noise in the solution, which is known as torque ripple [75]. These methods also require a powerful mesh generator and still high demand on computational power, especially in case of three-dimensional problems. To overcome these difficulties, two independent meshes are allowed to move freely, relative to each other. The overlapping method [75], interpolation method [45] and the locked step approach [69] are simple methods and easy to implement. Nevertheless, the locked step approach is not feasible for time transient simulations as unacceptable restrictions on the choice of time step length are introduced [98]. However, the computational effort becomes greater in case edge element representation is necessary, e.g. for magnetic vector potential formulations. Here, the interpolation factors are obtained by integration along the element edges.

A powerful alternative to these methods is given by the air-gap element method. Although, special attention must be paid to solving the equation system obtained in order to be as competitive as other methods [72], the air-gap method provides a sound basis for different machine analyses, e.g. magnetic bearings [73] and skewing [74].

The most flexible methods in terms of element type and mesh topology that appear are the Lagrange multipliers [37] and mortaring methods [40]. As the Lagrange multipliers method loses the advantages of the underlying finite element method, improvements are made to retain a symmetric and positive definite system matrix, e.g. [99] - [101]. However, both methods are computational costly and become even less attractive if three-dimensional problems are considered.

The discontinuous Galerkin approach [90] is, again, a computationally costly method as numerical fluxes are introduced and therefore the number of degrees of freedom is increased. To overcome this, it is suggested to split the overall problem domain into parts using classical finite element method and domains using the local discontinuous Galerkin approach. Thus, the number of unknowns will be decreased and the method becomes computational competitive to other methods [94].

At this point, it should be noted that above methods have been widely investigated for scalar potential formulations or magnetic vector potential formulations using triangular or tetrahedral elements in two-dimensional or three-dimensional problems, respectively.

3 Fundamentals

The use of optical and electromagnetic devices such as mobile phones or the internet has become vital in the daily life of people and is going to increase further. All of these everyday gadgets underlie certain electromagnetic phenomena, which can be described by the fundamental equations formulated by James Clerk Maxwell in 1873. These Maxwell's equations also form the basis for other types of electromagnetic problems arising, among others, in electrical machines. Utilizing scalar and vector potentials to describe the field quantities, they result in second order partial differential equations. As these partial differential equations are hard to solve analytically, numerical methods like the finite element method [1], [2] can be used to solve them.

After writing Maxwell's equations in their basic form, the magneto-static problem as well as the quasi-static eddy current problem will be defined. In addition to that, the case of motion induced eddy currents will be treated. Thereinafter, the finite element method is introduced by discussing the method of weighted residuals and space discretization using finite elements. Finally, a time discretization method is presented. Moreover, the potential formulation of the magneto-static problem with the aid of the reduced scalar potential as well as two potential formulations for eddy current problems [5], [7] are discussed.

3.1 Electromagnetic field

3.1.1 Maxwell's equations

Maxwell's equations are capable of describing different electromagnetically coupled phenomena with the aid of the field quantities. These equations are an accumulation of Ampère's law, Faraday's law of induction and Gauss' laws [23], [24]. With these Maxwell's equations, problems ranging from antennas (wave propagation) to electrical machines (quasi-static problems) can be described [25]. In this thesis, the focus will be kept on static and quasi-static problems, in which the Maxwell's equations become simplified. It is assumed here, that the time variation of the field quantities takes place at low frequency. Therefore, the displacement current density, caused by the time derivative of the electric flux density $\partial \mathbf{D} / \partial t$, can be neglected. In Tab. 1, the differential and integral formulations of Maxwell's equations are summarized.

The integral form of Maxwell's equations is obtained by using Gauss' theorem and Stokes' theorem [24]. Gauss' theorem states the equivalence of a volume integral of the divergence of a vector field to a surface integral over the surface bounding the volume. This can be physically interpreted as the accumulation of sources within a defined volume being equal to the flux of these sources flowing through the bounding surface. Stokes' theorem states the conversion of a surface integral of the curl of a vector field to a closed line integral over the curve bounding the surface. In other words, the circulation of a vector field around a closed path is equal to the flux of the curl of the vector field through the surface enclosed by this closed path.

	differential formulation	integral formulation
Ampère's law	$\text{curl} \mathbf{H} = \mathbf{J}$	(1) $\oint_{C=\partial\Gamma} \mathbf{H} \cdot d\mathbf{s} = \int_{\Gamma} \mathbf{J} \cdot d\Gamma$
Faraday's law	$\text{curl} \mathbf{E} = -\frac{\partial \mathbf{B}}{\partial t}$	(2) $\oint_{C=\partial\Gamma} \mathbf{E} \cdot d\mathbf{s} = -\int_{\Gamma} \frac{\partial \mathbf{B}}{\partial t} \cdot d\Gamma$
Gauss' law for magnetism	$\text{div} \mathbf{B} = 0$	(3) $\oint_{C=\partial\Gamma} \mathbf{B} \cdot d\Gamma = 0$
Gauss' law	$\text{div} \mathbf{D} = \rho$	(4) $\oint_{\Gamma=\partial\Omega} \mathbf{D} \cdot d\Gamma = \int_{\Omega} \rho d\Omega$

Tab. 1: Electromagnetic field equations, the so-called Maxwell's equations in two ways of formulations, differential and integral. The boundary of the surface Γ is denoted by $\partial\Gamma$, $\partial\Omega$ denotes the bounding surface of the volume Ω and \mathbf{n} denotes the surface normal vector pointing outward of closed surfaces.

In addition to Maxwell's equations, a fifth fundamental equation can be obtained from Ampère's law (1). The law of continuity states the principle of charge conservation and is written as

$$\text{div}(\text{curl} \mathbf{H}) \equiv 0 = \text{div} \mathbf{J}. \quad (5)$$

The quantities in (1)-(4) are defined as follows: the magnetic field intensity vector \mathbf{H} , the current density vector \mathbf{J} , the electric flux density vector \mathbf{D} , the electric field intensity vector \mathbf{E} , the magnetic flux density vector \mathbf{B} and the electric volume charge density ρ . Taking account of the material properties, these field quantities are coupled as

$$\mathbf{B} = \mu\mathbf{H} = \mu_0\mu_r\mathbf{H}, \quad (6)$$

$$\mathbf{D} = \varepsilon\mathbf{E} = \varepsilon_0\varepsilon_r\mathbf{E}, \quad (7)$$

$$\mathbf{J} = \sigma\mathbf{E}, \quad (8)$$

with the relative permeability μ_r and the permeability of vacuum $\mu_0 = 4\pi \cdot 10^{-7} \text{Vs}(Am)^{-1}$, the relative permittivity ε_r and the permittivity of vacuum $\varepsilon_0 \cong 8.8541 \cdot 10^{-12} \text{As}(Vm)^{-1}$ as well as the conductivity σ . Unless isotropic materials are considered, these material properties become tensors. Typically, these material properties vary with temperature, frequency, field intensity and location inside the medium.

3.1.2 Faraday's law of induction

The effect of the electromagnetic field and the forces acting on charged particles or moving charged particles are demonstrated by the characteristic experiments of Faraday. These experiments substantially say that, whenever a conductor is moved in the presence of a static magnetic field, a current will flow (Lorentz' force law). Conversely, if a conductor is stationary but exposed to a time varying magnetic field, a current will again flow in this conductor (Faraday's law). These phenomena can be summarized in the Eulerian reference frame as

$$\mathbf{F} = q(\mathbf{E} + \mathbf{v} \times \mathbf{B}) \quad (9)$$

with \mathbf{F} denoting the force acting on a charged particle q and \mathbf{v} denoting the velocity of the particle. Because of this force acting on the conductor, an electric field will arise within this conductor due to the separation of the charged particles (see Fig. 1a). In steady-state the force become zero $\mathbf{F}=0$, and, hence, this electric force is then equal to the magnetic force

$$\mathbf{F} = q(\mathbf{E} + \mathbf{v} \times \mathbf{B}) = 0 \rightarrow \mathbf{E} = -(\mathbf{v} \times \mathbf{B}). \quad (10)$$

The work to separate the charged particles is named as electro-motive force (*emf*) and is defined as

$$U_{emf} = \frac{1}{q} \oint_C \mathbf{F} \cdot d\mathbf{s} = \oint_C (\mathbf{v} \times \mathbf{B}) \cdot d\mathbf{s}, \quad (11)$$

where C denotes a closed line within the conductor. If the conductor is exposed to a magnetic field that is homogeneous over the whole domain including this conductor, the electro-motive force will be zero. In contrast to that, the electro-motive force is unequal to zero, if the magnetic field is inhomogeneous within the domain comprising the conductor. An illustration of both cases is given in Fig. 1.

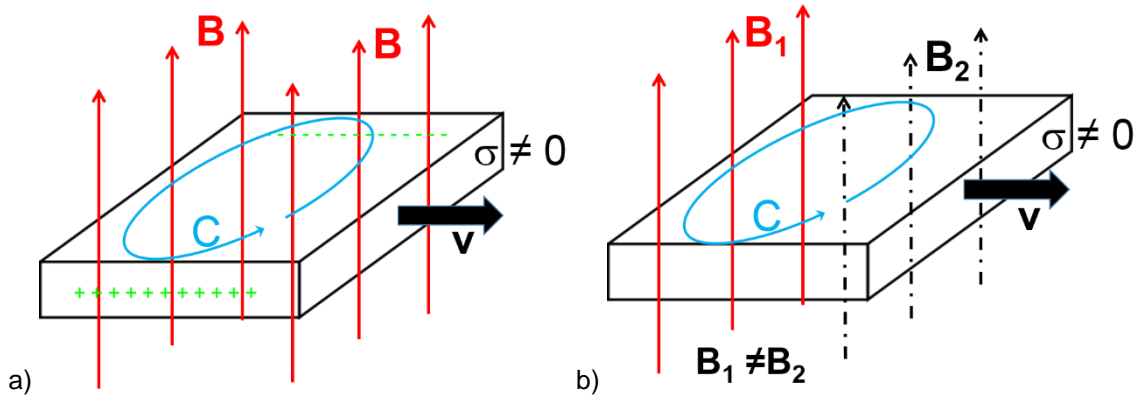


Fig. 1: Illustration of a conducting domain ($\sigma \neq 0$) moving with velocity \mathbf{v} in a homogeneous (a) and inhomogeneous (b) magnetic field.

The electro-motive force in (11) can also be interpreted as the time variation of the magnetic flux Φ through an arbitrary surface Γ within the conducting domain.

$$U_{emf} = -\frac{d\Phi}{dt} = -\frac{d}{dt} \int_{\Gamma} \mathbf{B} \cdot \mathbf{n} d\Gamma. \quad (12)$$

Taking the time variation of the magnetic flux density \mathbf{B} into account, the *emf* can be rewritten as

$$\frac{d\Phi}{dt} = \int_{\Gamma} \frac{\partial \mathbf{B}}{\partial t} \cdot \mathbf{n} d\Gamma - \oint_{C=\partial\Gamma} (\mathbf{v} \times \mathbf{B}) \cdot d\mathbf{s}. \quad (13)$$

Substituting (10) into (11) and comparing it to (13), Faraday's law is arrived which is independent of the presence of a conducting medium:

$$\oint_{C \in \partial\Gamma} \mathbf{E} \cdot d\mathbf{s} = -\int_{\Gamma} \frac{\partial \mathbf{B}}{\partial t} \cdot \mathbf{n} d\Gamma. \quad (14)$$

As mentioned before, a variation of the magnetic field gives rise to an electric field. In the presence of a conductive medium, this electric field causes circular currents to flow in the conducting domain. These circular currents are named as eddy currents. As a result of these eddy currents, a magnetic field is generated affecting the original magnetic field. This damping influence mainly depends on the frequency of the change of the exciting magnetic field and the conductivity of the conducting domain. An illustration of eddy currents in the case of a homogeneous conducting domain is given in Fig. 2.

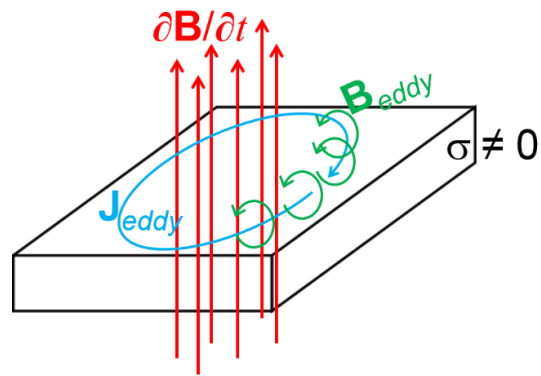


Fig. 2: If a conducting domain ($\sigma \neq 0$) is exposed to a time varying magnetic field, eddy currents \mathbf{J}_{eddy} will flow in the conducting material causing a magnetic field \mathbf{B}_{eddy} . This field is then counteracting to the change of the exciting magnetic field.

3.2 Problem definitions

3.2.1 Magneto-static problem:

When describing the magneto-static problem, Ampère's law (1) and the Gauss' law for magnetism (3) need to be considered. To define a magneto-static problem, consider a problem domain Ω with the boundaries $\Gamma_H = \sum_{i=1}^N \Gamma_{H,i}$ and Γ_B as shown in Fig. 3. The excitation of the magnetic field is given by a source coil with impressed current density \mathbf{J}_0 , which is placed in a region without magnetic material.

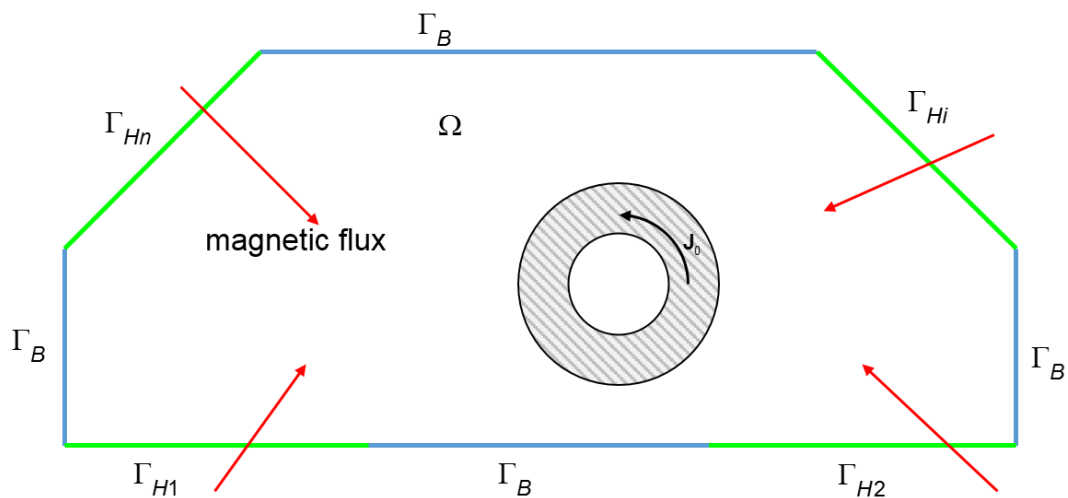


Fig. 3: Generalized topology of a magneto-static problem.

To ensure the solvability of the magneto-static problem, a set of differential equations as well as boundary conditions on the boundaries Γ_H and Γ_B need to be defined. Hence, such problems are also called boundary value problems. The tangential component of the magnetic field intensity \mathbf{H} is prescribed on the boundary Γ_H . This is equivalent to assuming an impressed vector field \mathbf{K} as a surface current density on the surface Γ_H , forming the boundary to an external magnetic wall ($\mu_r \gg 1$). Setting the tangential component of \mathbf{H} to zero ($\mathbf{K}=0$), could represent a symmetry plane of the problem. By defining the normal component of the magnetic flux density \mathbf{B} as a fictitious surface charge density b , the flux through Γ_B is prescribed. By setting the normal component of \mathbf{B} to zero ($b=0$), a possible symmetry plane can again be taken into account. The magneto-static boundary value problem is summarized in Tab. 2, with the outward surface normal vector denoted by \mathbf{n} .

	Domain	Definition/Condition
Maxwell's Equations:	Ω	$\text{curl} \mathbf{H} = \mathbf{J}$
	Ω	$\text{div} \mathbf{B} = 0$
Boundary condition:	$\Gamma_H = \sum_{i=1}^n \Gamma_{H,i}$	$\mathbf{H} \times \mathbf{n} = \mathbf{K}$
	Γ_B	$\mathbf{B} \cdot \mathbf{n} = -b$

Tab. 2: Summary of the equations and boundary conditions for the magneto-static boundary value problem.

3.2.2 Quasi-static eddy current problem:

In case of quasi-static eddy current problems, the set of Maxwell's equations (1) - (3) need to be considered. This kind of boundary value problem can be defined by a generalized topology comprising a conducting domain Ω_c and a non-conducting domain Ω_n as shown in Fig. 4. In case of the non-conducting domain, the same differential equations and boundary conditions as in the magneto-static case are valid. However, in this case, the field quantities are time-dependent. For the conducting domain, the presence of the eddy currents with the current density \mathbf{J} has to be additionally considered with the aid of Faraday's law. Again, to ensure a unique solution of the differential equations, boundary conditions need to be defined [5], [17]. The outer boundaries of the conducting domain are divided into electrical and magnetic boundaries: Γ_{Ec} and Γ_{Hc} , whereas the outer boundary of the non-conducting domain is constituted by Γ_{Hn} and Γ_{Bn} . In addition to these boundary conditions, an interface condition on Γ_{cn} between the conducting and non-conducting domain need to be defined. The excitation of the magnetic field is a given current density \mathbf{J}_0 within the non-conducting domain.

The quasi-static boundary value problem is defined and summarized in Tab. 3. The tangential component of the magnetic field intensity \mathbf{H} is specified on the boundaries Γ_{Hc} and Γ_{Hn} , whereas the tangential component of the electric field intensity \mathbf{E} is defined on Γ_{Ec} . The normal component of the magnetic flux density \mathbf{B} is defined on Γ_{Bn} . The continuity of the tangential component of the magnetic field intensity and the normal component of the magnetic flux density along the interface Γ_{cn} between the domains Ω_n and Ω_c , ensure the coupling of the formulations used in the conducting and non-conducting domains.

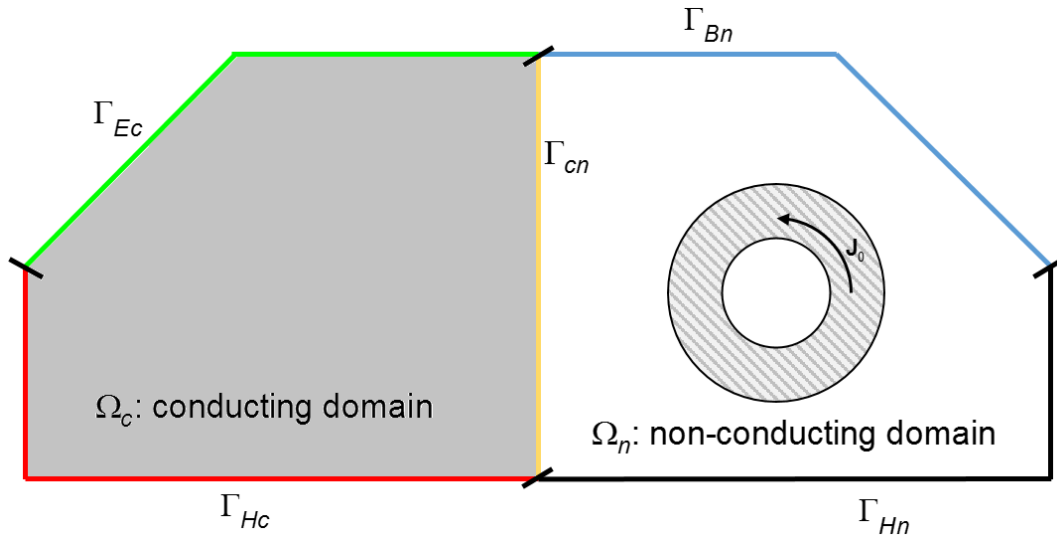


Fig. 4: Generalized topology for a quasi-static eddy current problem.

	Domain	Definition/Condition
Equation:	Ω_n	$\text{curl} \mathbf{H} = \mathbf{J}_0$
	Ω_n	$\text{div} \mathbf{B} = 0$
	Ω_c	$\text{curl} \mathbf{H} = \mathbf{J}$
	Ω_c	$\text{curl} \mathbf{E} = -\frac{\partial \mathbf{B}}{\partial t}$
	Ω_c	$\text{div} \mathbf{B} = 0$
Boundary condition:	Γ_{Hn}	$\mathbf{H} \times \mathbf{n} = \mathbf{K}$
	Γ_{Bn}	$\mathbf{B} \cdot \mathbf{n} = -b$
	Γ_{Hc}	$\mathbf{H} \times \mathbf{n} = 0$
	Γ_{Ec}	$\mathbf{E} \times \mathbf{n} = 0$
	Γ_{cn}	$\mathbf{H} \times \mathbf{n}$ and $\mathbf{B} \cdot \mathbf{n}$ continuous

Tab. 3: Summary of the equations and boundary conditions for the quasi-static, boundary value problem.

3.3 Method of weighted residuals

The method of weighted residuals or the method of Galerkin constitutes the basis of the finite element method [3], [4], [8], [16]. This method is illustrated by the example of a second order, time independent differential equation of Poisson type in a domain Ω :

$$-\Delta u = f, \text{ at } \Omega \quad (15)$$

where u is the unknown function and f denotes the given exciting function. The uniqueness of the solution is ensured through the definition of the Dirichlet boundary condition $u = u_D$ on Γ_D describing the function values and the Neumann boundary conditions $\partial u / \partial n = \gamma_N$ on Γ_N describing the surface normal derivatives of the unknown function u .

Following the approach of Ritz, the unknown function u can be approximated by a linear combination of linear independent functions $\varphi_0, \varphi_1 \dots \varphi_m$:

$$u \approx \tilde{u} = \varphi_0 + \sum_{k=1}^m v_k \varphi_k \quad (16)$$

where φ_0 satisfies the Dirichlet boundary conditions exactly. With this approach, the differential equation (15) and the Neumann boundary conditions can be satisfied approximately by appropriately selecting the coefficients v_k . If (16) is substituted into (15), the resulting differential equation is not satisfied exactly, an error R arises. This residual is defined as

$$\Delta \varphi_0 + \sum_{k=1}^m v_k \Delta \varphi_k - f = R. \quad (17)$$

It is demanded that this error R will vanish on average over the domain Ω if multiplied by some pre-defined weighting functions. If these weighting functions are chosen to be equal to the basis functions $\varphi_1 \dots \varphi_m$, the resulting residual function R is orthogonal to the function space spanned by the basis functions $\varphi_1 \dots \varphi_m$. This leads to a set of m equations to evaluate the unknown constant coefficients v_k . Therefore, the residual function is defined to satisfy

$$\int_{\Omega} R \varphi_j d\Omega = 0, \text{ with } j = 1, 2, \dots, m. \quad (18)$$

Substituting (17) into (18) and utilizing Green's identity [3],[25], a set of algebraic equations is obtained as

$$\sum_{k=1}^m v_k \left[\underbrace{\int_{\Omega} \text{grad } \varphi_k \cdot \text{grad } \varphi_j d\Omega + \oint_{\Gamma=\partial\Omega} \frac{\partial \varphi_k}{\partial n} \varphi_j d\Gamma}_{=\int_{\Omega} \Delta \varphi_k \cdot \varphi_j d\Omega, \text{ Green's identity}} \right] + \int_{\Omega} \text{grad } \varphi_0 \cdot \text{grad } \varphi_j d\Omega + \oint_{\Gamma=\partial\Omega} \frac{\partial \varphi_0}{\partial n} \varphi_j d\Gamma - \int_{\Omega} f \varphi_j d\Omega = 0, \text{ with } j = 1, 2, \dots, m. \quad (19)$$

By taking advantage of the boundary conditions on $\Gamma = \Gamma_D + \Gamma_N$, the equation system (19) can be rewritten as

$$\sum_{k=1}^m v_k \int_{\Omega} \text{grad } \varphi_k \cdot \text{grad } \varphi_j d\Omega = - \int_{\Omega} \text{grad } u_D \cdot \text{grad } \varphi_j d\Omega + \int_{\Gamma_N} \gamma_N \varphi_j d\Gamma + \int_{\Omega} f \varphi_j d\Omega, \text{ with } j = 1, 2, \dots, m \quad (20)$$

with $\varphi_0 = u_D$ and $\varphi_k = 0$, $k=1, \dots, m$ on Γ_D . Apparently, the Neumann boundary conditions are satisfied implicitly and, therefore, they are called natural boundary conditions.

In case of time dependent differential equations, the Galerkin method can be used by assuming the unknown coefficients to be time dependent $v_k(t)$. In general, the solution is dependent on time and the spatial coordinates \mathbf{r} . As an example, consider the time dependent differential equation in domain Ω as

$$-\Delta u - f(\mathbf{r}, t) + C \frac{\partial u}{\partial t} = 0, \text{ in } \Omega \quad (21)$$

with a constant coefficient C , the Dirichlet boundary $u(\mathbf{r}, t) = u_D(\mathbf{r}, t)$ on Γ_D and the Neumann boundary $\partial u(\mathbf{r}, t) / \partial n = \gamma_N(\mathbf{r}, t)$ on Γ_N for $t > 0$. The initial value at time $t=0$ is given as $u(\mathbf{r}, 0) = u_0(\mathbf{r}, 0)$ in Ω . Hence, the approximation of the unknown function $u(\mathbf{r}, t)$ is defined as

$$u(\mathbf{r}, t) \approx \tilde{u}(\mathbf{r}, t) = \varphi_0(\mathbf{r}, t) + \sum_{k=1}^m v_k(t) \varphi_k(\mathbf{r}) \quad (22)$$

where $\varphi_0(\mathbf{r}, t)$ satisfies exactly the inhomogeneous boundary conditions on Γ_D , whereas $\varphi_k(\mathbf{r})$ satisfy the time independent homogeneous boundary conditions on Γ_D . Applying Galerkin's method to the differential equation (21) as previously shown and taking account of the boundary conditions, the resulting set of algebraic equations is obtained as

$$\begin{aligned} \sum_{k=1}^m \left(v_k(t) \int_{\Omega} \text{grad } \varphi_k \cdot \text{grad } \varphi_j d\Omega + \frac{\partial v_k}{\partial t} \int_{\Omega} C \varphi_k \varphi_j d\Omega \right) = - \int_{\Omega} \text{grad } u_D \cdot \text{grad } \varphi_j d\Omega + \\ + \int_{\Gamma_N} \gamma_N \varphi_j d\Gamma + \int_{\Omega} \left(f - C \frac{\partial u_D}{\partial t} \right) \varphi_j d\Omega, \text{ with } j = 1, 2, \dots, m. \end{aligned} \quad (23)$$

The equation systems in (20) and (23) can be rewritten in a compact matrix form. As an example, the matrix form of (23) is presented. This can be written with the stiffness matrix $[\mathbf{A}]$ and mass matrix $[\mathbf{M}]$ as

$$[\mathbf{A}]\{\mathbf{v}\} + [\mathbf{M}]\{\dot{\mathbf{v}}\} = \{\mathbf{b}\} \quad (24)$$

with $\dot{\mathbf{v}}$ denoting the first-order time derivatives and the matrix elements:

$$a_{kj} = \int_{\Omega} \text{grad } \varphi_k \cdot \text{grad } \varphi_j d\Omega, \quad m_{kj} = \int_{\Omega} C \varphi_k \varphi_j d\Omega, \quad (25)$$

$$b_j = - \int_{\Omega} \text{grad } u_D \cdot \text{grad } \varphi_j d\Omega + \int_{\Gamma_N} \gamma_N \varphi_j d\Gamma + \int_{\Omega} \left(f - C \frac{\partial u_D}{\partial t} \right) \varphi_j d\Omega. \quad (26)$$

Note that, if the terms in (24)-(26) including the time derivative are omitted, the matrix form of (20) is arrived at.

As presented, the method of weighted residuals (Galerkin's method) is a suitable numerical technique for solving partial differential equations. Since the basis functions are defined over the whole domain Ω , it is difficult to choose them to satisfy the homogeneous Dirichlet boundary conditions in case of practical geometries. Therefore, a discretization of the domain Ω into subdomains is appropriate, in which case the satisfaction of the boundary conditions is easier to achieve. Furthermore, in case of time dependent problems, a time discretization is needed as well.

3.4 Space discretization using finite elements

For discretizing a continuous domain, several techniques are known, e.g. the methods of finite differences, finite volumes and finite elements. The latter technique is used here for electromagnetic problems [7], [17] - [20], [22]. The domain discretization with finite elements leads to a so-called finite element mesh or grid. Thereby, a continuous domain is subdivided, depending on the dimensionality of the problem most commonly either into line segments (1D), triangles or quadrilaterals (2D), or tetrahedra, triangular prisms or hexahedra (3D). Depending on the polynomial order of the basis functions within them, these different types of elements can be designed to be linear, second order or of higher order. Fig. 5 illustrates such linear finite elements. In the following, the focus is kept on second order hexahedral elements, as the investigation made in this thesis deals with three-dimensional (3D) problems and the use of second order hexahedral elements. These higher order elements have the advantage to be capable of reconstructing shapes that are curved and diminish geometrical errors e.g. in cylindrical structures

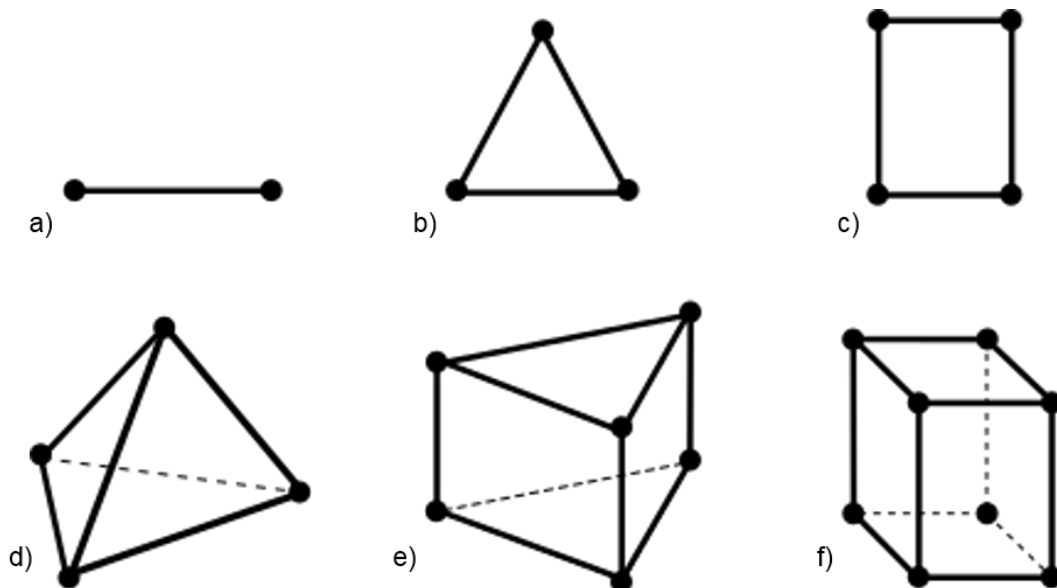


Fig. 5: Different types of linear elements, regarding to the dimensionality of the considered problem. a) 1D line element b) 2D triangle element c) 2D quadrilateral element d) 3D tetrahedral element e) 3D triangular prism f) 3D hexahedral element.

The elements shown can be further classified into node based and edge based elements. Fig. 6a shows a node based, second order element with 20 nodes, whereas the hybrid version of an edge and node based element with 36 edges and 20 nodes is shown in Fig. 6b. By using node based second order elements, the degrees of freedom are expressed by the values of the approximated quantity in the nodes of the elements imposing full continuity. In case of vectorial quantities, both the normal and tangential components are continuous. The solution becomes approximated with the aid of the node based shape functions $N_j(\xi, \eta, \zeta)$. These functions are defined in the local coordinate space $\{\xi, \eta, \zeta\} \in [-1, 1]$ of the finite element. The shape functions $N_j(\xi, \eta, \zeta)$ are defined as second order polynomial functions for all $n=20$

nodes. Thus, these basis functions are a linear combination of 20 polynomials for node j , which can be written as an inner product:

$$N_j(\xi, \eta, \zeta) = \mathbf{C}_j^T \cdot \mathbf{K}, \quad \text{with } \mathbf{K} = \begin{bmatrix} 1 \\ \xi \\ \eta \\ \zeta \\ \xi\eta \\ \xi\zeta \\ \vdots \\ \xi\eta\zeta^2 \end{bmatrix} \quad \text{and } \mathbf{C}_j = \begin{bmatrix} c_{j,1} \\ c_{j,2} \\ c_{j,3} \\ \vdots \\ c_{j,20} \end{bmatrix} \quad (27)$$

with the vector \mathbf{K} comprising appropriate permutations of $\{\xi^p, \eta^r, \zeta^s\}$, and the coefficient vector \mathbf{C}_j comprising the coefficients of these power functions. These coefficients are derived from the shape functions' property of being equal to one at node j and zero at all other nodes:

$$N_j(\xi, \eta, \zeta) = \begin{cases} 1 & \text{at node } j \\ 0 & \text{at all other nodes} \end{cases} \quad (28)$$

Explicitly, the coefficient vector \mathbf{C}_j can be written with the aid of the $(n \times n)$ identity matrix \mathbf{E} as

$$\mathbf{W} = \mathbf{L}^{-1} \cdot \mathbf{E} = \mathbf{L}^{-1}, \quad \text{with } \mathbf{L} = \begin{bmatrix} \mathbf{K}^T(\xi_1, \eta_1, \zeta_1) \\ \vdots \\ \mathbf{K}^T(\xi_j, \eta_j, \zeta_j) \\ \vdots \\ \mathbf{K}^T(\xi_{20}, \eta_{20}, \zeta_{20}) \end{bmatrix} \quad \text{and } \mathbf{W} = [\mathbf{C}_1, \mathbf{C}_2, \dots, \mathbf{C}_{20}], \quad (29)$$

with \mathbf{W} denoting the coefficient matrix and where the coefficients of matrix \mathbf{L} denote the permutations of $\{\xi^p, \eta^r, \zeta^s\}$ for each node $j=1, \dots, 20$.

The second order, polynomial shape functions obtained in this way are illustrated by the example of three node locations in Fig. 7, which are similar to the shape functions of all other nodes. In particular, the shape functions presented correspond to two corner nodes, e.g. $N_1(-1, -1, -1) = 1$ and $N_3(1, -1, -1) = 1$, and one side middle node e.g. $N_2(0, -1, -1) = 1$.

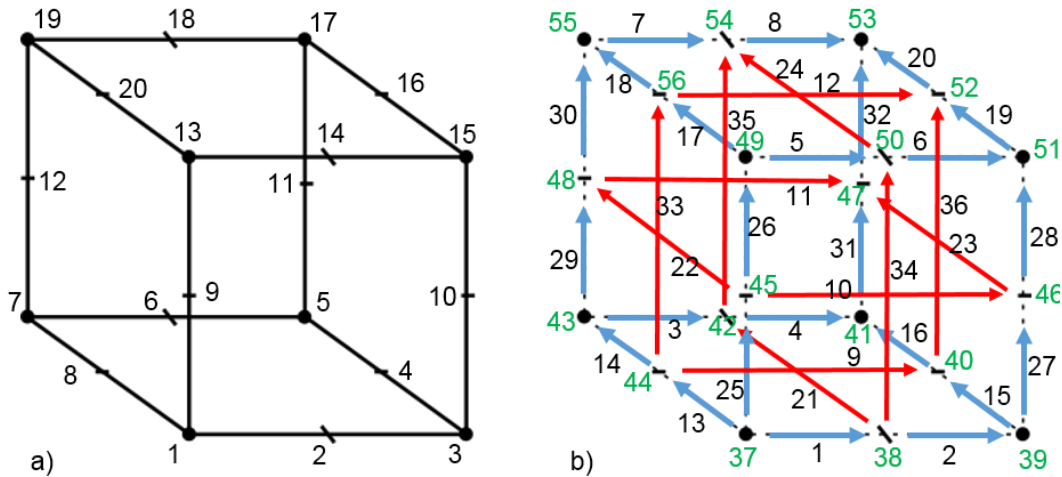


Fig. 6: Classification into nodal or edge based, second order hexahedral elements. a) Nodal finite element with 20 nodes. b) Hybrid finite element with $n_e=36$ edges (1 to 36) and $n_r=20$ nodes (37 to 56).

Discretizing a given problem geometry by hexahedral finite elements, the resulting global continuous finite element mesh consists of arbitrarily shaped hexahedra. These elements can then be transformed into regularly shaped elements in the local coordinate space with the aid of the node based shape functions. If the transformation is done by the same shape functions $N_j(\xi, \eta, \zeta)$, the elements are called isoparametric. In this case, the global coordinate triple (x_j, y_j, z_j) of node j appears in the transformation of the local coordinates into the global ones as follows:

$$\begin{aligned}
 x(\xi, \eta, \zeta) &= \sum_{j=1}^{20} x_j N_j(\xi, \eta, \zeta), \\
 y(\xi, \eta, \zeta) &= \sum_{j=1}^{20} y_j N_j(\xi, \eta, \zeta), \\
 z(\xi, \eta, \zeta) &= \sum_{j=1}^{20} z_j N_j(\xi, \eta, \zeta)
 \end{aligned} \tag{30}$$

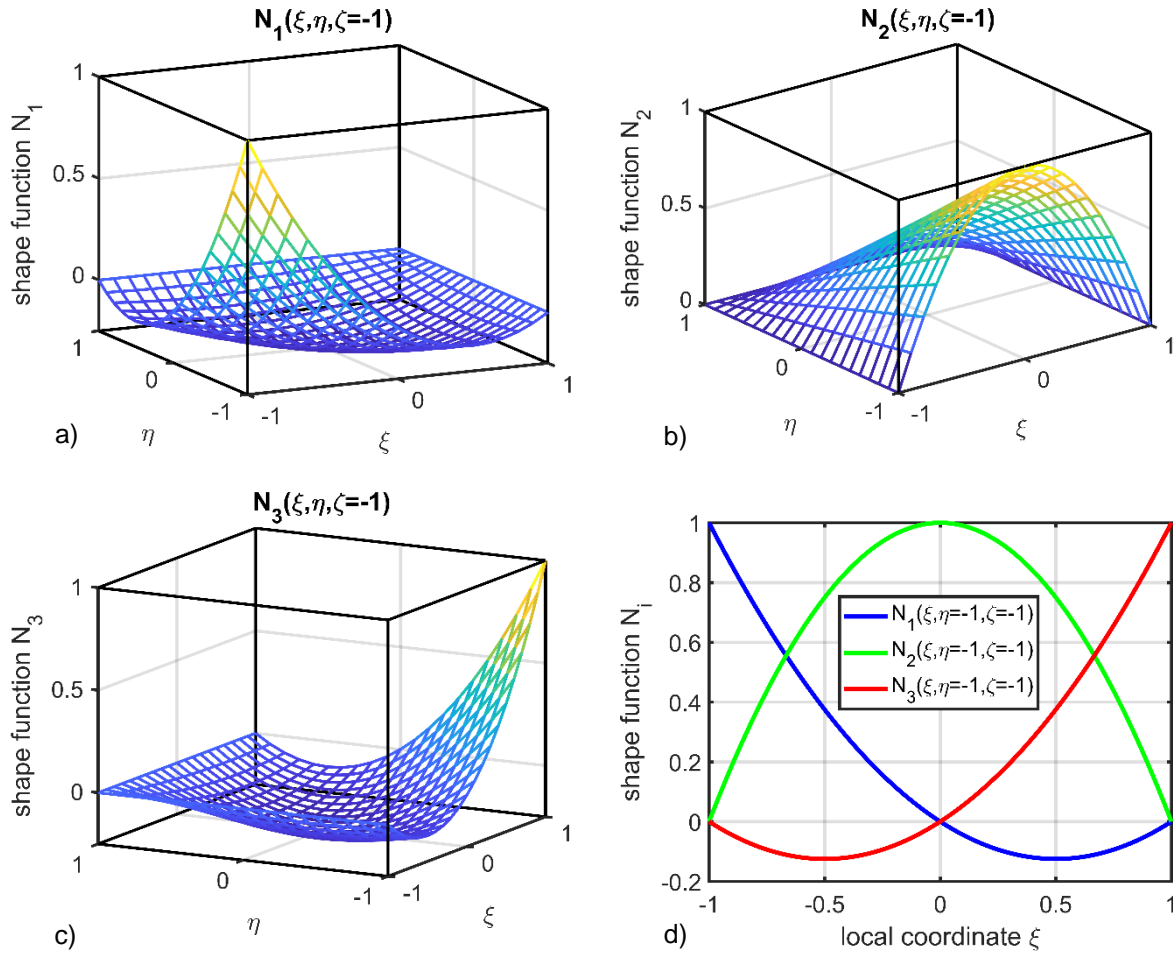


Fig. 7: Illustration of the nodal shape functions N_i in case of three different node locations. a) 3D surface view of a left corner node: $N_1(-1, -1, -1) = 1$ b) 3D surface view of a side middle node: $N_2(0, -1, -1) = 1$ c) 3D surface view of a corner node $N_3(1, -1, -1) = 1$ d) Shape functions N_1, N_2 and N_3 along the local coordinate ξ , while keeping the other coordinates constant: $\eta = \zeta = -1$.

In case of vectorial quantities, it is desirable to use edge-based elements (see Fig. 6b) as this element type imposes continuity of the tangential component only and allows the normal component to be discontinuous. This is in contrast to the nodal representation where full continuity of the normal and tangential component is imposed. In case of certain geometries, especially involving sharp corners or edges formed by interfaces to materials with high relative permeability, the nodal representation can lead to numerical errors and non-physical solutions [7], [8]. However, the vectorial shape functions $\mathbf{N}_j(x, y, z)$ of the edge-based elements satisfy

$$\int_{\text{edge}_i} \mathbf{N}_j(x, y, z) \cdot d\mathbf{s} = \begin{cases} 1 & \text{at edge } i \ (i = j) \\ 0 & \text{at all other edges } (i \neq j) \end{cases} \quad (31)$$

with the global coordinate triple (x, y, z) obtained through the transformation (30) with the aid of the nodal shape functions $N_j(\xi, \eta, \zeta)$. In addition to this property of the edge basis functions,

the gradient of the nodal shape functions can be represented by a linear combination of these edge basis functions $\mathbf{N}_j(x, y, z)$ with the constant coefficients c_{ij} :

$$\text{grad} N_i(\xi, \eta, \zeta) = \sum_{j=1}^{36} c_{ij} \mathbf{N}_j(x, y, z), \text{ with } i = 1, 2, \dots, 20. \quad (32)$$

Using the function defined by the collection of all node-based shape functions $N_j(\xi, \eta, \zeta)$ corresponding to a global node or the collection of all edge-based shape functions $\mathbf{N}_j(x, y, z)$ corresponding to a global edge as the basis function φ_k in (20) or (23), the finite element method is arrived at. By doing this, the resulting system matrices are symmetric and sparse with a small bandwidth along the main diagonal, utilizing a proper numbering of the nodes and/or edges. To solve the resulting algebraic equation systems, classical iterative methods like the conjugate gradient method can be used or direct methods based on Gaussian elimination are applicable [27], [29]. The latter method is suitable to problems with a small number of degrees of freedom (DOF), whereas the iterative method is capable to solve problems with a very large number of DOF. By taking advantage of regularization and preconditioning methods, a speed up of convergence can be achieved [30] - [32]. In case non-linear material properties need to be taken into account, the resulting non-linear equation system can be solved with iterative methods, e.g. direct iteration [35], Newton-Raphson method, fixed-point iteration [33], [34].

3.5 Time discretization

If time dependent electromagnetic field problems are considered, one has to distinguish between different types of time-dependence. In case of time harmonic problems, which can be easily treated in the frequency domain, the variation in time of the fields follows a sinusoidal function with a single frequency. On the other hand, in case of fields changing arbitrarily in time, the electromagnetic field problem has to be formulated in the time domain. Hence, such time transient problems require time discretization schemes to be applied to the finite element equations. A very common method is the use of one-step integration techniques [1], [36]. In particular, the explicit and implicit Euler schemes as well as the Crank Nicolson scheme are common methods. The corresponding recursion formulas are:

$$\begin{aligned}
 \text{Explicit Euler: } & u_{n+1} = u_n + hf(t_n, u_n) \\
 \text{Implicit Euler: } & u_{n+1} = u_n + hf(t_{n+1}, u_{n+1}) \quad , \\
 \text{Crank Nicolson: } & u_{n+1} = u_n + \frac{h}{2} [f(t_n, u_n) + f(t_{n+1}, u_{n+1})]
 \end{aligned} \tag{33}$$

where h denotes the increment in time and the function $f(t, u)$ evaluates to the time derivative

$$\frac{du}{dt} = f(t, u) . \tag{34}$$

The semi-discrete recursion formulas (33) can be combined within one formula as

$$\frac{u_{k+1} - u_k}{\Delta t_k} = \theta f(t_{k+1}, u_{k+1}) + (1 - \theta) f(t_k, u_k) \tag{35}$$

with Δt_k denoting the time step width with $\theta \in [0, 1]$ controlling the influence of the previous time value u_k . For $\theta=0$ we have explicit Euler, $\theta=1$ yields implicit Euler and $\theta=1/2$ corresponds to Crank Nicolson. It should be noted that stability is guaranteed regardless of the time step width provided $1/2 \leq \theta \leq 1$, [36].

Consider now the time dependent problem (24) with time derivative $\{\dot{v}\} = \{\partial v / \partial t\}$. By approximating this derivate as

$$\{\dot{v}\} \approx \frac{\{v_{k+1}\} - \{v_k\}}{\Delta t_k} , \tag{36}$$

and applying (34), the discrete time formulation of this problem is obtained as

$$[\mathbf{A}](\theta \{v_{k+1}\} + (1 - \theta) \{v_k\}) + [\mathbf{M}] \left(\frac{\{v_{k+1}\} - \{v_k\}}{\Delta t_k} \right) = (\theta \{b_{k+1}\} + (1 - \theta) \{b_k\}) . \tag{37}$$

3.6 A potential formulation for magneto-static problems

A potential formulation for the magneto-static problem defined in Tab. 2 will be discussed by introducing a magnetic scalar potential Φ and a current vector potential \mathbf{T}_0 . These potentials are introduced by using Ampere's law and appropriate vector identities [26], [27]. The solenoidality of the magnetic flux density yields the resulting partial differential equation in terms of the scalar and vector potential describing the magnetic field quantities.

By splitting the magnetic field intensity \mathbf{H} into a source term \mathbf{T}_0 and a reduced field intensity \mathbf{H}_r :

$$\mathbf{H} = \mathbf{T}_0 + \mathbf{H}_r , \quad (38)$$

with the vector \mathbf{T}_0 (current vector potential) satisfying

$$\text{curl} \mathbf{T}_0 = \mathbf{J} , \quad (39)$$

the curl of the reduced magnetic field intensity \mathbf{H}_r results to be zero:

$$\text{curl} \mathbf{H}_r = 0 . \quad (40)$$

The condition (40) can be satisfied if the reduced magnetic field intensity \mathbf{H}_r is described with the aid of a reduced scalar potential as

$$\mathbf{H}_r = -\text{grad} \Phi . \quad (41)$$

Therefore, the magnetic field intensity can be written as

$$\mathbf{H} = \mathbf{T}_0 - \text{grad} \Phi , \quad (42)$$

leading to the partial differential equation

$$-\text{div}(\mu \text{grad} \Phi) = -\text{div}(\mu \mathbf{T}_0) \quad (43)$$

by utilizing (6) and the solenoidality of the magnetic flux density (3). Writing the boundary conditions given in Tab. 2 with the aid of the potentials, the boundary value problem of the magneto-static problem can be summarised as shown in Tab. 4. If Galerkin's method is applied to this boundary value problem, the resulting equation system becomes symmetric using nodal basis functions to represent the scalar potential Φ .

Equation/Condition	Domain	
$-\text{div}(\mu \text{grad}\Phi) = -\text{div}(\mu \mathbf{T}_0)$	Ω	(44)
$\Phi = \Phi_0$	Γ_H	
$\mu \text{grad}\Phi \cdot \mathbf{n} = \mu \frac{\partial \Phi}{\partial n} = b + \mu \mathbf{T}_0 \cdot \mathbf{n}$	Γ_B	(45)

Tab. 4: Summary of the magneto-static boundary value problem in terms of the scalar potential Φ and the current vector potential \mathbf{T}_0 .

The advantageous use of the current vector potential \mathbf{T}_0 avoids the necessity of modelling the conductor structure, e.g. coils that carry the exciting current \mathbf{J} . The current vector potential \mathbf{T}_0 can be defined as the magnetic field intensity \mathbf{H}_s obtained by Biot-Savart's law

$$\mathbf{H}_s(r) = \frac{1}{4\pi} \int_{\Omega} \frac{\mathbf{J}_0 \times (\mathbf{r} - \mathbf{r}')}{|\mathbf{r} - \mathbf{r}'|^3} d\Omega', \quad (46)$$

or by approximating the current vector potential \mathbf{T}_0 with the aid of the edge basis functions (31)

$$\mathbf{T}_0 \approx \sum_{k=1}^{n_e} t_k \mathbf{N}_k \quad (47)$$

where n_e is the number of edges of the finite element mesh, and the coefficient t_k represents the line integral of the source field along the edge k . Further details to this approach can be found in the Appendix of the present thesis.

3.7 Potential formulations for eddy current problems

In case of quasi-static eddy current problems previously defined in Tab. 3, the problem domain can be split into a conducting and non-conducting domain, Ω_c and Ω_n . In the conducting domain both the magnetic and electric fields need to be considered, whereas only the magnetic field is relevant in the non-conducting domain. For this type of electromagnetic field problem two potential formulations are considered [7]. First, a magnetic vector potential \mathbf{A} and an electric scalar potential V is used to describe the field quantities. Second, a current vector potential \mathbf{T} and a scalar potential Φ are used.

3.7.1 \mathbf{A} , V - \mathbf{A} formulation

By taking advantage of the solenoidality of the magnetic flux density \mathbf{B} , the magnetic vector potential \mathbf{A} can be introduced satisfying

$$\mathbf{B} = \text{curl } \mathbf{A}, \text{ in } \Omega_c \cup \Omega_n . \quad (48)$$

Using this magnetic vector potential \mathbf{A} and by defining the electric scalar potential V , the electric field intensity \mathbf{E} in the conductive region can be written as

$$\mathbf{E} = -\frac{\partial \mathbf{A}}{\partial t} - \text{grad} \left(\frac{\partial V}{\partial t} \right), \text{ in } \Omega_c \quad (49)$$

where taking the time derivative of the scalar potential ensures symmetry in the resulting equation system after applying Galerkin's method to the corresponding partial differential equations.

The resulting boundary value problem is defined and summarised in Tab. 5, with the material properties $\mathbf{J} = \sigma \mathbf{E}$ and $\mathbf{H} = 1/\mu \mathbf{B} = \nu \mathbf{B}$ taken into account and having substituted (48) and (49) into Ampère's law and the continuity law of the current density. By specifying a constant scalar potential V_0 on the boundary Γ_{Ec} , the voltage excitation of the eddy current problem can be taken into account. Conversely, the current excitation with a given current I is possible by introducing the scalar potential V_0 as an unknown constant potential [10]. The additional relationship

$$-\int_{\Gamma_{Ec}} \sigma \left(\frac{\partial \mathbf{A}}{\partial t} + \text{grad} \frac{\partial V}{\partial t} \right) \cdot \mathbf{n} d\Gamma = I \quad (50)$$

has to be satisfied as well. If Galerkin's method is applied to the following boundary value problem, it is advantageous to use edge basis functions to represent the magnetic vector potential and nodal basis functions for the scalar potential [11]. If doing so, the resulting equation system is singular and symmetric [7]. The singularity results from the fact that the gradient of the nodal basis functions can be obtained as a linear combination of the edge basis functions (see (32)). When applying a conjugate gradient method for solving this singular

equation system, the right hand side of the equations system must be consistent. In case direct methods are used for solving, the singularity need to be eliminated, which is usually done by tree-cotree gauging approaches [12]. Since, the magnetic vector potential and the scalar potential is defined over the whole domain $\Omega = \Omega_c \cup \Omega_n$, the number of degrees of freedom is rather high. Moreover, the necessity of modelling the conductors carrying the exciting sources further increases the numerical burden.

Equation/Condition	Domain	
$\text{curl}(\nu \text{curl} \mathbf{A}) + \sigma \left[\frac{\partial \mathbf{A}}{\partial t} + \text{grad} \left(\frac{\partial V}{\partial t} \right) \right] = \mathbf{0}$	Ω_c	(51)
$-\text{div} \left(\sigma \left(\frac{\partial \mathbf{A}}{\partial t} + \text{grad} \left(\frac{\partial V}{\partial t} \right) \right) \right) = 0$	Ω_c	(52)
$\text{curl}(\nu \text{curl} \mathbf{A}) = \mathbf{J}_0$	Ω_n	(53)
$(\nu \text{curl} \mathbf{A}) \times \mathbf{n} = \mathbf{K}$	Γ_{Hn}	
$\mathbf{A} \times \mathbf{n} = \boldsymbol{\alpha}$	Γ_{Bn}	
$(\nu \text{curl} \mathbf{A}) \times \mathbf{n} = \mathbf{0}$, and $\sigma (-\partial \mathbf{A} / \partial t - \text{grad} \partial V / \partial t) \cdot \mathbf{n} = 0$	Γ_{Hc}	(54)
$\mathbf{A} \times \mathbf{n} = \mathbf{0}$, and $V = \text{constant} = V_0$	Γ_{Ec}	
$(\nu_c \text{curl} \mathbf{A}_c) \times \mathbf{n}_c + (\nu_n \text{curl} \mathbf{A}_n) \times \mathbf{n}_n = \mathbf{0}$, and $\mathbf{A}_c \times \mathbf{n}_c + \mathbf{A}_n \times \mathbf{n}_n = \mathbf{0}$	Γ_{cn}	

Tab. 5: Eddy current boundary value problem in terms of the $\mathbf{A}, V\text{-}\mathbf{A}$ formulation. Here, the normal component of the magnetic flux density \mathbf{B} is prescribed by the tangential component of the magnetic vector potential \mathbf{A} . The outward surface normal vector of the conducting domain and non-conducting domain are related as $\mathbf{n}_c = -\mathbf{n}_n$.

3.7.2 $\mathbf{T}, \Phi\text{-}\Phi$ formulation

When introducing the $\mathbf{T}, \Phi\text{-}\Phi$ formulation for eddy current problems, the formulation for the magneto-static case (section 3.6) is used in the non-conducting domain Ω_n , whereas the electric and magnetic quantities in the conducting domain Ω_c need to be defined additionally.

The current density \mathbf{J} of the eddy currents in the conductor is divergence free, hence

$$\text{curl} \mathbf{T} = \mathbf{J}, \text{ in } \Omega_c, \quad (55)$$

and the magnetic field intensity \mathbf{H} in the conducting region is given as

$$\mathbf{H} = \mathbf{T}_0 + \mathbf{T} - \text{grad} \Phi, \text{ in } \Omega_c. \quad (56)$$

In addition to the partial differential equation (44) in Ω_n , Faraday's law need to be considered in Ω_c . Substituting the potentials defined in (41) and (55) into Faraday's law, the \mathbf{T}, Φ - Φ formulation of the quasi-static eddy current problem is arrived. Tab. 6 summarizes the partial differential equations and boundary conditions.

When applying Galerkin's method to this boundary value problem, the use of edge basis functions to represent the current vector potential \mathbf{T} and the use of nodal basis functions for the scalar potential Φ is advantageous [7]. The resulting equation system is, again, singular and symmetric. Since the current vector potential is defined in the conducting domain only and the exciting conductor structure need not be modelled, the number of degrees of freedom is significantly lower than in case of the \mathbf{A}, V - \mathbf{A} formulation. The problem of non-simply connected conductor structures, e.g. holes within the conductor, can be tackled by introducing conductors with low conductivity in the holes or cutting domains to enable potential jumps [13].

Equation/Condition	Domain	
$\text{curl}(\rho \text{curl} \mathbf{T}) + \left[\frac{\partial(\mu \mathbf{T})}{\partial t} - \text{grad} \left(\frac{\partial(\mu \Phi)}{\partial t} \right) \right] = - \frac{\partial(\mu \mathbf{T}_0)}{\partial t}$	Ω_c	(57)
$\text{div}(\mu(\mathbf{T} - \text{grad} \Phi)) = - \text{div}(\mu \mathbf{T}_0)$	Ω_c	(58)
$- \text{div}(\mu \text{grad} \Phi) = - \text{div}(\mu \mathbf{T}_0)$	Ω_n	(59)
$\Phi = \text{constant} = \Phi_0$	Γ_{Hn}	
$\frac{\partial(\mu \Phi)}{\partial \mathbf{n}} = b + \mu \mathbf{T}_0 \cdot \mathbf{n}$	Γ_{Bn}	
$\mathbf{T} \times \mathbf{n} = \mathbf{T}_0 \times \mathbf{n} = \mathbf{0}$, and $\Phi = \text{constant} = \Phi_0$	Γ_{Hc}	(60)
$(\rho \text{curl} \mathbf{T}) \times \mathbf{n} = -(\rho \text{curl} \mathbf{T}_0) \times \mathbf{n} = \mathbf{0}$, and $\mu(\mathbf{T} - \text{grad} \Phi) \cdot \mathbf{n} = -\mu \mathbf{T}_0 \cdot \mathbf{n} = 0$	Γ_{Ec}	
$\mathbf{T} \times \mathbf{n} = \mathbf{0}$, and $(\mu_c \mathbf{T}_0 + \mu_c \mathbf{T} - \mu_c \text{grad} \Phi) \cdot \mathbf{n}_c + (\mu_n \mathbf{T}_0 + \mu_n \mathbf{T} - \mu_n \text{grad} \Phi) \cdot \mathbf{n}_n = 0$	Γ_{cn}	

Tab. 6: Eddy current boundary value problem in terms of the \mathbf{T}, Φ - Φ formulation.

4 Non-conforming mesh connection method

In the present section, a non-conforming mesh method is introduced and discussed as applied to the Poisson equation. In particular, the static magnetic field problem formulated by a scalar potential is considered (see section 3.6). This setting is equivalent to the electrostatic or stationary current field problem. The coupling method introduced in section 4.1 can be used in all these field problems, since it uses the degrees of freedom of the nodes, e.g. the electric or magnetic scalar potential, to couple two disjoint domains with their meshes being non-matching and thus featuring hanging nodes at a so-called sliding surface. The non-conforming mesh method follows the approach of [45] where the interpolation technique was first introduced for tetrahedral elements and revisited in [46].

4.1 Coupling of nodes/potentials

For the sake of simplicity, the basic idea of the non-conforming mesh method is introduced with a two dimensional (2D) finite element mesh with second order quadrilateral elements as example. Consider two disjoint subdomains Ω^M and Ω^S of the problem domain $\Omega = \Omega^M \cup \Omega^S$ with the sliding surface Γ_S being the interface between them (see Fig. 8). Along this interface Γ_S , the two meshes of the domains Ω^M and Ω^S are allowed to be non-matching with so called hanging nodes. This non-conformance of the overall mesh can be caused either through the relative movement between Ω^M and Ω^S (the domains become displaced relative to each other), or due to different mesh topologies of the two domains Ω^M and Ω^S . Once the sliding surface has been defined, master nodes m_l and slave nodes s_k can be defined along this surface implicitly defining the master domain Ω^M and the slave domain Ω^S . The nodes that do not belong to this sliding surface Γ_S , will be called regular nodes n_R .

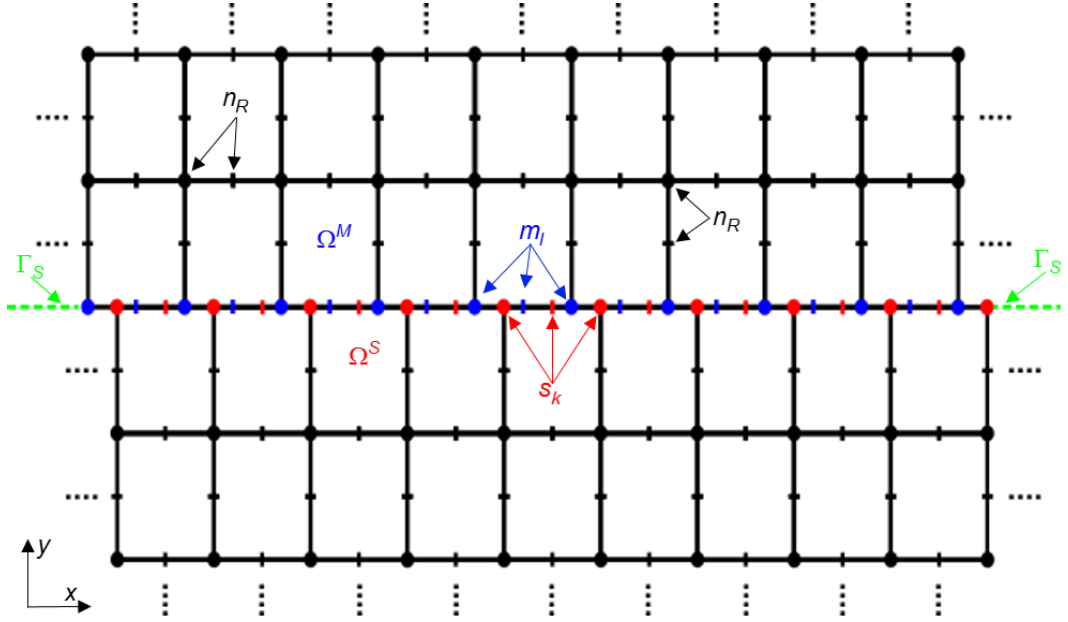


Fig. 8: Illustrative, two dimensional example of a non-conforming finite element mesh with quadrilateral elements. The overall mesh is allowed to be non-conforming with hanging nodes along the sliding surface Γ_S . Master and slave nodes, m_i and s_k can be defined along Γ_S .

The degrees of freedom (e.g. the electric or magnetic scalar potential Φ) of each slave node is replaced by a linear combination of the degrees of freedom of the corresponding master nodes. The set of the indices of the corresponding master nodes of a slave nodes is denoted by $S_k^{(master)}$, and with $L_k^{(master)}$ denoting the number of corresponding master nodes. Hence, the degree of freedom of the slave node $\Phi_k^{(slave)}$ at the space coordinates $\mathbf{r}_k^{(slave)}$ is written as:

$$\Phi_k^{(slave)} = \Phi(\mathbf{r}_k^{(slave)}) = \sum_{l \in S_k^{(master)}} c_{kl} \Phi_l^{(master)} \quad (61)$$

with $\Phi_l^{(master)}$ denoting the degrees of freedom of the master nodes. The coupling factor c_{kl} is obtained with the aid of the node-based shape function N_l of the master node m_l . In particular, the value of the coupling factor is obtained by the evaluation of the shape function at the space coordinates $\mathbf{r}_k^{(slave)}$ of the slave node s_k ,

$$c_{kl} = N_l^{(master)}(\mathbf{r}_k^{(slave)}). \quad (62)$$

The computation of the coupling coefficients for a slave node along the sliding surface is illustrated in Fig. 9 for an example of a planar 2D non-conforming mesh consisting of second order quadrilateral elements with the slave node s_k at position $\mathbf{r}_k^{(slave)}$ corresponding to three master nodes, i.e. $L_k^{(master)} = 3$. The example is shown in Fig. 9a, and detailed in Fig. 9b. In the latter figure, the localisation of the slave node s_k is shown in the local coordinate system of the master element at position $\tilde{\mathbf{r}}_k$.

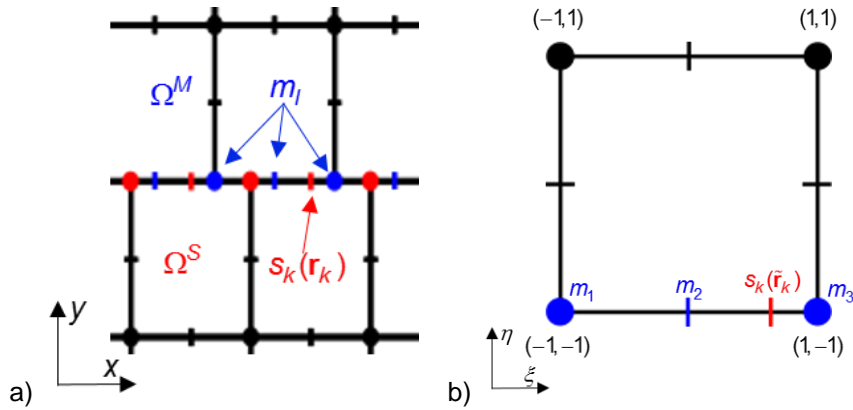


Fig. 9: Coupling situation of a slave node s_k in case of a two dimensional non-conforming mesh. a) Global position of the slave node at its space coordinates r_k . b) Localisation of the slave node within the local coordinate system of the master element.

If the location of the slave node s_k is given by $\xi = 0.6$ and $\eta = -1$, the coupling coefficients c_{kl} , $l \in [1,3]$ evaluate to $c_{k1} = -0.12$ for the left end node m_1 with the shape function N_1 , $c_{k3} = 0.48$ for the right end node m_3 with the shape function N_3 and $c_{k2} = 0.64$ for the middle node m_2 with the shape function N_2 . The coupling coefficients and shape functions of the master nodes are illustrated in Fig. 10. It is obvious to assume that the coupling coefficients evaluate to values less or equal to one: $c_{kl} \leq 1$ if the local coordinates are between $\{\xi, \eta\} \in \{-1, 1\}$.

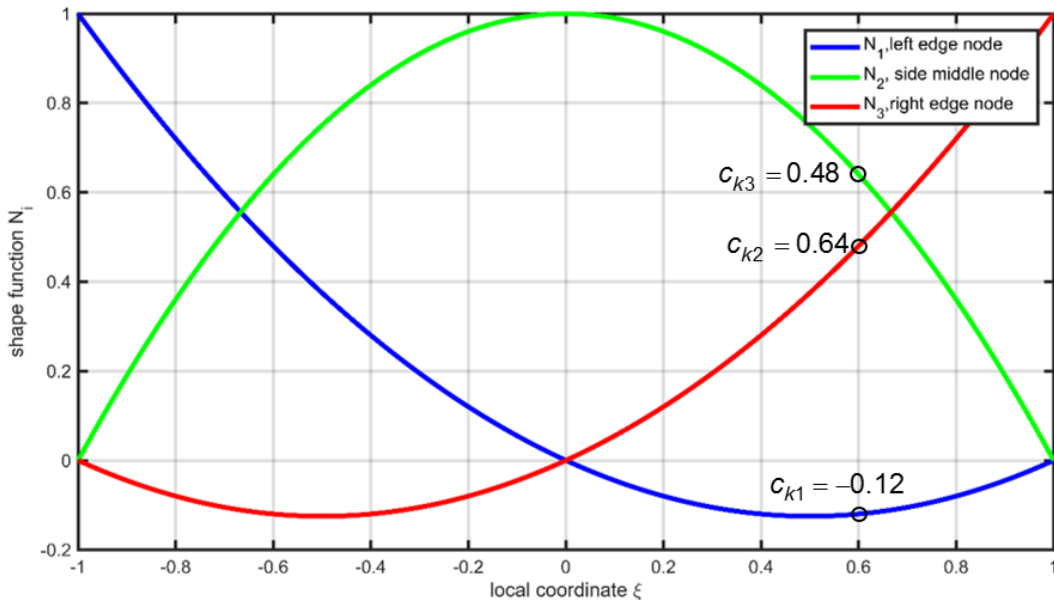


Fig. 10: Coupling coefficients and shape functions of corresponding master nodes in case of slave node s_k located at $\xi=0.6$ and $\eta=-1$.

The extension to a three dimensional (3D) problem and finite element mesh is simple. In case of 3D problems, the sliding interface Γ_S consist of element surfaces instead of lines as in the 2D case. Depending on the element type used (e.g. tetrahedral or hexahedral elements), the number of slave nodes and master nodes along the sliding surface will be higher than in the 2D case. The number of corresponding master nodes $L_k^{(master)}$ is at least equal to the number of nodes that belong to the facet of the finite element which is part of the sliding interface Γ_S . In the present work, hexahedral elements of second order are used. Therefore, the number of corresponding master nodes satisfies $L_k^{(master)} \geq 8$. Consider a stationary master domain Ω^M and slave domain Ω^S with a non-matching mesh along the sliding interface Γ_S as illustrated for a planar problem in Fig. 11a. In particular, the coupling situation for two nodes s_1 and s_2 is shown in detail along the sliding surface in Fig. 11b. First, consider the case of slave node s_1 which is aligned with the facet separating the neighbouring master elements M_1 and M_5 . This slave node hence corresponds to the master nodes of both master elements M_1 and M_5 . Obviously, the nodes of either master element M_1 or those of M_5 can be chosen to constitute the corresponding set of master nodes. Second, slave node s_2 is considered, which is located on a facet of master element M_1 . It is obvious that only the nodes of master element M_1 can be selected as master nodes of the slave node s_2 . In both cases, the set of corresponding master nodes for each slave node consists of $L_k^{(master)} = 8$ master nodes.

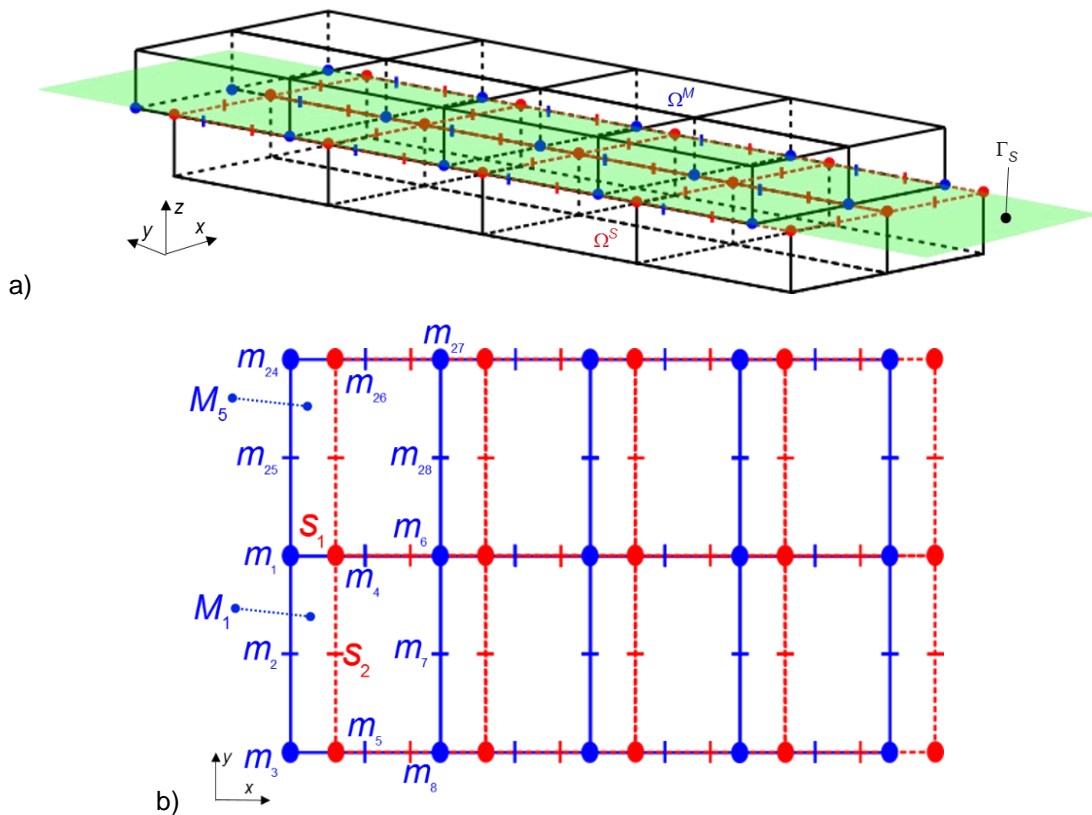


Fig. 11: Coupling situation in case of 3D problems. a) Non-conforming mesh along the sliding surface Γ_S . b) Top view of the coupling situation for two slave nodes in detail at the sliding surface.

4.2 Reformulating the Galerkin equations of the magneto-static field problem

The magneto-static field problem leads to a second order differential equation of the Poisson type in the problem domain Ω with boundary conditions defined in section 3.6. After discretizing the problem domain and applying Galerkin techniques (see section 3.3 and 3.4), an algebraic equation system can be established. The ansatz function of the magnetic scalar potential Φ is

$$\Phi \approx \Phi_n = \sum_{k=1}^{n_{node}} \varphi_k N_k \quad (63)$$

with the node-based polynomial shape functions N_k , the nodal values φ_k of the magnetic scalar potential Φ_n and the number of nodes denoted by n_{node} . Hence, the equation system can be written as

$$\begin{aligned} \sum_{j=1}^{n_{node}} \varphi_j \int_{\Omega} \text{grad} N_i \cdot \mu \text{grad} N_j d\Omega = \int_{\Omega} \text{grad} N_i \cdot \mu \mathbf{T}_0 d\Omega + \int_{\Gamma_B} N_i b d\Gamma \\ - \int_{\Omega} \text{grad} N_i \cdot \mu \text{grad} \Phi_D d\Omega, \text{ with } i = 1, 2, \dots, n \end{aligned} \quad (64)$$

where \mathbf{T}_0 is the current vector density and its curl describes the impressed current density \mathbf{J}_0 . The matrix of this equation system (64) is sparse, symmetric and positive definite and can be solved by classical iterative solvers.

Taking the interpolation of the slave node potential (61) into account, the ansatz function (63) can be rewritten as

$$\begin{aligned} \Phi_n(\mathbf{r}) = \sum_{l=1}^{L^{(regular)}} \Phi_l^{(regular)} N_l^{(regular)} + \\ + \sum_{l=1}^{L^{(master)}} \Phi_l^{(master)} \left(N_l^{(master)}(\mathbf{r}) + \sum_{k=1}^{L^{(slave)}} c_{kl} N_k^{(slave)}(\mathbf{r}) \right), \end{aligned} \quad (65)$$

where the superscripts stand for the regular, master and slave nodes, and where the last term reflects the coupling of the nodal potentials (61).

Applying (65) to the Galerkin equations (64), these can be rewritten as two sets of equations:

$$\begin{aligned} & \sum_{k=1}^{L^{(regular)}} \varphi_k^{(regular)} \int_{\Omega} \text{grad} N_i^{(regular)} \cdot \mu \text{grad} N_k^{(regular)} d\Omega + \sum_{k=1}^{L^{(master)}} \varphi_k^{(master)} \int_{\Omega} \text{grad} N_i^{(regular)} \cdot \mu \Psi_k d\Omega = \\ & \int_{\Omega} \text{grad} N_i^{(regular)} \cdot \mu \mathbf{T}_0 d\Omega + \int_{\Gamma_B} N_i^{(regular)} b d\Gamma - \int_{\Omega} \text{grad} N_i^{(regular)} \cdot \mu \text{grad} \Phi_D d\Omega \quad (i = 1, 2, \dots, L^{(regular)}) \end{aligned} \quad (66)$$

$$\begin{aligned} & \sum_{k=1}^{L^{(regular)}} \varphi_k^{(regular)} \int_{\Omega} \Psi_i \cdot \mu \text{grad} N_k^{(regular)} d\Omega + \sum_{k=1}^{L^{(master)}} \varphi_k^{(master)} \int_{\Omega} \Psi_i \cdot \mu \Psi_k d\Omega = \int_{\Omega} \Psi_i \cdot \mu \mathbf{T}_0 d\Omega + \\ & + \int_{\Gamma_B} \left(N_i^{(master)} + \sum_{k=1}^{L^{(slave)}} c_{kl} N_k^{(slave)} \right) b d\Gamma - \int_{\Omega} \Psi_i \cdot \mu \text{grad} \Phi_D d\Omega \quad (i = 1, 2, \dots, L^{(master)}). \end{aligned} \quad (67)$$

The interpolation of the slave potential is taken into account by the function Ψ_k denoted by

$$\Psi_k = \text{grad} N_k^{(master)} + \sum_{l=1}^{L^{(slave)}} c_{kl} \text{grad} N_l^{(slave)}. \quad (68)$$

At this point it should be noted that mixed terms including both master and slave shape functions do not appear, since the two types of shape functions are disjoint.

Of the two sets of Galerkin equations (66) and (67), the latter takes account of the interpolation of the slave potential. They can be written in matrix form as

$$\begin{pmatrix} \mathbf{A}_{RR} & \mathbf{A}_{RM} + \mathbf{A}_{RS} \mathbf{C} \\ \mathbf{C}^T \mathbf{A}_{RS}^T + \mathbf{A}_{RM}^T & \mathbf{A}_{MM} + \mathbf{C}^T \mathbf{A}_{SS} \mathbf{C} \end{pmatrix} \begin{pmatrix} \mathbf{X}_R \\ \mathbf{X}_M \end{pmatrix} = \begin{pmatrix} \mathbf{b}_R \\ \mathbf{b}_M + \mathbf{C}^T \mathbf{b}_{RS} \end{pmatrix} \quad (69)$$

where the subscripts R , M and S of the coefficient matrix \mathbf{A}_{ij} stand for the regular, master and slave nodes. The coupling to the slave nodes is represented by the rectangular matrices \mathbf{C} and \mathbf{A}_{ij} containing the coupling terms. However, the matrices \mathbf{A}_{ii} are symmetric and the overall system matrix obtained is sparse, symmetric and positive definite. The coefficients of the matrices are:

$$\begin{aligned} a_{ij}^{RR} &= \int_{\Omega} \text{grad} N_i^{(regular)} \cdot \mu \text{grad} N_j^{(regular)} d\Omega, \\ & \text{with: } i = 1, 2, \dots, L^{(regular)} \text{ and } j = 1, 2, \dots, L^{(regular)}, \end{aligned} \quad (70)$$

$$\begin{aligned} a_{ij}^{RM} &= \int_{\Omega} \text{grad} N_i^{(regular)} \cdot \mu \text{grad} N_j^{(master)} d\Omega, \\ & \text{with: } i = 1, 2, \dots, L^{(regular)} \text{ and } j = 1, 2, \dots, L^{(master)}, \end{aligned} \quad (71)$$

$$\begin{aligned} a_{ij}^{RS} &= \int_{\Omega} \text{grad} N_i^{(regular)} \cdot \mu \text{grad} N_j^{(slave)} d\Omega, \\ & \text{with: } i = 1, 2, \dots, L^{(regular)} \text{ and } j = 1, 2, \dots, L^{(slave)}, \end{aligned} \quad (72)$$

$$a_{ij}^{MM} = \int_{\Omega} \text{grad} N_i^{(master)} \cdot \mu \text{grad} N_j^{(master)} d\Omega , \quad (73)$$

with: $i = 1, 2, \dots, L^{(master)}$ and $j = 1, 2, \dots, L^{(master)}$,

$$a_{ij}^{SS} = \int_{\Omega} \text{grad} N_i^{(slave)} \cdot \mu \text{grad} N_j^{(slave)} d\Omega , \quad (74)$$

with: $i = 1, 2, \dots, L^{(slave)}$ and $j = 1, 2, \dots, L^{(slave)}$,

$$c_{ij} = N_j^{(master)}(\mathbf{r}_i^{(slave)}) , \quad (75)$$

with: $i = 1, 2, \dots, L^{(slave)}$ and $j = 1, 2, \dots, L^{(master)}$,

where the superscripts indicate the corresponding matrices of equation system (69). The coefficients of the right hand side of (69) are given as:

$$b_R = \int_{\Omega} \text{grad} N_i^{(regular)} \cdot \mu \mathbf{T}_0 d\Omega + \int_{\Gamma_B} N_i^{(regular)} b d\Gamma - \int_{\Omega} \text{grad} N_i^{(regular)} \cdot \mu \text{grad} \Phi_D d\Omega , \text{ with } i = 1, 2, \dots, L^{(regular)} , \quad (76)$$

$$b_M = \int_{\Omega} \text{grad} N_i^{(master)} \cdot \mu \mathbf{T}_0 d\Omega + \int_{\Gamma_B} N_i^{(master)} b d\Gamma - \int_{\Omega} \text{grad} N_i^{(master)} \cdot \mu \text{grad} \Phi_D d\Omega , \text{ with } i = 1, 2, \dots, L^{(master)} , \quad (77)$$

$$b_{RS} = \int_{\Omega} \text{grad} N_i^{(slave)} \cdot \mu \mathbf{T}_0 d\Omega + \int_{\Gamma_B} N_i^{(slave)} b d\Gamma - \int_{\Omega} \text{grad} N_i^{(slave)} \cdot \mu \text{grad} \Phi_D d\Omega , \text{ with } i = 1, 2, \dots, L^{(slave)} . \quad (78)$$

4.3 Error analysis

In this section, the precision of the non-conforming mesh method introduced in the previous two sections and summarized in (69) is investigated by analysing a simple cylindrical magneto-static boundary value problem with a known exact solution. The model problem imitates the air gap of an electrical machine. There are no source terms, hence the boundary value problem reduces to the following (see Fig. 12):

$$-\operatorname{div}(\mu \operatorname{grad} \Phi) = 0 \text{ in } \Omega, \quad (79)$$

$$\Phi = \Phi_0 \text{ on } \partial\Omega_1, \partial\Omega_2, \quad (80)$$

with the Dirichlet data

$$\Phi_{0,1} = R_i^p \cos(p\phi) \text{ on } \partial\Omega_1, \quad (81)$$

$$\Phi_{0,2} = R_o^p \cos(p\phi) \text{ on } \partial\Omega_2, \quad (82)$$

Where R_i , R_o are the inner and outer radii of the cylinder, ϕ is the azimuthal coordinate and p is the number of pole pairs. Then, the exact solution is:

$$\Phi = r^p \cos(p\phi). \quad (83)$$

In order to impose a strong variation of the potential in azimuthal direction, the number of pole pairs is selected as $p=10$.

The geometry of the cylindrical model with the finite element mesh is shown in Fig. 12a with the inner radius chosen as $R_i=0.54m$, the radius of the sliding surface as $R_m=0.57m$ and the outer radius as $R_o=0.6m$. The length of the cylinder in the axial direction is chosen as $l=1.0m$. The finite element mesh consists of second order hexahedral elements and is obtained by dividing the annuli between R_i and R_m as well as between R_m and R_o , equidistantly into n quadrilateral elements.

As this boundary value problem is independent of the axial coordinate, i.e. essentially two-dimensional, the finite element mesh consists of only one layer in axial direction obtained by extruding these quadrilateral elements in the axial direction along the length l . A detailed view of the finite element mesh in the xy -plane is shown in Fig. 12b. The displacement angle $\Delta\gamma$ is introduced to characterize the degree of non-conformity between the two meshes of the annuli. This displacement angle depends on the number of elements of domain Ω_2 and is defined as

$$\Delta\gamma = \frac{360^\circ}{2n} \alpha \quad (84)$$

where the factor α is in the range of $0 \leq \alpha \leq 1$. Hence, a conforming mesh is characterized by $\alpha=0$, whereas the largest displacement is obtained for $\alpha=1$, where the hanging nodes are in the centres of the opposite element edges. Note that, in order to overcome the problem of a small gap or overlap between the meshes in case of a curved sliding surface, a tolerance for

the distance between the slave node and the facet master nodes has been introduced. A value of 10^{-6} (normalized with the size of the master element) has turned out to be appropriate.

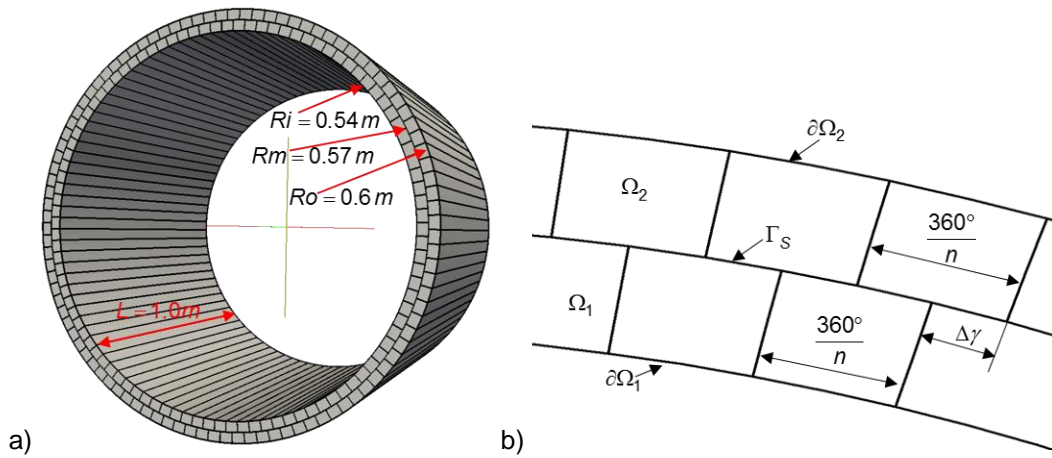


Fig. 12: Problem model for the error analysis. a) 3D view of the cylindrical model with the non-matching meshes. b) Detailed view of the non-conforming mesh with equidistant elements along the sliding surface.

Using this simple cylindrical model, two experiments have been carried out to evaluate the accuracy of the non-conforming mesh method. First, the number of elements has been increased from $n=100$ up to $n=1500$ in both domains, and the relative movement between the domains Ω_1 and Ω_2 has been modelled. This relative movement is taken into account by increasing the displacement angle $\Delta\gamma$ invoked by varying the value of α as $\alpha = 0.1, 0.2, \dots, 1.0$. In the second experiment, the same accuracy investigation has been carried out, but here the number of elements is different in the two domains Ω_1 and Ω_2 . The number of elements in the domain Ω_2 has again been increased from $n=100$ up to $n=1500$, whereas the number of elements in the domain Ω_1 has been taken to be a multiple of n and chosen as $2n, 3n$. The mesh topologies of these two experiments in case of $n=400$ are shown in Fig. 13.

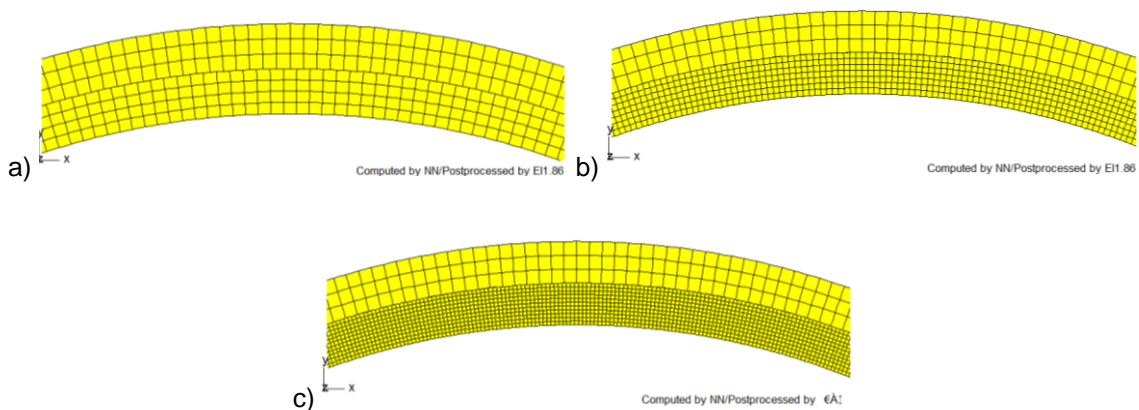


Fig. 13: Different mesh topologies considered for the error analysis. a) Equal number of elements in the two domains Ω_1 and Ω_2 . b) Different number of elements in the two domains Ω_1 : $2n$ and Ω_2 : n c) Different number of elements in the two domains Ω_1 : $3n$ and Ω_2 : n .

The solutions obtained by both experiments are quantified by an error ε_n , which uses the exact analytical solution Φ obtained with (83) and the numerical values $\tilde{\Phi}_k$ at particular evaluation points:

$$\varepsilon_n = \frac{\sqrt{\sum_{k=1}^{N_p} (\Phi_k - \tilde{\Phi}_k)^2}}{\max_{1 \leq k \leq N_p} \{|\Phi_k|\}}. \quad (85)$$

The numerical values $\tilde{\Phi}_k$ are taken along a circular line in the vicinity of the slip surface Γ_S at the radii $R_1=0.571m$ and $R_2=0.569m$, for the master domain Ω_2 and the slave domain Ω_1 , respectively. As the solution is of periodic nature, it is sufficient to consider one period of the solution. Hence, the numerical values $\tilde{\Phi}_k$ are taken in the azimuthal range of $0^\circ < \beta < 36^\circ$ degrees at $N_p=720$ equidistant evaluation points.

The magnetic scalar potential Φ is shown and compared in Fig. 14 and Fig. 15 for the case of $n=400$ finite elements. The solution obtained by a conforming mesh between Ω_1 and Ω_2 is shown in Fig. 14a. Fig. 14b illustrates the magnetic scalar potential in case of the non-conforming mesh. The solutions obtained in the second experiment with a different number of elements in the master and slave domains are shown in Fig. 15a for the case of Ω_1 : $2n$ elements, and in Fig. 15b for Ω_1 : $3n$ elements.

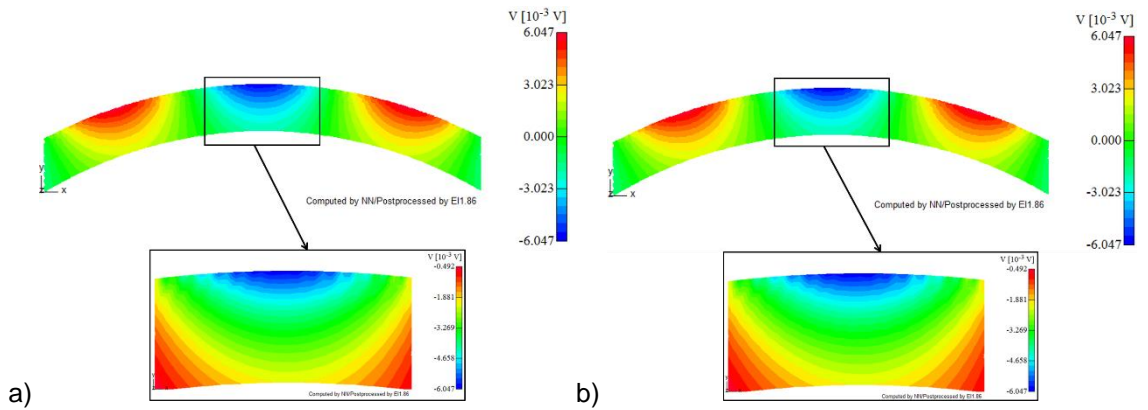


Fig. 14: Comparison of the magnetic scalar potential. a) conforming mesh b) non-conforming mesh with equal number of elements in both domains Ω_1 and Ω_2 .

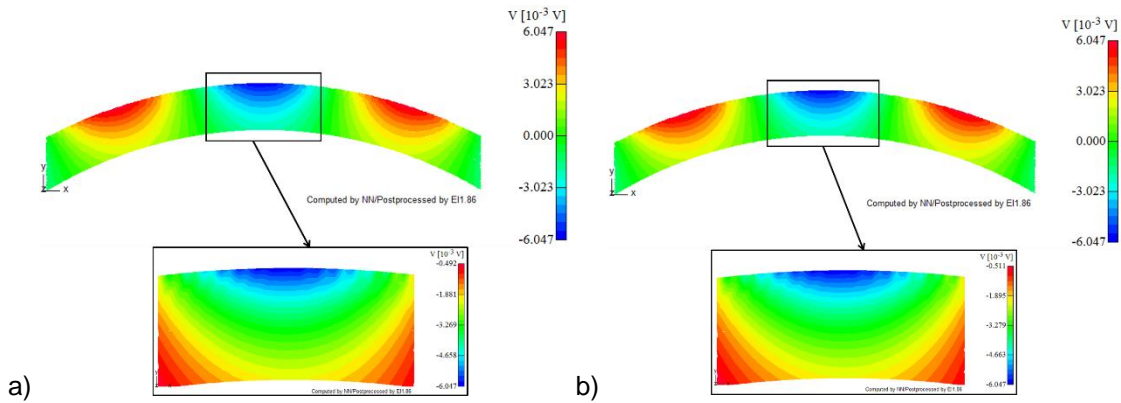


Fig. 15: Comparison of the magnetic scalar potential in case of different number of elements in both domains Ω_1 and Ω_2 . a) $\Omega_1:2n$ and $\Omega_2:n$ b) $\Omega_1: 3n$ and $\Omega_2: n$.

The field plots of the magnetic scalar potential compared in Fig. 14 and Fig. 15 indicate that the solutions of both experiments are reasonable and in a good agreement with the analytical solution. In the two cases where a different number of elements in the two domains Ω_1 and Ω_2 is considered, the field plots in Fig. 15 also indicate reasonable solutions and a good agreement with the analytical solution. These observations are substantiated by the comparison of the numerical values $\tilde{\Phi}_k$ with the analytical solution of the scalar potential in Fig. 17. The numerical values $\tilde{\Phi}_k$ along the circular line with $R_2=0.569m$ are shown here for all considered cases with $n=400$ elements.

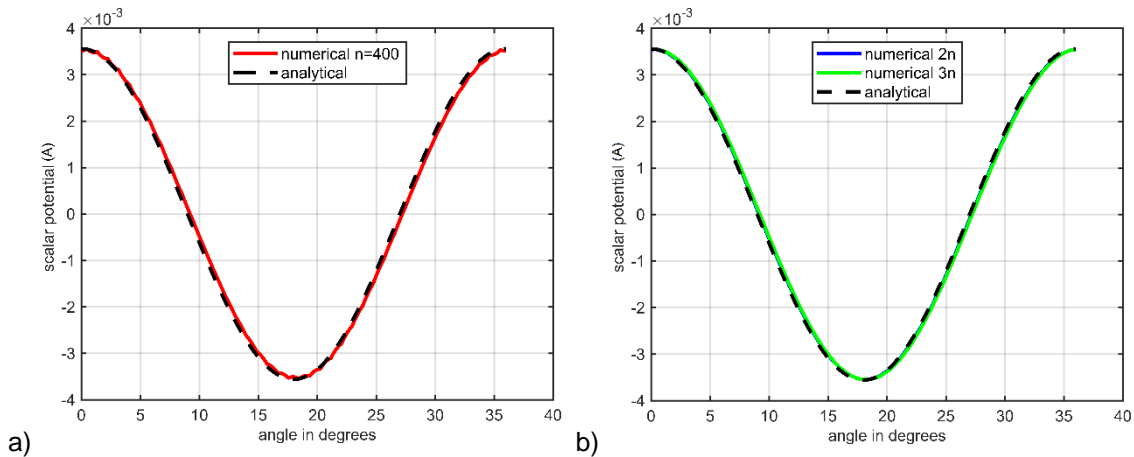


Fig. 16: Numerical values of the magnetic scalar potential along the circular line with radius $R_2=0.569m$ for $n=400$ elements. a) Comparison of the analytical solution with the non-conforming case with equal number of elements in both domains Ω_1 and Ω_2 . b) Numerical values obtained in the two cases with different number of elements in the two domains. First, $\Omega_1:2n$ and second $\Omega_1:3n$ and $\Omega_2:n$ (numerical $3n$).

The error ε_n of the obtained numerical values $\tilde{\Phi}_k$ along the curved lines at $R_1=0.571m$ and $R_2=0.569m$ defined in (85) is compared in Fig. 17 for two cases of displacement with $\alpha=0.0$ (conforming mesh) and $\alpha=1.0$ (worst non-conforming mesh case). In addition, the error in case of $\alpha=1.0$ and at R_2 is shown for different numbers of elements in the two domains Ω_1 and Ω_2 . The error ε_n is plotted in logarithmic scale against the number of elements n , with the curves showing identical convergence rates with a slope close to -2. This behaviour corresponds well to the theoretical result for second order elements predicting the error to decrease in a quadratic manner [1]. The error ε_n obtained for the second experiment is larger than in the case of an equal number of elements, but it converges again with a slope close to -2. It is reasonable to assume that there is a certain limit on increasing the number of elements for the slave domain Ω_1 , as in case of $\Omega_1: 3n$ the error ε_n is almost one decade larger than the error obtained in the case of the first experiment. It is, therefore, obvious to suggest to limit the ratio between the number of elements n_{EL}^{master} in the master domain to n_{EL}^{slave} in the slave domain.

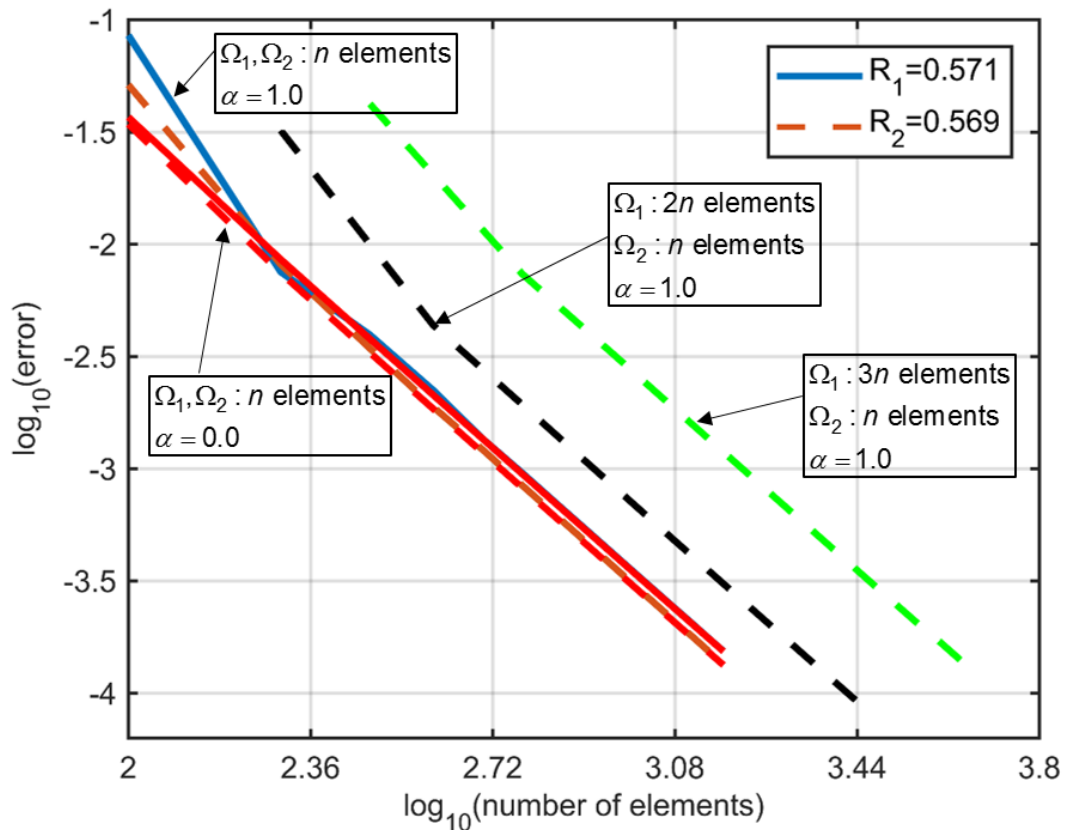


Fig. 17: Error plotted as a function of the number of elements in logarithmic scale, both at R_1 (solid lines) and R_2 (dashed lines). The case of $\alpha=0$ corresponds to a conforming mesh, $\alpha=1.0$ to a maximally non-conforming one. The convergence rate indicated by all curves is almost the same with a slope close to -2, indicating quadratic convergence.

On the basis of the observations made, a third experiment has been carried out to obtain a recommendation of the limit on the ratio δ between the number of elements n_{EL}^{master} in the master domain to n_{EL}^{slave} in the slave domain.

$$\delta = \frac{n_{EL}^{master}}{n_{EL}^{slave}} \quad (86)$$

In this third experiment, the ratio (86) characterizes the finite element mesh density along the sliding surface of the master and slave domain (Ω_2 and Ω_1), and is varied between $0.1 \leq \delta \leq 3.0$. In case of $0.1 \leq \delta < 1.0$, the finite element mesh of the slave domain is finer than that of the master domain, and in case of $1.0 < \delta \leq 3.0$ the refinement of the finite element mesh is opposite to first case. If the ratio is equal to one: $\delta = 1.0$, the mesh density is equal in both domains Ω_2 and Ω_1 with a number of elements $n_{EL}^{master} = n_{EL}^{slave} = 600$. In addition to the variation of δ , the degree of displacement between the two domains Ω_2 and Ω_1 is also varied. The error ε_n defined in (85) is compared for different degrees of displacement $0.1 \leq \alpha \leq 1.0$ in Fig. 18 and detailed in Fig. 19. It is obvious that the solutions become incorrect if the ratio of the mesh density is increased beyond a certain limit. Apparently, this limit is approximately at $\delta = 1.4$. Hence, it is suggested to use a ratio between the number of elements n_{EL}^{master} in the master domain to n_{EL}^{slave} in the slave domain which is within the interval: $0.1 \leq \delta < 1.4$. By choosing a ratio within this interval, reliable solutions with a small error can be obtained.

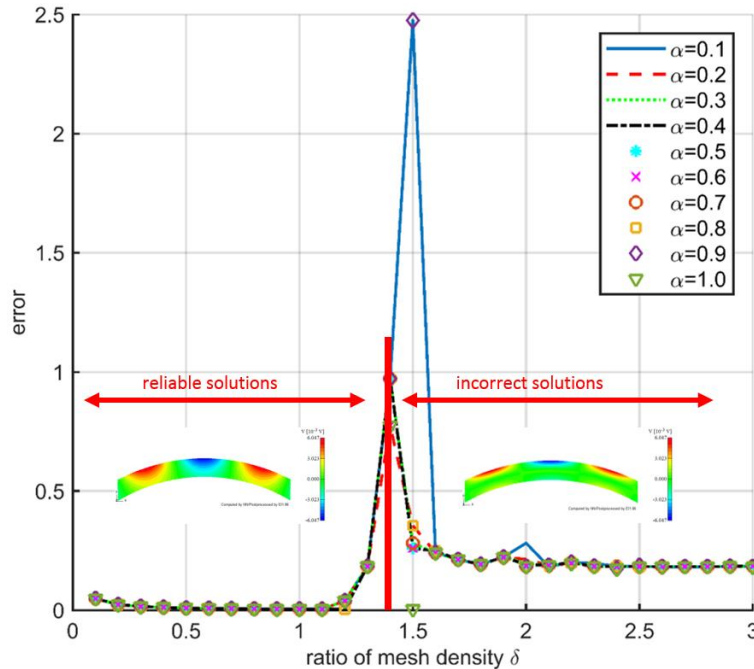


Fig. 18: Error depending on the ratio δ between the number of elements n_{EL}^{master} in the master domain to n_{EL}^{slave} in the slave domain. In case of the ratio of mesh density is $\delta < 1.4$, reliable solutions can be obtained. If the ratio is increased further, incorrect solutions are obtained. Therefore it is suggested to use a ratio of $0.1 \leq \delta < 1.4$.

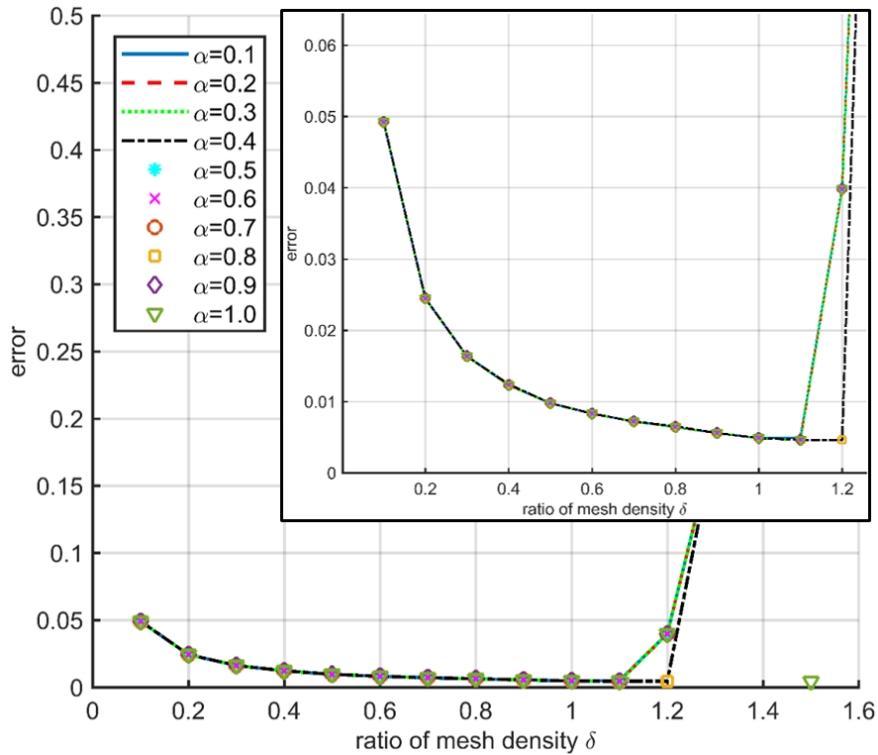


Fig. 19: A detailed plot of the error ε_n depending on the ratio of mesh density. Apparently, the error is smallest if the ratio is near to one. As in detail shown, the error decreases in quadratic manner when increasing the number of elements.

In the following, the error ε_n for the master domain at radius R_1 is investigated in Fig. 20 showing its dependence on the displacement angle $\Delta\gamma$ and on the number of finite elements being increased from $n=100$ up to $n=1500$. Fig. 21 shows the same error comparisons for the slave domain at radius R_2 . It can be seen in both figures that the error ε_n becomes larger with increasing degree of displacement. As expected, the largest error occurs at a displacement angle $\Delta\gamma$ with $\alpha=1.0$ (see (84)) where the hanging nodes are in the centres of the opposite element edges. Note that if the number of finite elements is large enough, the error remains almost stable with a slight tendency to become larger at increased displacement angles.

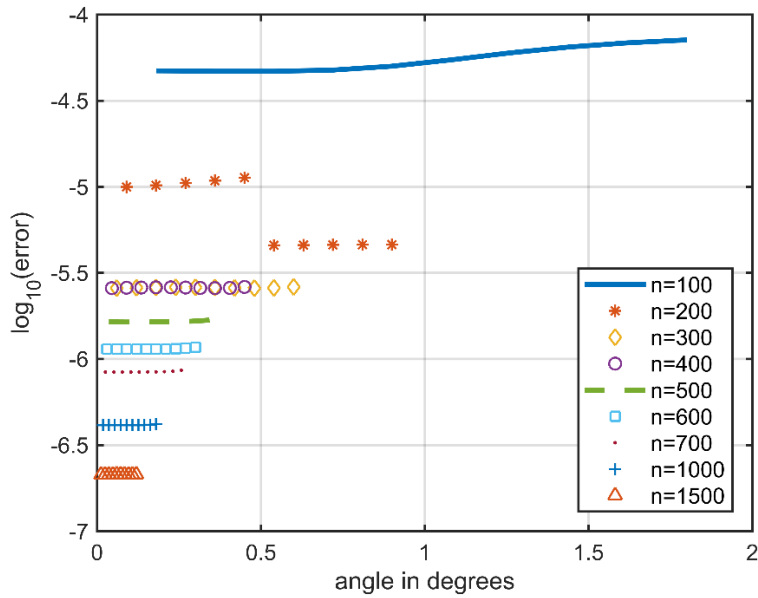


Fig. 20: Error depending on the relative movement between the domains Ω_1 and Ω_2 . The error is shown in the case of domain Ω_2 with radius R_1 .

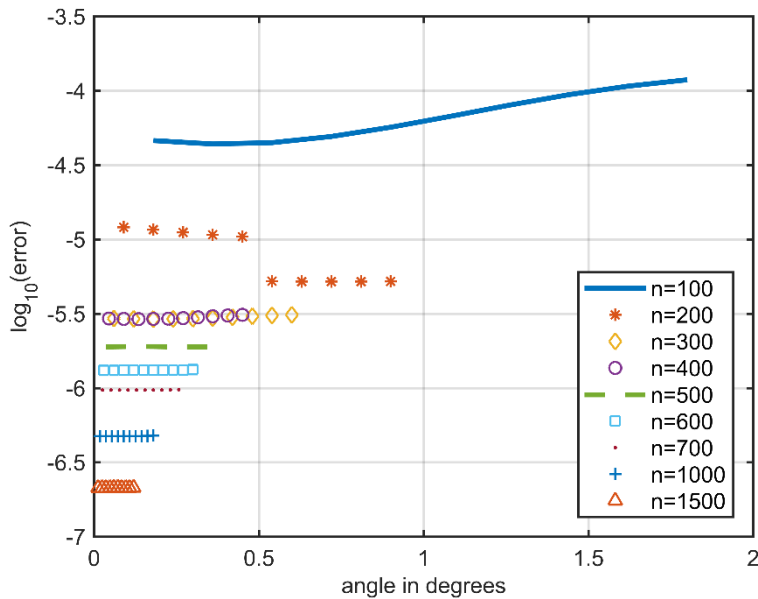


Fig. 21: Error depending on the relative movement between the domains Ω_1 and Ω_2 . The error is shown in the case of domain Ω_1 with radius R_2 .

To conclude this section on error analyses, a brief remark is made about the sparsity of the system matrix of the equation system (69). A comparison of the distribution of the non-zero entries of the system matrices in case of a conforming and a non-conforming mesh for the magneto-static problem (79) - (82) is shown in Fig. 22. For illustrative purposes, the number of finite elements is chosen as $n=400$. Comparing the structure of the matrix in case of the

non-conforming mesh (Fig. 22a) with the structure of the matrix obtained by the conforming mesh case (Fig. 22b), it can be seen that the sparsity and symmetry are very similar in both cases. In case of the non-conforming mesh coupling, the number of non-zeros: $nz=856799$, is slightly larger than in case of the conforming mesh with $nz=808799$. In particular, the number of additional non-zeros (coupling coefficients) is $nz=48000$. The position of these additional coefficients in the overall matrix of the equations system is shown in Fig. 22c.

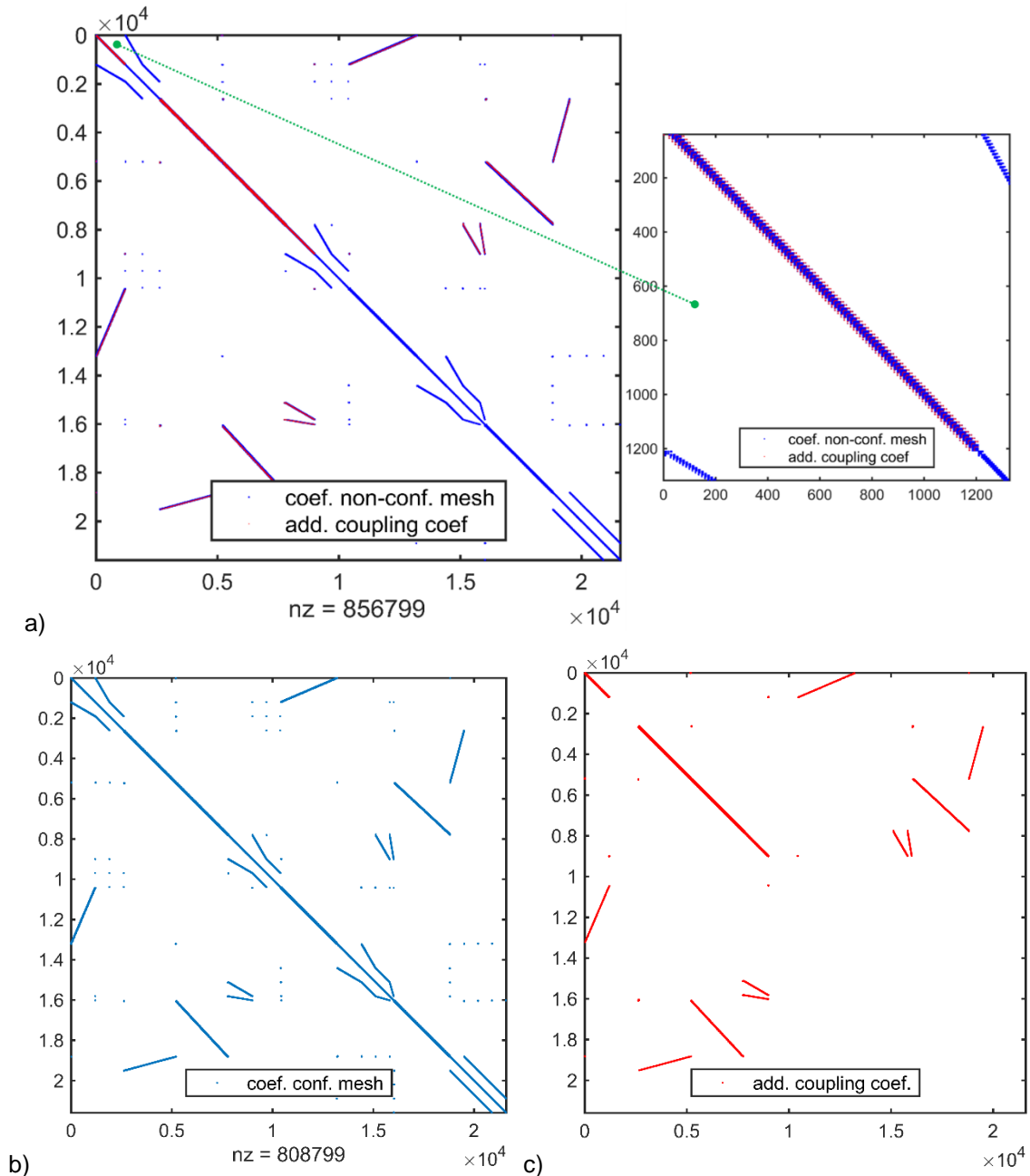


Fig. 22: Comparison of the distribution of the non-zero entries in the system matrix in case of a non-conforming and a conforming mesh. a) System matrix of the non-conforming mesh with a detail view of the main diagonal. b) System matrix in case of a conforming mesh. c) Additional coupling coefficients (non-zeros).

4.4 Periodic boundary condition

The use of (anti-) periodic boundary conditions is useful to reduce the cost of modelling with finite elements, since many electromagnetic field problems are of symmetric, periodical and repetitive structure. The use of (anti-) periodic boundaries is well established and has been systematically introduced e.g. in [53] and [6]. In this section, the (anti-) periodic boundary conditions are investigated in the frame of the non-conforming mesh method for node-based hexahedral elements. The (anti-) periodic boundary condition is validated by solving a magneto-static field problem of simple rotating machine with six poles.

The use of (anti-) periodic boundary conditions is applicable to the non-conforming mesh method without introducing any additional constraints. In Fig. 23, a sketch of the boundary connection conditions is shown for two disjoint domains Ω_1 and Ω_2 with a non-matching mesh along the sliding surface Γ_S . On the left and right boundaries $\Gamma_{a,1}$, $\Gamma_{a,2}$ of each domain, (anti-) periodic boundaries are imposed. Taking these into account, the nodal coupling between the master and slave nodes along the sliding surface splits up into two parts. First, the master-slave coupling can be directly obtained at the surface part Γ_d . Second, the coupling between the slave and master nodes is executed at the complementary surfaces $\Gamma_{c,1}$, $\Gamma_{c,2}$. In other words, the slave nodes located on the surface $\Gamma_{c,1}$, correspond to master nodes located on the surface $\Gamma_{c,2}$. Taking this complementary correspondence and the (anti-) periodic boundary condition into account, the ansatz function (65) for the scalar potential can be rewritten as

$$\begin{aligned} \Phi_n(\mathbf{r}) = & \sum_{l=1}^{L^{(regular)}} \Phi_l^{(regular)} N_l^{(regular)} + \sum_{l=1, l \in \Gamma_d}^{L^{(master)}} \Phi_l^{(master)} \left(N_l^{(master)}(\mathbf{r}) + \sum_{k=1}^{L^{(slave)}} c_{kl} N_k^{(slave)}(\mathbf{r}) \right) + \\ & + \sum_{l=1, l \in \Gamma_c}^{L^{(master)}} \pm \Phi_l^{(master)} \left(N_l^{(master)}(\tilde{\mathbf{r}}) + \sum_{k=1}^{L^{(slave)}} c_{kl} N_k^{(slave)}(\tilde{\mathbf{r}}) \right) \end{aligned} \quad (87)$$

with the transformed, fictitious space coordinates of the slave node $\tilde{\mathbf{r}}$ at the complementary surface, either $\Gamma_{c,1} \rightarrow \Gamma_{c,2}$ or $\Gamma_{c,2} \rightarrow \Gamma_{c,1}$. Note that the (anti-) periodic boundary coupling is considered by the +/- sign of the magnetic scalar potential of the master node appearing in the third term on the right hand side of (87).

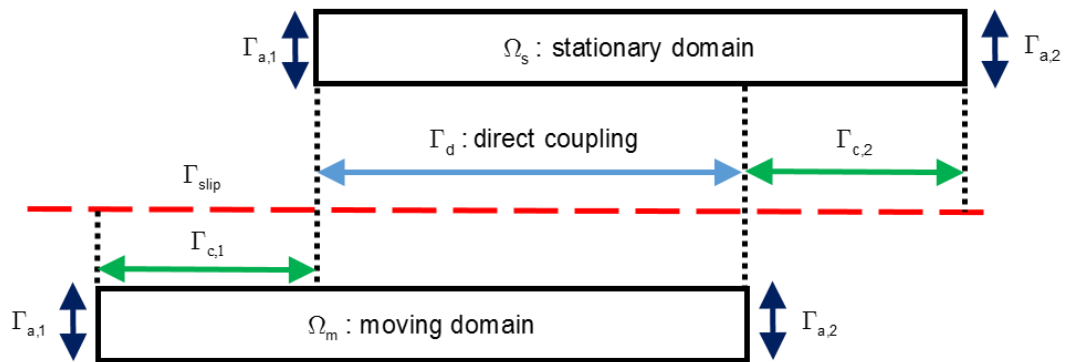


Fig. 23: Illustration of (anti-) periodic boundary conditions in case of moving domains.

The validation of this concept to deal with (anti-) periodic boundary conditions is carried out by solving a magneto-static problem of a simple rotating machine with six poles. Only one-sixth of the machine has to be modelled, with a 60-degree azimuthal periodicity. The problem model with the rotor displaced relatively to the stator by an angle of 20 degrees is shown in Fig. 24a. The excitation of the magnetic field is provided by an impressed, stationary current in the stator winding, whereas the rotor is not excited in this simplified test case. The model with the periodic boundaries and discretised by node-based second order hexahedral elements is shown in Fig. 24b. To compare the result obtained by the non-conforming mesh model, a second model with a conforming mesh is also analysed. The field plots of the magnetic flux density $|\mathbf{B}|$ in the two cases are compared in Fig. 25, and the comparison of some values of the magnetic flux density and the magnetic field intensity $|\mathbf{H}|$ are shown in Fig. 26. These values have been taken at $N_p=360$ equidistant evaluation points along a curved line within the stator domain at radius $R=0.09m$ in an azimuthal range of 60 degrees.

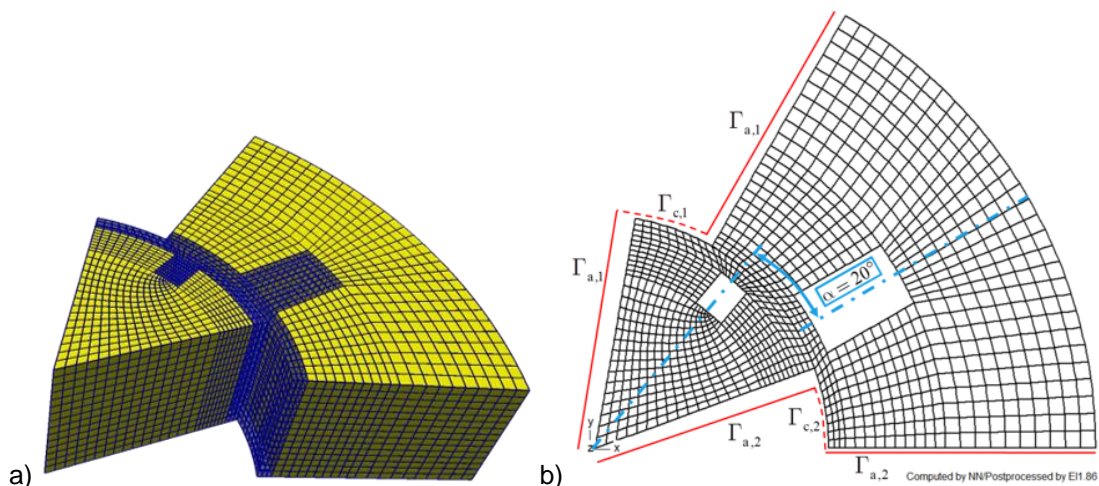


Fig. 24: Problem model of a rotating machine with six poles. a) 3D view of one-sixth of the machine with 60-degree azimuthal periodicity. b) Top view of the problem with (anti-) periodic boundary conditions.

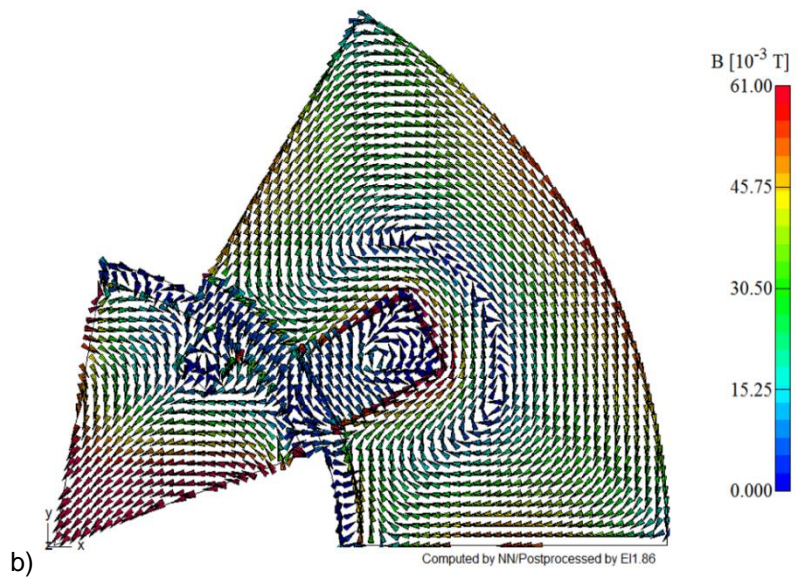
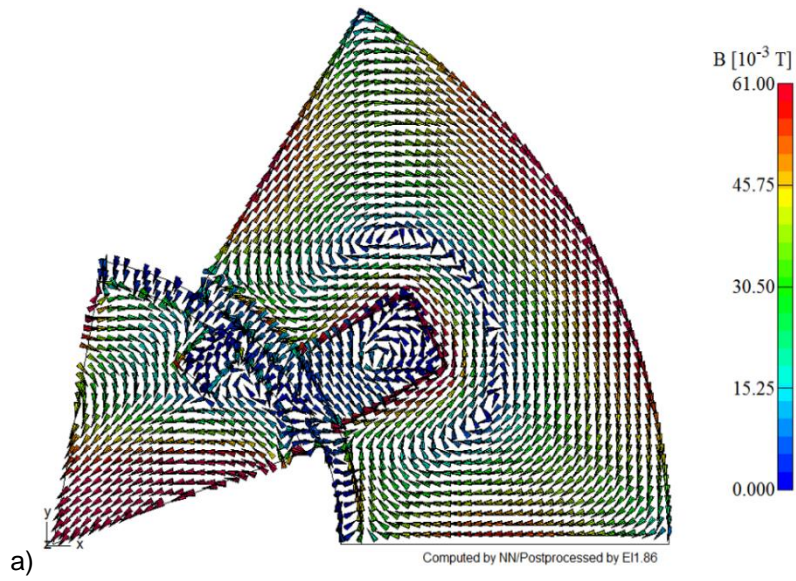


Fig. 25: Comparison of the magnetic flux density $|\mathbf{B}|$. a) Non-conforming mesh b) Conforming mesh

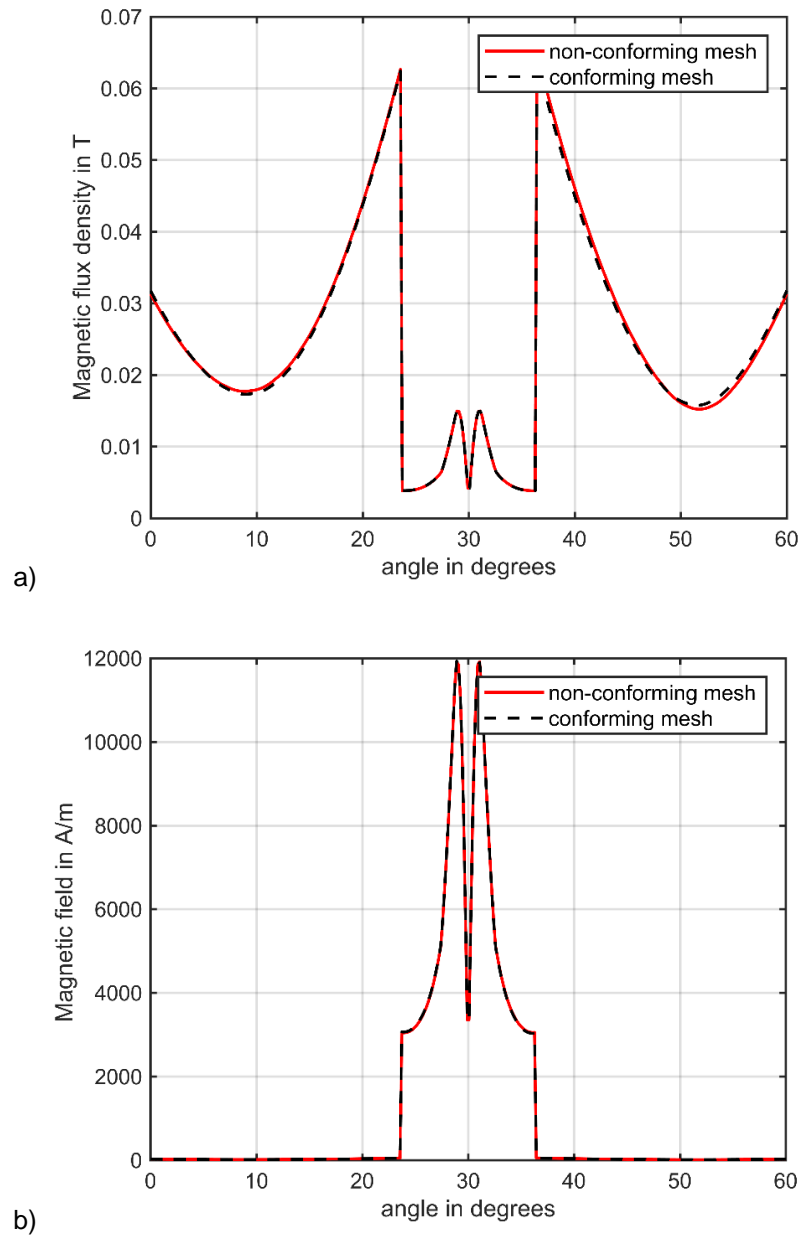


Fig. 26: Comparison of numerical values calculated along a curved line with radius $R=0.09m$ and azimuthal range of 60 degrees. a) Magnetic flux density $|\mathbf{B}|$ b) Magnetic field intensity $|\mathbf{H}|$.

The magnetic field intensity $|\mathbf{H}|$ determined by the non-conforming mesh model is in a good agreement with the magnetic field obtained by the conforming mesh model (see Fig. 26b). As the numerical values of the magnetic flux density $|\mathbf{B}|$ show (see Fig. 26a), there is also a good agreement between the result of the conforming mesh and non-conforming mesh.

5 Taking account of motion

5.1 Problem definition

The relative movement between two domains with at least one of them including a source that excites a magnetic field leads to eddy currents induced by motion if conducting regions are present. This problem has been treated in the literature for formulations utilizing a magnetic vector potential e.g. in [48] - [50]. The eddy currents are due to the time-variation of the magnetic field, either through a time varying imposed current density \mathbf{J}_0 , or by the movement of the source generating the magnetic field, or by the movement of the conductor in the presence of a magnetic field. The issue of motional eddy currents can be described either by a stationary framework utilizing the Minkowski transformation, or by taking account of the relative movement between a stationary and moving domains.

5.1.1 Motional eddy currents – stationary framework

In a stationary framework, the motion induction is taken into account by adding the velocity term $\mathbf{v} \times \mathbf{B}$ to the electric field intensity [51] giving rise to the currents generating the magnetic field where \mathbf{v} is the velocity and \mathbf{B} the magnetic flux density. The so-called Minkowski transformation leads to a single steady state solution, assuming that the velocity is constant [49]. In addition to the restriction that only moving conductor volumes with invariant cross section at right angles to the direction of motion can be considered, the resulting finite element system matrix is asymmetric and often ill-conditioned in case of coarse meshes [49]. Despite these disadvantages, using this stationary framework as reference method in the following section 5.2 dedicated to accuracy analyses is feasible. The reason is that this formulation can be modelled by conforming meshes.

Briefly, the method uses the magnetic vector potential \mathbf{A} , satisfying $\mathbf{B}=\text{curl}\mathbf{A}$, and the scalar electric potential V giving rise to the electric field $\mathbf{E}=-\text{grad}V-\partial\mathbf{A}/\partial t$. Therefore, Ampere's law (see section 3.2.2) including the velocity term can be written as:

$$\text{curl}\frac{1}{\mu}\text{curl}\mathbf{A}=-\sigma\frac{\partial\mathbf{A}}{\partial t}-\sigma\text{grad}V+\sigma\mathbf{v}\times\text{curl}\mathbf{A}, \quad (88)$$

with the electric conductivity σ and the relative permeability μ . Note that the continuity equation $\text{div}\mathbf{J}=0$ is implied by (88), but it is included in the boundary value problem in order to have two differential equations for the two unknown potentials:

$$\text{div}\left(\sigma\left(\frac{\partial\mathbf{A}}{\partial t}-\mathbf{v}\times\text{curl}\mathbf{A}+\text{grad}V\right)\right)=0. \quad (89)$$

5.1.2 Motional eddy currents – moving framework

A more general approach to take account of the effects of the electro-motive force (emf) due to motion is to consider the relative movement between a stationary and a moving domain. Following the approach of [50] and [52], the moving framework can be defined as described below.

Consider a stationary, global coordinate system S and a point located at $\mathbf{r}(t)$ within a conductor moving with the velocity \mathbf{v} and discretised with the aid of finite elements. Hence, Faraday's law can be written in this system with the velocity term as

$$\text{curl}\mathbf{E}=-\frac{\partial\mathbf{B}(t,\mathbf{r}(t))}{\partial t}+\text{curl}(\mathbf{v}\times\mathbf{B}(t,\mathbf{r}(t))), \quad (90)$$

where the flux density \mathbf{B} is dependent on time t as well as the space coordinate $\mathbf{r}(t)$. If the conductor is moved at a velocity \mathbf{v} for a given time interval Δt , each finite element of the conductor is exposed to a magnetic field $\mathbf{B}'(\ell',\mathbf{r}')$ occurring at $\ell'=\ell+\Delta\ell$ in time and at $\mathbf{r}'=\mathbf{r}(t)+\mathbf{v}\Delta t$ in space. An illustration of this conductor movement is shown in Fig. 27.

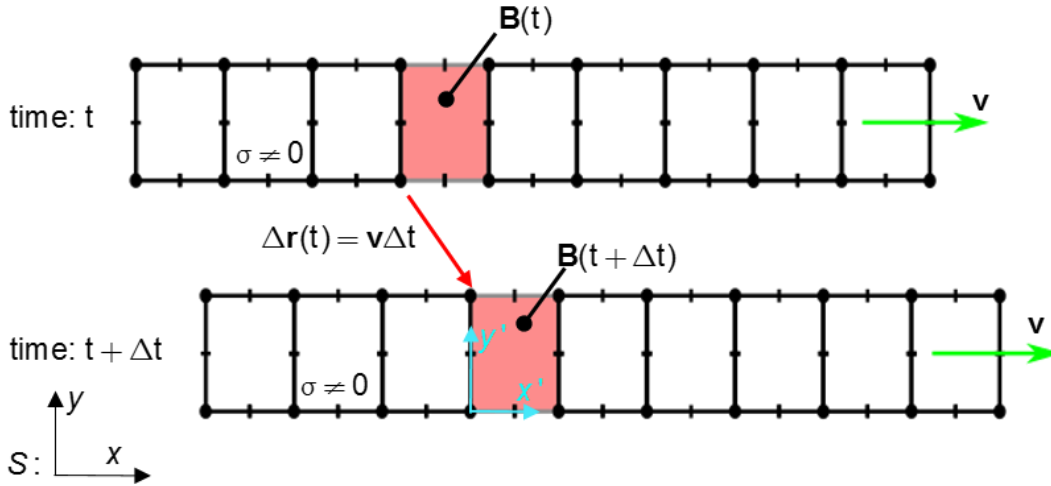


Fig. 27: Conductor moving in the global coordinate system S at a velocity \mathbf{v} for a certain time Δt . The finite elements of the conductor are exposed to a change of the magnetic flux density.

Since the finite elements belong to their local coordinate system S' which moves with the velocity \mathbf{v} , each finite element observes a change of the magnetic flux density $\Delta \mathbf{B} = \mathbf{B} - \mathbf{B}'$. Therefore, the velocity term $\mathbf{v} \times \mathbf{B}$ can be omitted in S' and it is sufficient to approximate Faraday's law (90) by the difference of the magnetic flux density at time instants t and $t + \Delta t$.

$$\text{curl} \mathbf{E} \approx \frac{\mathbf{B} - \mathbf{B}'}{\Delta t} = \frac{\mathbf{B}(t) - \mathbf{B}(t + \Delta t)}{\Delta t} \quad (91)$$

5.1.3 \mathbf{T}, Φ - Φ , formulation for motional eddy currents

In this work the \mathbf{T}, Φ - Φ formulation for eddy current problems (see section 3.7.2) will be combined with the non-conforming mesh method to consider the relative movement between a stationary and a moving domain. In this case, the non-conforming mesh method as introduced in the sections 4.1 and 4.2 can be used without change if the sliding interface is located in the non-conducting domain with the magnetic field described by the scalar potential Φ .

The governing equations of the eddy current problem can be found by substituting the potentials defined in (41) and (55) into Maxwell's equations (1)-(3). Hence, the differential equation corresponding to Faraday's law in the conducting domain Ω_c is

$$\text{curl}(\rho \text{curl} \mathbf{T}) + \frac{\partial}{\partial t}(\mu \mathbf{T}) - \frac{\partial}{\partial t}(\mu \text{grad} \Phi) = -\text{curl}(\rho \text{curl}(\mathbf{T}_0)) - \frac{\partial}{\partial t}(\mu \mathbf{T}_0) \text{ in } \Omega_c. \quad (92)$$

By the solenoidality of the magnetic flux density ($\text{div}\mathbf{B}=0$), an additional differential equation in the domain $\Omega_c \cup \Omega_n$ (i.e. both in the conducting and non-conducting domains) is obtained as

$$\text{div}(\mu\mathbf{T} - \text{grad}\Phi) = -\text{div}(\mu\mathbf{T}_0) \text{ in } \Omega_c \cup \Omega_n . \quad (93)$$

Having discretized the problem, the current vector potential \mathbf{T} can be approximated with the aid of the edge basis functions \mathbf{N}_k (see section 3.4) and the magnetic scalar potential Φ by the node-based polynomial basis functions N_k (see section 3.4). Thus, the ansatz functions for the potentials are

$$\mathbf{T} \approx \mathbf{T}_n = \sum_{k=1}^{n_{edge}} t_k \mathbf{N}_k , \quad (94)$$

$$\Phi \approx \Phi_n = \sum_{k=1}^{n_{node}} \varphi_k N_k \quad (95)$$

where t_k represent the line integrals of \mathbf{T}_n along the element edges, and φ_k the nodal values of the potential Φ_n .

Applying Galerkin techniques to the differential equations in (92) and (93), two sets of equations are obtained

$$\begin{aligned} & \int_{\Omega_c} \text{curl}\mathbf{N}_i \cdot \rho \text{curl}\mathbf{T}_n d\Omega + \int_{\Omega_c} \mathbf{N}_i \left[\frac{\partial}{\partial t}(\mu\mathbf{T}_n) - \frac{\partial}{\partial t}(\mu \text{grad}\Phi_n) \right] d\Omega = \\ & - \int_{\Omega_c} \text{curl}\mathbf{N}_i \cdot \rho \text{curl}\mathbf{T}_0 d\Omega - \int_{\Omega_c} \mathbf{N}_i \frac{\partial}{\partial t}(\mu\mathbf{T}_0) d\Omega \quad (i = 1, 2, \dots, n_{edge}) \end{aligned} \quad (96)$$

$$\begin{aligned} & \underbrace{\int_{\Omega_c + \Omega_n} \text{grad}N_i \frac{\partial}{\partial t} \mu \text{grad}\Phi_n d\Omega}_{\text{for } \Omega_n: \text{Int. 1}} - \int_{\Omega_c} \text{grad}N_i \frac{\partial}{\partial t}(\mu\mathbf{T}_n) d\Omega = \\ & \underbrace{\int_{\Omega_c + \Omega_n} \text{grad}N_i \frac{\partial}{\partial t}(\mu\mathbf{T}_0) d\Omega}_{\text{for } \Omega_n: \text{Int. 2}} + \underbrace{\int_{\Gamma_B} N_i \frac{\partial b}{\partial t} d\Gamma}_{\text{Int. 3}} \quad (i = 1, 2, \dots, n_{nodes}). \end{aligned} \quad (97)$$

Focusing on the equation terms which are valid for the non-conducting domain Ω_n in (97), the non-conforming mesh method can be introduced as already discussed in section 0. Using the ansatz function (65) for the magnetic scalar potential, the terms in (97) specific for the domain Ω_n can be rewritten as:

Integral Int. 1:

$$\begin{aligned}
 & \sum_{k=1}^{L^{(regular)}} \int_{\Omega_n} \text{grad} N_i^{(regular)} \frac{\partial}{\partial t} \left(\mu \varphi_k^{(regular)} \text{grad} N_k^{(regular)} \right) d\Omega + \\
 & + \sum_{k=1}^{L^{(master)}} \int_{\Omega_n} \text{grad} N_i^{(master)} \frac{\partial}{\partial t} \left(\mu \varphi_k^{(master)} \Psi_k \right) d\Omega + \\
 & + \sum_{k=1}^{L^{(regular)}} \int_{\Omega_n} \Psi_i \frac{\partial}{\partial t} \left(\mu \varphi_k^{(regular)} \text{grad} N_k^{(regular)} \right) d\Omega + \sum_{k=1}^{L^{(master)}} \int_{\Omega_n} \Psi_i \frac{\partial}{\partial t} \left(\mu \varphi_k^{(master)} \Psi_k \right) d\Omega
 \end{aligned} \quad (98)$$

Integral Int. 2:

$$\int_{\Omega_n} \text{grad} N_i^{(regular)} \frac{\partial}{\partial t} (\mu \mathbf{T}_0) d\Omega + \int_{\Omega_n} \Psi_i \frac{\partial}{\partial t} (\mu \mathbf{T}_0) d\Omega . \quad (99)$$

Integral Int. 3:

$$\int_{\Gamma_B} N_i^{(regular)} \frac{\partial b}{\partial t} d\Gamma + \int_{\Gamma_B} \left(N_i^{(master)} + \sum_{k=1}^{L^{(slave)}} c_{ki} N_k^{(slave)} \right) \frac{\partial b}{\partial t} d\Gamma . \quad (100)$$

Again, the term Ψ_k used in the integral expressions (98) - (100) is defined as

$$\Psi_k = \text{grad} N_k^{(master)} + \sum_{l=1}^{L^{(slave)}} c_{kl} \text{grad} N_l^{(slave)} . \quad (101)$$

Finally, the following equation system is obtained:

$$\begin{aligned}
 & \begin{bmatrix} \mathbf{A}_{RR} & \mathbf{A}_{RM} + \mathbf{A}_{RS} \mathbf{C} \\ \mathbf{C}^T \mathbf{A}_{RS} + \mathbf{A}_{RM}^T & \mathbf{A}_{MM} + \mathbf{C}^T \mathbf{A}_{SS} \mathbf{C} \end{bmatrix} \begin{pmatrix} \mathbf{x}_R \\ \mathbf{x}_M \end{pmatrix} + \\
 & + \begin{bmatrix} \mathbf{K}_{RR} & \mathbf{K}_{RM} + \mathbf{K}_{RS} \mathbf{C} \\ \mathbf{C}^T \mathbf{K}_{RS} + \mathbf{K}_{RM}^T & \mathbf{K}_{MM} + \mathbf{C}^T \mathbf{K}_{SS} \mathbf{C} \end{bmatrix} \begin{pmatrix} \dot{\mathbf{x}}_R \\ \dot{\mathbf{x}}_M \end{pmatrix} = \\
 & = \begin{pmatrix} \mathbf{b}(t)_R \\ \mathbf{b}(t)_{A,M} + \mathbf{C}^T \mathbf{b}(t)_{K,RS} \end{pmatrix} + \begin{pmatrix} \dot{\mathbf{b}}(t)_{K,R} \\ \dot{\mathbf{b}}(t)_{K,M} + \mathbf{C}^T \dot{\mathbf{b}}(t)_{K,RS} \end{pmatrix}
 \end{aligned} \quad (102)$$

where \mathbf{C} denotes the coupling matrix including the coupling factors c_{kl} of the master nodes. The stiffness matrix is denoted by \mathbf{A}_{ij} , and \mathbf{K}_{ij} denotes the mass matrix where the subscripts R , M and S stand for the regular, master and slave degrees of freedom. After time-discretization, the equation system in (102) can be solved iteratively by well-established techniques like the conjugate gradient (CG) method, since the obtained matrices are sparse, symmetric and positive definite.

5.2 Accuracy analysis

In this section two problem types, planar and cylindrical structures are investigated and the results obtained are discussed. Both problem types are of academic nature to allow comparisons to reference methods and to analyse the application of the non-conforming mesh method to motional eddy current problems. The first problem takes account of planar motion with two straight conductors moved above an iron plate. In the second example, a cylindrical coil is rotated within a copper shell.

Due to the simplicity of both examples, two kinds of reference solutions involving conforming meshes can be used as benchmarks. Either the transient behaviour or the steady state solution after the transients have faded will be compared to these. In the latter case, the Minkowski transformation described in subsection 5.1.1 is used to obtain the reference solution. The time transient behaviour is verified by comparing it to results obtained by solving the problems with the overall finite element mesh being stationary and conforming and the sources are moved only. This is possible, since, being represented by the source current vector potential \mathbf{T}_0 on the right hand side of (96) and (97), these need not be modelled by the finite element mesh. It is sufficient to update \mathbf{T}_0 at each time step with the motion of the sources taken into account. In the following, this method is referred to as transient reference method. Note that this method is only feasible if the sources (coil, conductors, etc.) are surrounded by air and no magnetic medium like e.g. the iron core of a coil is in movement.

The performance of the non-conforming meshing method is analysed by varying the mesh density along the sliding surface Γ_S or the size of the time step. The simulations are first carried out both for planar and rotational movement with equal mesh densities in the moving and stationary domains along the sliding surface. In the case of rotational movement, an additional experiment is performed to consider two different mesh densities in the moving and stationary domains along the sliding surface.

5.2.1 Planar problem – plane motion

The planar problem shown in Fig. 28 consists of a thin iron plate located parallel to the xy -plane and two straight conductors above this plate. The geometrical dimensions of the problem are shown in Fig. 28. The linear material properties of the iron plate are chosen as $\sigma_{Fe}=0.45 \cdot 10^7 Sm^{-1}$ for the conductivity and μ_r for the relative permeability. The sliding surface Γ_S is placed in the middle of the air gap with the surrounding air containing the two conductors defined as master domain Ω_{mov} and the region including the iron plate is selected as slave domain Ω_{stat} . The movement of the master domain and the two conductors with a constant velocity contradicts the boundary conditions at the boundaries parallel to the xz -plane. In order to minimize the influence of this boundary effect, the problem domain including the plate is sufficiently enlarged in the y -direction. The field quantities are evaluated in $N_p=1000$ equidistant points along a straight line. This line runs in the y -direction in the centre of the iron plate with a length of $l=1m$ at a depth of $z_1=1mm$, below the top of the plate.

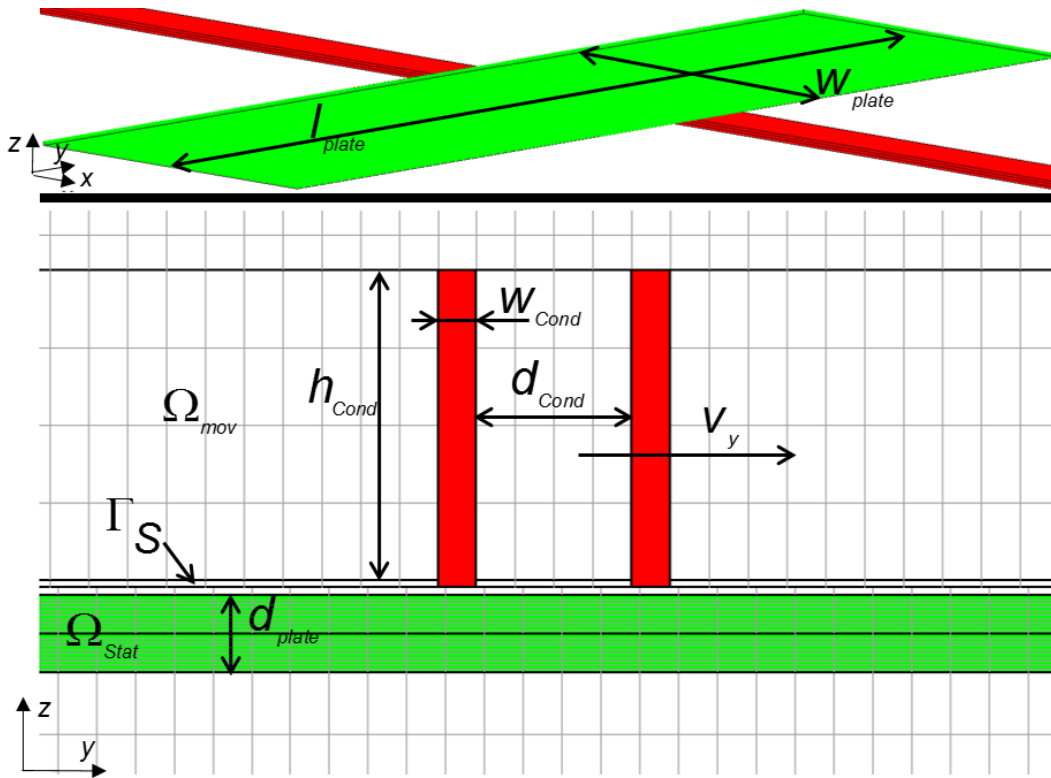


Fig. 28: Planar problem model to consider motion induced eddy currents. The dimensions of the iron plate are defined as $l_{plate}=3m$, $w_{plate}=1m$ and $d_{plate}=0.01m$. The cross section of the conductors is defined by $w_{cond}=5mm$ and $h_{cond}=41mm$. The two conductors are displaced to each other by $d_{cond}=20mm$ and the air gap between the conductors and iron plate is set to $d_A=1mm$.

The finite element mesh is generated by subdividing the whole domain into n_E equidistant second order hexahedral elements in the y -direction. As the example is geometrically invariant in x -direction, only one layer of elements parallel to the yz -plane is needed. The mesh density along the sliding surface Γ_S is defined as

$$\delta_{n_E} = \frac{n_E}{l_{plate}} \quad (103)$$

where the unit of the length l_{plate} is taken in meters. Note that this density is the same for both the master and slave domains.

In case of the time transient simulations, the magnetic field is excited by the impressed current density of the conductors $\mathbf{J}(t)$ assumed to be a step function with a ramp as shown in Fig. 29 and can be written as

$$\mathbf{J}(t) = \begin{cases} \mathbf{J}_0(t-t_1)/(t_2-t_1), & \text{for } t_1 \leq t \leq t_2 \\ \mathbf{J}_0, & t_2 < t \leq T \end{cases}, \quad (104)$$

with the steady state value $\mathbf{J}_0=0.625 \cdot 10^7 \text{ Am}^{-2}$, $t_1=0.0\text{ms}$, $t_2=16.0\text{ms}$ and $T=48\text{ms}$. This time interval T corresponds to an overall displacement of 240mm in the y -direction, as the y -component of the velocity is chosen to be $v_y=5\text{ms}^{-1}$. In case of the stationary simulation including the velocity term, the impressed current density is set to the steady state value $\mathbf{J}_0=0.625 \cdot 10^7 \text{ Am}^{-2}$.

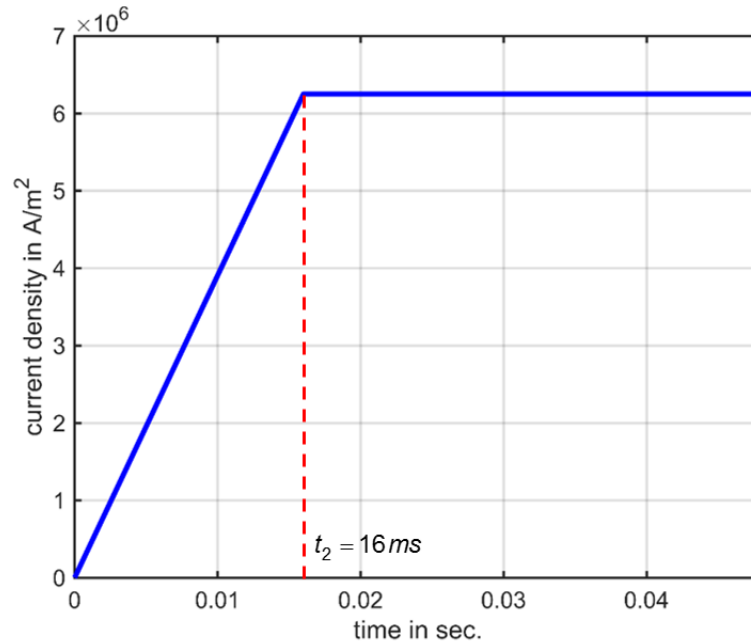


Fig. 29 Impressed current density $\mathbf{J}(t)$ is assumed to be a step function with ramp.

As mentioned in the introduction of this section, two types of analyses have been carried out. First, the time step size Δt has been varied from $\Delta t=0.5ms$ up to $\Delta t=1.5ms$ corresponding to displacements of $\Delta d=0.25mm$ up to $\Delta d=7.5mm$ of the moving domain Ω_{mov} relative to the stationary domain Ω_{stat} . Second, the mesh density δ_{n_E} is increased using the values $n_E \in \{600, 1200, 3000\}$ finite elements along the sliding surface, whereas the time step Δt is kept constant. The numbers n_E of elements correspond to element widths of $w_{EL}=5.0, 2.5$ and $1.0mm$.

The curves in Fig. 30 and Fig. 31 have been obtained by calculating the mean value of the modulus of the current density $|\mathbf{J}_i|$ at the points $i=1, 2, \dots, N_p=1000$ for each time step

$$\mathbf{J}_{mean}(t) = \frac{1}{N_p} \sum_{i=1}^{N_p} |\mathbf{J}_i|, \text{ with } 0 \leq t \leq 48ms. \quad (105)$$

The evaluation of the mean value at each time step allows a simple characterization of the transient behaviour of the eddy current density \mathbf{J} in the iron plate (see Fig. 30). Oscillations of the solution at steady state obtained at approximately $t=25.0ms$ occur for each time step. These oscillations are expected to be due to the mesh being too coarse with $n_E=600$ elements. In the case of a small time step, oscillations of the solution are present but not as intense as shown by the solutions with an increased time step. In addition to these oscillations, the steady state solution decreases on average if the time step size increases.

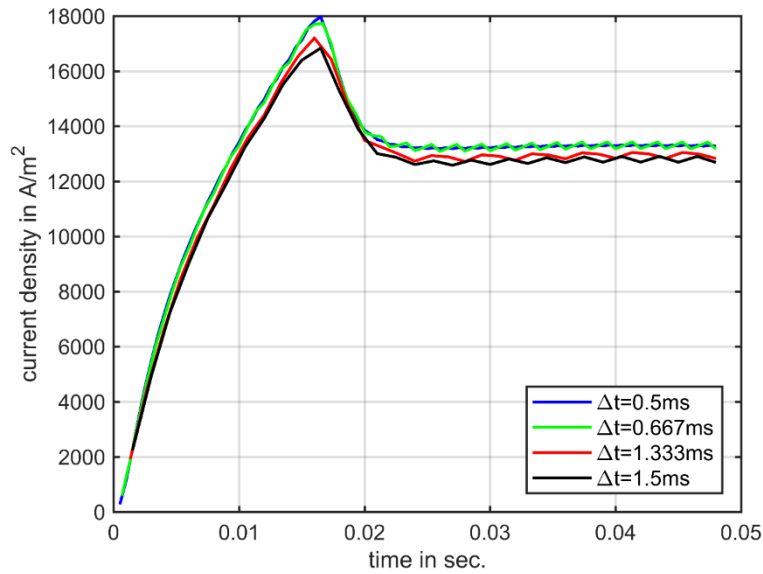


Fig. 30: Comparison of the current density in case of a coarse mesh with $n_E=600$ elements along the sliding surface.

The plots of the current density $|\mathbf{J}|$ shown in Fig. 31 correspond to the case of $n_E=3000$ elements along the sliding surface. The solutions obtained show the same overall transient behaviour as those plotted in Fig. 30 and compare quite well with the transient reference solution. In particular, the solutions at steady state are in a very good agreement with the stationary solution, provided the time steps are chosen sufficiently small. However, accuracy

is lost if the time step size is increased, similarly to the case of the coarser mesh in Fig. 21. As expected, the oscillations of the mean value of $|\mathbf{J}|$ seen in Fig. 30 disappear due to the increase of the number of elements. It is safe to conclude that the decrease of the element size will improve stability and, indeed, overall accuracy. These results are in agreement with the results obtained at the error analysis in section 4.3 where the error also decreases with an increased number of elements.

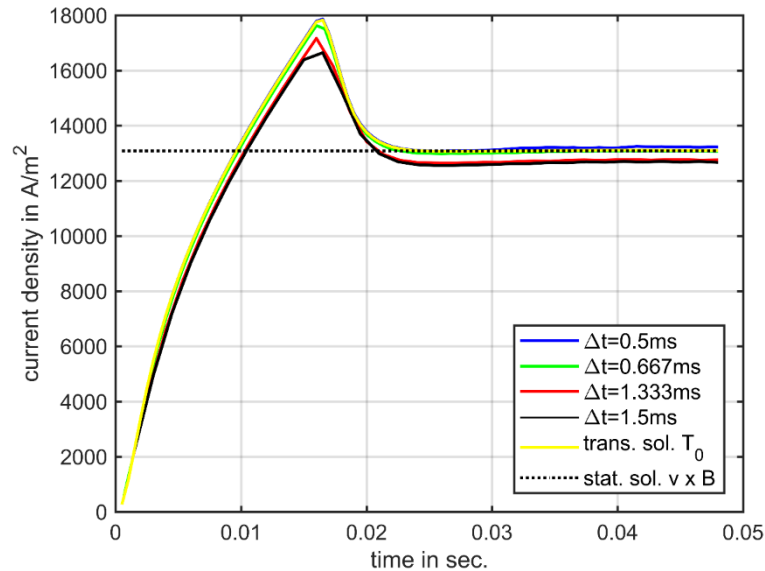


Fig. 31: Comparison of the current density in case of a fine mesh with $n_E=3000$ elements along the sliding surface.

To underline this statement, the values of the current density $|\mathbf{J}|$ and of the magnetic flux density $|\mathbf{B}|$ at steady state are shown in Fig. 32 and Fig. 33. In addition to two solutions with different time steps using a non-conforming mesh, the reference solutions, stationary and transient, have also been plotted. In case of the time transient solutions, the field values following the last time step at $t=48ms$ have been evaluated. The distribution of the current density $|\mathbf{J}|$ in Fig. 32 is almost identical for each solution. Only the peak values of the transient results, both the reference and the best solution obtained by the non-conforming mesh method, are slightly less than the value yielded by the stationary reference solution at position $y=1.408m$. The transient reference solution and the solution obtained by the non-conforming mesh method with $\Delta t=0.5ms$ are in a very good agreement, but the peak value at $y=1.408m$ is considerably lower in case of $\Delta t=1.5ms$. Comparing the magnetic flux density $|\mathbf{B}|$ in Fig. 33, the same observations as for the current density can be made.

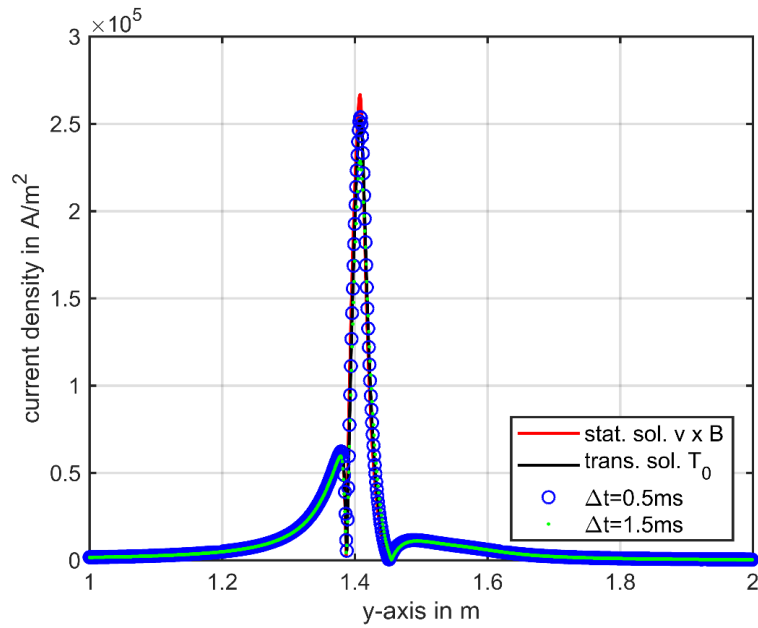


Fig. 32: Comparison of the current density in case of $n_E=3000$ elements along the sliding surface and at last time step $t=48ms$.

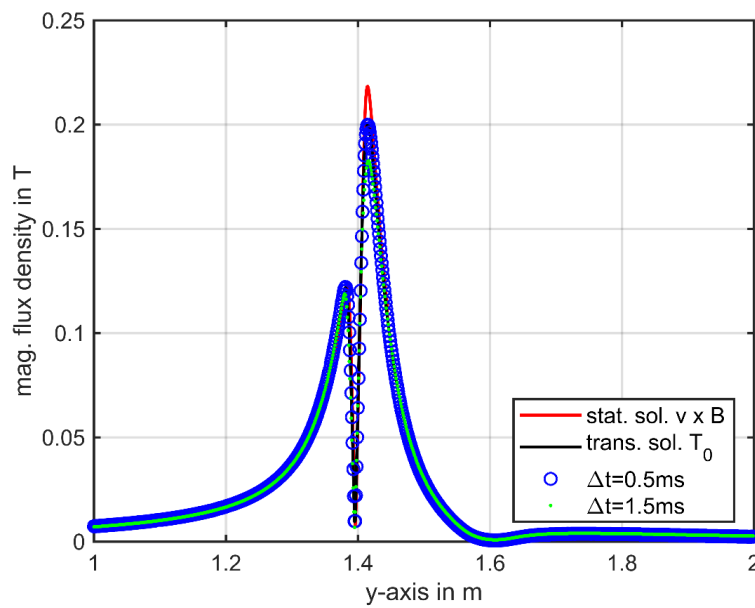


Fig. 33: Comparison of the magnetic flux density in case of $n_E=3000$ elements along the sliding surface and at last time step $t=48ms$.

To conclude the presentation of the results for this planar problem, the field plots of the current density $|\mathbf{J}|$ and magnetic flux density $|\mathbf{B}|$ are compared for the stationary reference solution (Minkowski transformation) and the steady state solution following the last time step of the non-conforming mesh method. The comparisons are shown in Fig. 34 and Fig. 35 where it can be seen that the fields are in a good agreement.

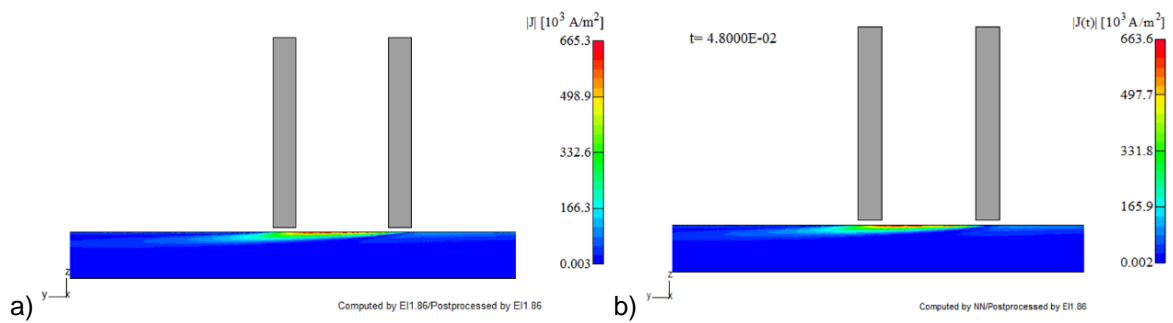


Fig. 34: Field plot of the induced eddy current in the iron plate. a) Current density in case of the stationary solution b) Current density in case of the transient solution with a non-conforming mesh along the sliding surface following the last time step at $t=48ms$.

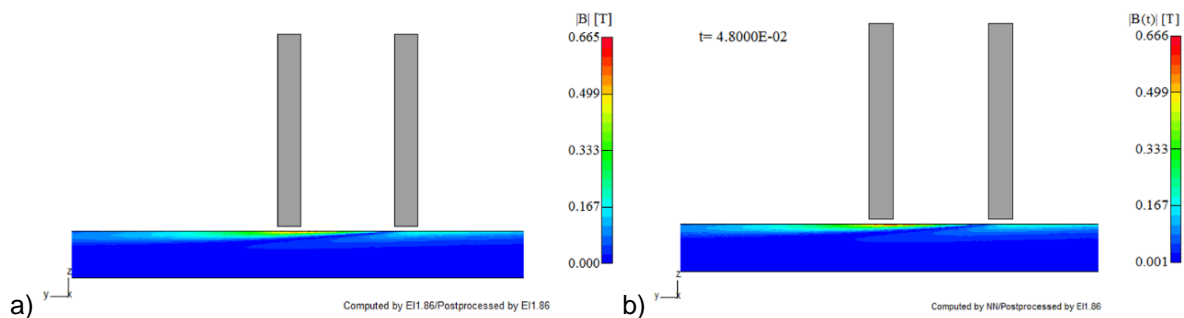


Fig. 35: Field plot of the magnetic flux density in the iron plate. a) Magnetic flux density in case of the stationary solution b) Magnetic flux density in case of the transient solution with a non-conforming mesh along the sliding surface following the last time step at $t=48ms$.

5.2.2 Cylindrical problem – rotational motion

In this section, the cylindrical problem shown in Fig. 36 is investigated using two different finite element mesh topologies. First, the density of finite element mesh along the sliding surface Γ_S is the same for the stationary and moving domains Ω_{stat} and Ω_{mov} (see section 5.2.2.1). In the second case, the mesh density is different in the two domains Ω_{stat} and Ω_{mov} (see section 5.2.2.2).

The problem consists of a cylindrical shell made of copper in the stationary problem domain Ω_{stat} with a cylindrical coil placed in the centre of a cylinder constituting the moving domain Ω_{mov} . The axes of the coil and of the shell are perpendicular to each other. In addition, there is a symmetry plane perpendicular to the axis of the shell. The dimensions of the problem are shown in Fig. 36 and summarized in Tab. 7.

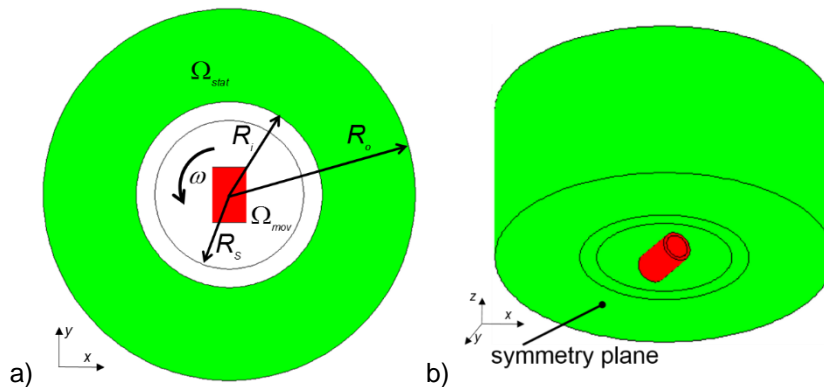


Fig. 36: Model of a problem consisting of a copper shell with a cylindrical coil settled in the centre of the annulus. a) Top view with dimensions b) 3D view with symmetry plane at the bottom.

Copper shell		Cylindrical coil	
outer radius	$R_o=10mm$	outer radius	$R_0^{coil} = 0.9mm$
inner radius	$R_i=5mm$	inner radius	$R_i^{coil} = 0.7mm$
height of the shell	$h_1=10mm$	height of the coil	$h_2=3mm$
radius sliding surface	$R_s=4mm$		

Tab. 7 Dimensions of the cylindrical problem.

The conductivity of the copper shell is $\sigma_{Cu}=5.7 \cdot 10^7 Sm^{-1}$ and the relative permeability is $\mu_r \approx 1$. In both problem models, the impressed current density $\mathbf{J}(t)$ is, again, a step function with a ramp, the steady state value being $J_0=0.1 \cdot 10^7 Am^{-2}$:

$$\mathbf{J}(t) = \begin{cases} \mathbf{J}_0(t - t_1) / (t_2 - t_1), & \text{for } t_1 \leq t \leq t_2 \\ \mathbf{J}_0, & t_2 < t \leq T \end{cases}, \quad (106)$$

with $t_1=0.0ms$, $t_2=16.0ms$ and $T=50.0255ms$. This time interval T corresponds to an azimuthal rotation of 180 degrees, as the constant angular frequency is chosen to be $\omega = 62.8s^{-1}$.

The finite element mesh is generated for both problem models by dividing the structure equidistantly into n_{EL} intervals along the circumference of the sliding interface Γ_S . Hence, the mesh density is defined as

$$\delta_{n_{EL}} = \frac{n_{EL}}{2\pi R_S}. \quad (107)$$

In the following two subsections, the evaluation of the field quantities has been done along a circular line with radius $R_1=5.5mm$ located in the symmetry plane of the copper shell. These numerical values are taken at $N_p=1000$ equidistant points along the circular line. Again, the time transient behaviour is characterized by evaluating the mean values similarly to (105), at each time step in the time interval $0 < t < T$.

5.2.2.1 Copper shell I: equal mesh density

In this first experiment, the mesh density along the sliding surface is chosen to be equal for the moving and stationary domains. Similar to the simulations investigated in section 5.2.1, the size of the time step Δt is first varied with the mesh density kept constant. In addition to this, the mesh density is then varied with the time step size held constant. In Fig. 37, an example of the mesh topology with equal mesh density in the two domains is shown. Similar to the analysis of the planar motion, the results of the non-conforming mesh technique are compared to the solutions obtained by the transient reference method and to the stationary solution using the velocity term. The time steps are varied from $\Delta t=0.278ms$ up to $\Delta t=4.17ms$ and the mesh density values $\delta_{n_{EL}}$ correspond to $n_{EL} \in \{40, 80, 120\}$. The time steps chosen correspond to a relative azimuthal displacement between the domains Ω_{stat} and Ω_{mov} from $\Delta\varphi=1$ degrees up to $\Delta\varphi=15$ degrees.

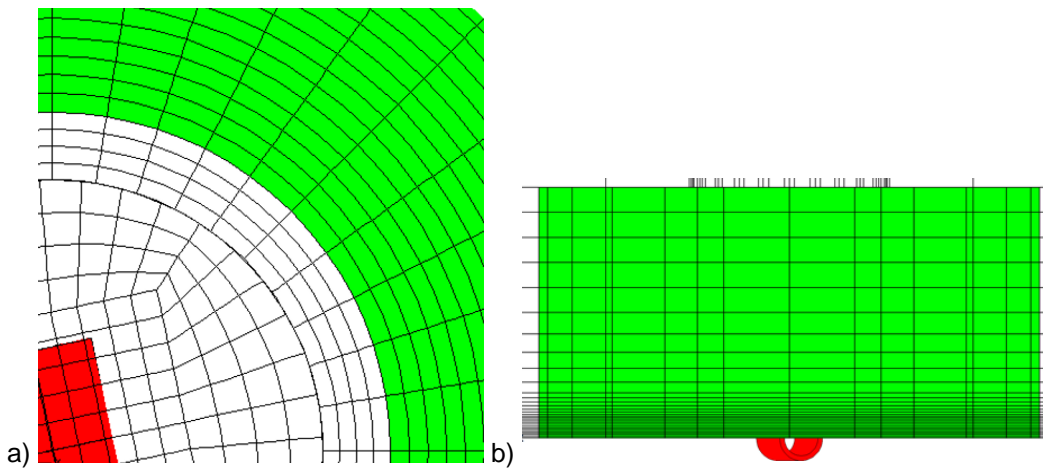


Fig. 37: Mesh topology with equal mesh density in both domains, stationary and moving.
a) Top view of the mesh b) Front view of the mesh along the z-axis.

Fig. 38 compares the transient behaviour of the current density $|\mathbf{J}|$ for different time steps and for the number of elements $n_{EL}=40$. It can be observed that the solutions are in a good agreement with the reference solutions (transient reference method and stationary solution). The time steps $\Delta t=2.084ms$ and $\Delta t=2.501ms$ are obviously too large to capture the decay of the transient solution properly. However, the steady state solutions obtained by these time steps are almost equal to the other solutions and no oscillations appear at steady state. Note that the time step $\Delta t=2.501ms$ corresponds to an azimuthal displacement of 9 degrees which is equal to the angle of each element. In this particular case, a so called locked step analysis, with the mesh being conformal at each time step has been performed. The oscillations in the transient part as well as in the steady state part at lower time steps are expected to be due to a too large element size. The oscillations in case of $\Delta t=0.417ms$ (relative displacement of $\Delta\varphi=1.5$ degrees) are smoother, than in case of $\Delta t=0.278ms$ with corresponding relative displacement of $\Delta\varphi=1.0$ degrees. Comparing the solutions with the same time step but with increased number of elements $n_{EL}=80$, a similar behaviour can be observed (see Fig. 39). Indeed, the accuracy and smoothness of the solutions has increased in general. In the

particular case of $\Delta t=0.417ms$, the oscillations have almost vanished. If the number of elements is further increased to $n_{EL}=120$, the oscillations of the solution are decreased in the case of $\Delta t=0.278ms$, too. Therefore, the ratio χ to describe the relation between the element width w_{EL} (azimuthal angle) and relative azimuthal displacement d_{EL} dependent on the time step size Δt is introduced as

$$\chi = \frac{w_{EL}}{d_{EL}(\Delta t)}. \quad (108)$$

According to the above analysis, it is obvious to assume that the correlation between the time step size and element width is important. If the ratio χ is chosen to be either too large or too small, the solution shows large oscillations and instabilities. Considering the results obtained, the recommended range for the upper and lower limit of the ratio (108) is:

$$1/3 \leq \chi \leq 3. \quad (109)$$

Note that if the ratio is equal to one ($\chi=1$), the special case of a locked step is arrived at, provided that the mesh density is equal in the moving and stationary domains. To further justify this recommendation, the solution in case of $\Delta t=0.834ms$ and δ_{40} is also shown in Fig. 38. Hereby the suggested ratio evaluates to $\chi=3$. It can be seen that the oscillations become attenuated and accuracy is improved.

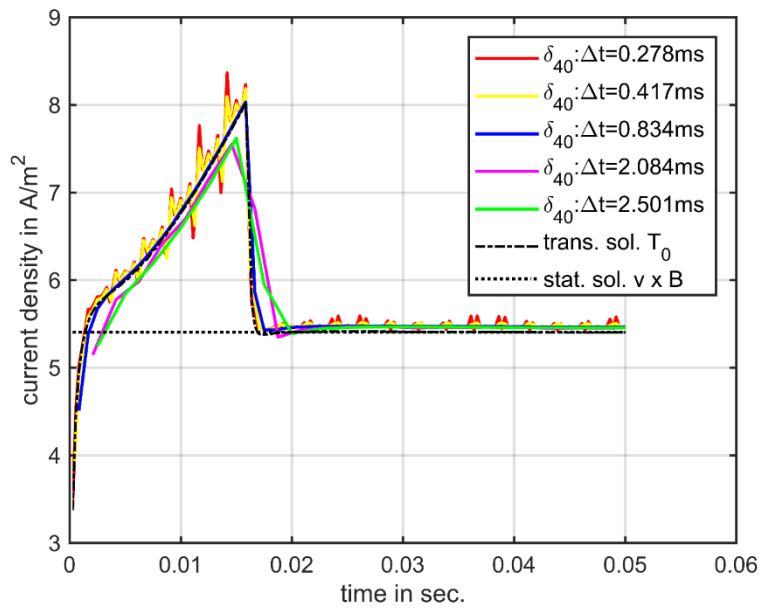


Fig. 38: Comparison of the current density for different time steps in case of $n_{EL}=40$ equidistant elements along the sliding surface.

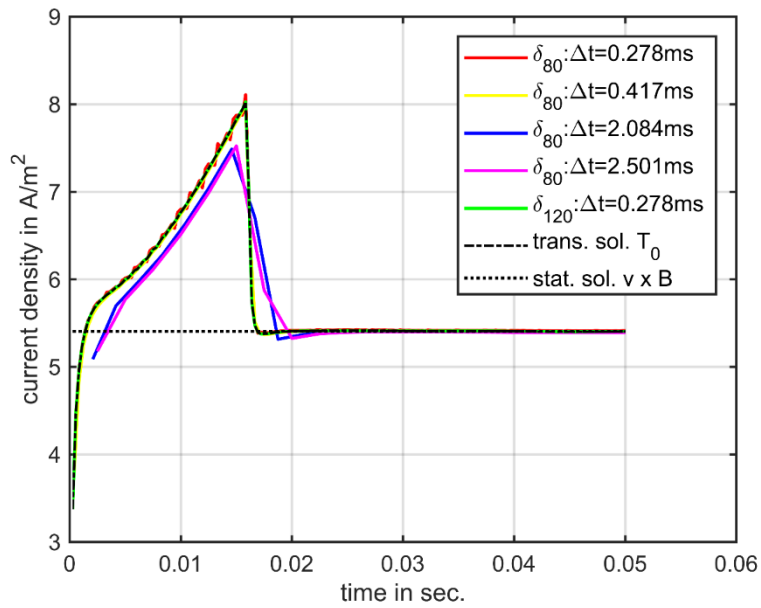


Fig. 39: Comparison of the current density for different time steps in case of $n_{EL}=80$ and $n_{EL}=120$ equidistant elements along the sliding surface.

In Fig. 40, the transient behaviour of the flux density $|\mathbf{B}|$ is compared for different time steps and mesh densities to the reference results. Again, similar oscillations as the ones in the current density $|\mathbf{J}|$ appear. In general, the magnetic flux density evolutions are in good agreement with the transient and stationary reference solutions.

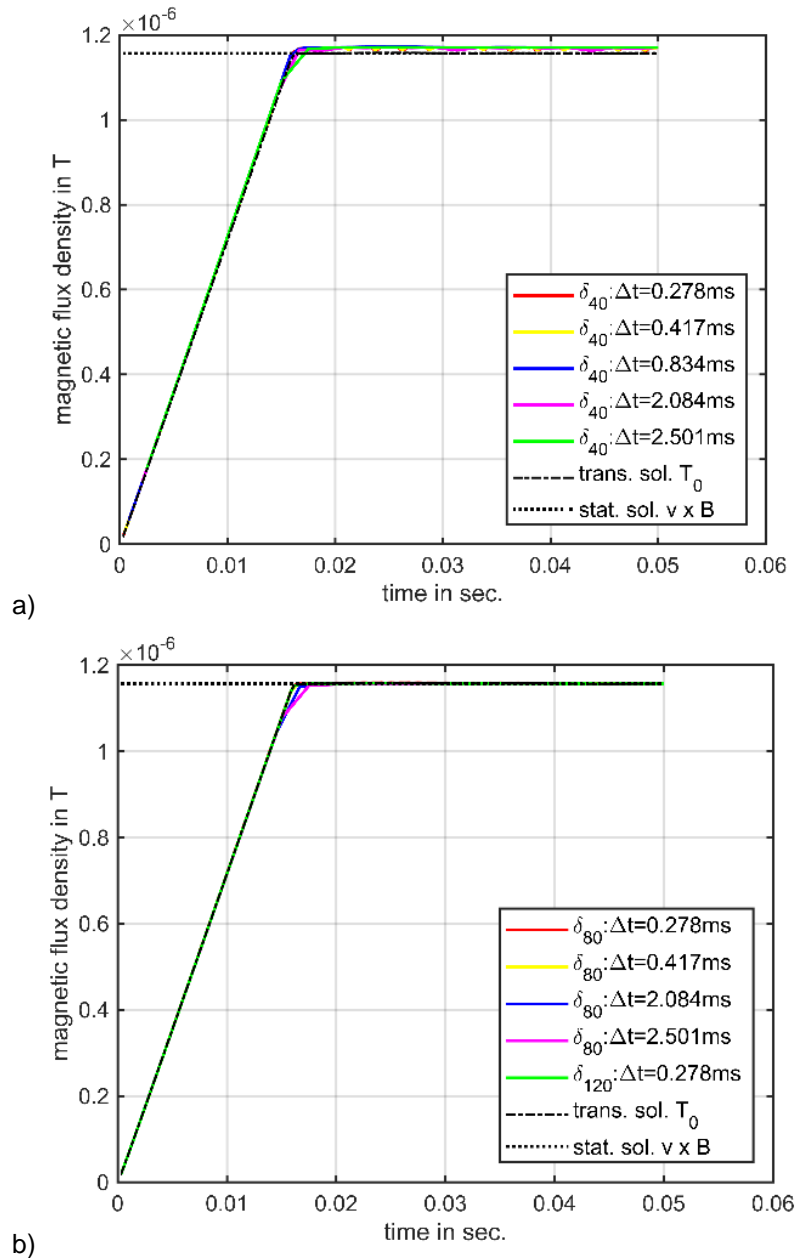
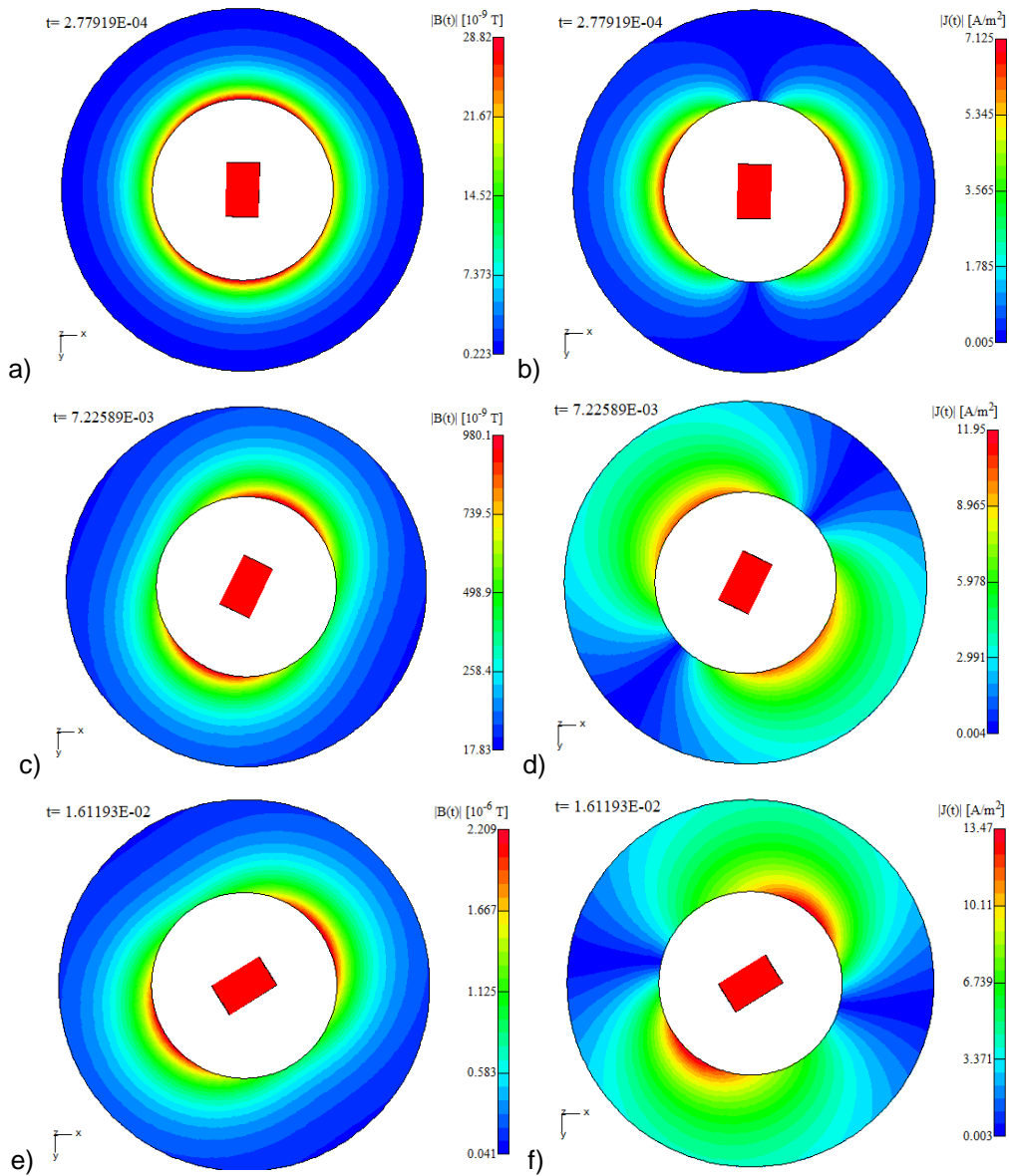


Fig. 40: Comparison of the magnetic flux density for different time steps in case of $n_{EL}=40$ (see a) and in case of $n_{EL}=80$ and $n_{EL}=120$ (see b).

In the following series of field plots shown in Fig. 41, the time evolution of the magnetic flux density $|\mathbf{B}|$ (figures on the left) and current density $|\mathbf{J}|$ (figures on the right) is illustrated at certain time instances. It can be seen that the magnetic field follows the movement of the exciting coil at steady state, whereas the current density exhibits a certain lag during the transient phase.



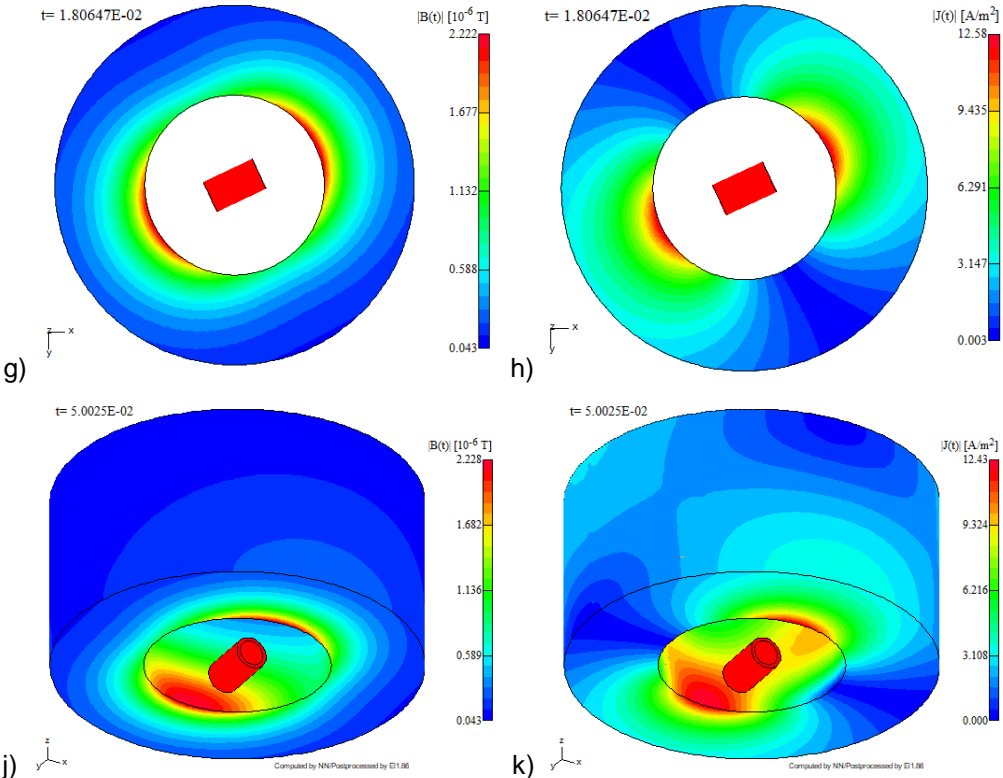


Fig. 41: Time transient evolution of the magnetic flux density $|B|$ on the left and of the current density $|J|$ on the right.

5.2.2.2 Copper shell II: different mesh density

In the second example, the mesh density is chosen to be different in the stationary and moving domains Ω_{stat} and Ω_{mov} . The mesh topology with $n_{EL}=80$ elements in the moving and $n_{EL}=120$ elements in the stationary region is shown in Fig. 42. The transient simulation is carried out with a time step size of $\Delta t=0.278ms$ corresponding to a relative azimuthal displacement of 1 degree between the two domains Ω_{stat} and Ω_{mov} . As a reference, the best solution of the previous analysis is used. This is the case, if the number of elements is set to $n_{EL}=120$ in both domains Ω_{stat} and Ω_{mov} , and the time step size is chosen as $\Delta t=0.278ms$.

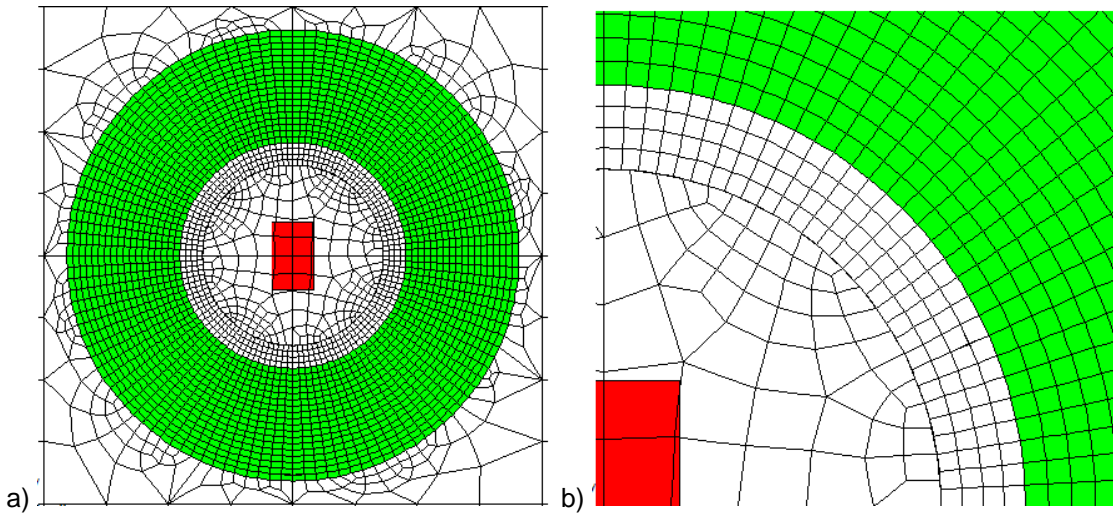


Fig. 42: Mesh topology with different mesh density in both domains, stationary and moving. a) Overview of the mesh at the point of interest b) Detailed view of the mesh along the sliding surface.

The evolutions of the current density $|\mathbf{J}|$ and of magnetic flux density $|\mathbf{B}|$ are shown in Fig. 43 and Fig. 44. It can be observed that, again, oscillations appear at steady state both for the current density and for the magnetic flux density. It is obvious to assume that this behaviour is again due to the correlation between the element width and time step size. Considering the ratio defined in (108) and its suggested limits (109), this ratio is outside the range for the moving domain with $\chi^{mov}=4.5$. For the stationary domain, this ratio evaluates to $\chi^{stat}=3.0$. Accordingly, two different time steps are chosen e.g. $\Delta t=0.417ms$ and $\Delta t=1.112ms$ with the values of χ within the suggested limits (109). Recalculating the solutions of the problem show that the oscillations still exist, but become attenuated. In particular, the oscillations have almost vanished in case of $\Delta t=1.112ms$, and the solution becomes on average closer to the reference solution at steady state. It is expected that the remaining oscillations are due to the insufficient discretization of the cylindrical structures and the problem arising due to geometrically non-matching element facets along the sliding surface. This problem is investigated in the following subsection 5.2.3.

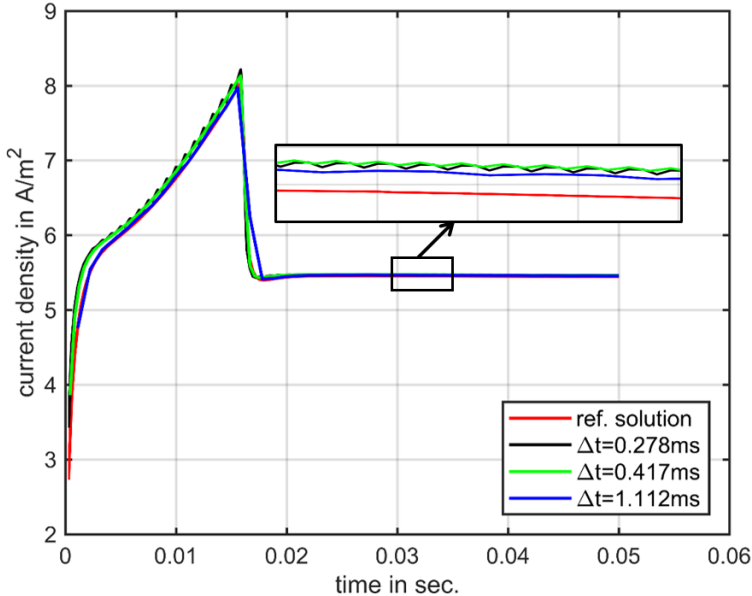


Fig. 43: Comparison of the current density in case of different mesh topologies in the two domains Ω_{stat} and Ω_{mov} .

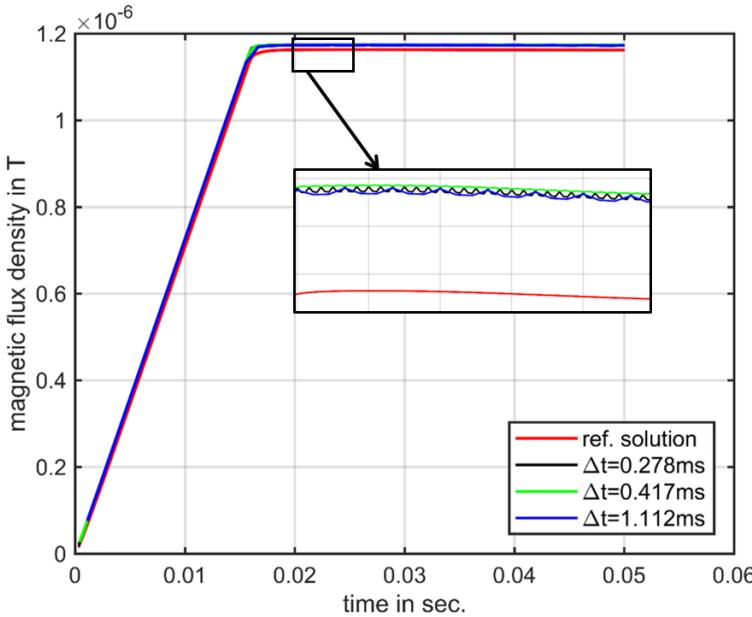


Fig. 44: Comparison of the magnetic flux density in case of different mesh topologies in the two domains Ω_{stat} and Ω_{mov} .

5.2.3 A special problem arising in case of cylindrical sliding surfaces

Previous numerical examples involving cylindrical structures show that even if the finite element mesh is refined, oscillations occur at steady state. This is in contrast to the numerical example with planar structure (see subsection 5.2.1). In that case, the oscillations vanished, if the mesh was refined with the ratio χ defined in (108) kept within the recommended limits $1/3 \leq \chi \leq 3$. It is obvious to assume that these remaining oscillations result from the problem topology, i.e. from the sliding surface being curved. As mentioned in section 4.3, small gaps and overlaps occur in case of cylindrical sliding surfaces when the two domains become displaced relative to each other during rotational movement or the mesh topologies in the two disjoint domains are different. In order to overcome this problem of geometrical errors, a tolerance for the distance between the slave node and the corresponding facet of the master element was enforced. Nevertheless, the numerical results show that, even for fine meshes where the differences in element sizes are kept within appropriate limits and second order elements are used, oscillations of the solution occur. Therefore, this problem arising in case of cylindrical sliding surfaces is investigated in this section.

The discretization of cylindrical structures leads to the problem of non-matching finite element surfaces along the sliding surface Γ_S , if the two disjoint domains Ω^M and Ω^S are displaced relative to each other. This situation is shown in an exaggerated way in Fig. 45 and in particular in Fig. 46 where the geometrical errors like small gaps and overlaps between the element surfaces along the sliding surface are highlighted.

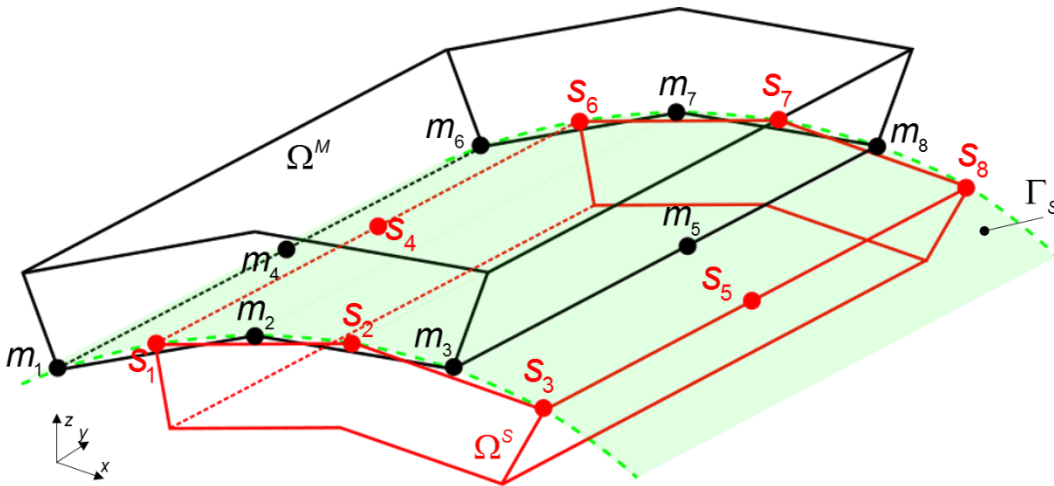


Fig. 45: Two disjoint domains Ω^M and Ω^S with non-conforming mesh along the sliding surface Γ_S . Master nodes m_l and slave nodes s_k can be defined along the interface Γ_S .

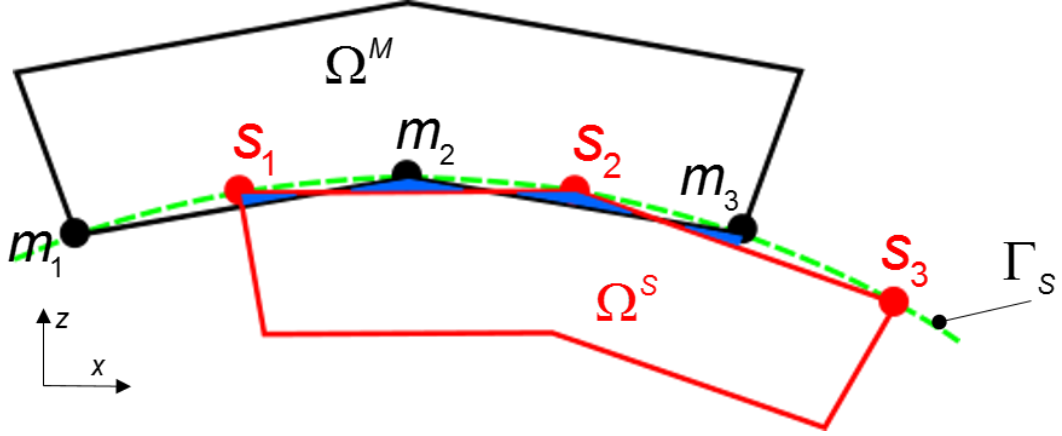


Fig. 46: Front view of two disjoint domains, showing in detail the problem of geometrical errors like small gaps and overlaps between the elements facets, in case of two elements displaced relatively to each other.

In order to quantify this problem of geometrical errors and its influence on numerical solutions, a quality measure of the coupling between a slave node s_k and its corresponding master nodes m_j is introduced as

$$\gamma_k = \sum_{l=1}^{L_k^{(master)}} c_{kl} = \sum_{l=1}^{L_k^{(master)}} N_l^{(master)}(r_k^{(slave)}) \quad (110)$$

with γ_k called the stiffness of coupling.

In case of perfectly matching surfaces like planar ones, the stiffness of coupling evaluates to one: $\gamma_k=1$. However, the stiffness of coupling becomes unequal to one: $\gamma_k \neq 1$ if the element facet of the slave node fails to align with the corresponding facet of the master element, i.e. if non-matching element surfaces along the sliding surface Γ_S appear. To prove these statements, consider a single second order hexahedral master element corresponding to a cube in the local coordinate system $\{\xi, \eta, \zeta\} \in [-1, 1]$ with slave nodes s_k located within this master element (see Fig. 47a).

The local coordinates of some characteristic slave nodes are given in Tab. 2. In case of the conventional coupling strategy with only the nodes belonging to the sliding surface of the master element considered, the number of master nodes is $L_k^{(master)} = 8$. The values of the stiffness of coupling for each slave node are also given in Tab. 8. Indeed, the values of the stiffness of coupling of slave nodes s_3 and s_4 are not equal to one. This inequality to one introduces potential jumps along the sliding interface resulting in additional oscillations of the solution. The values of the stiffness of coupling indicate that the stiffness of coupling decreases if the distance between the slave node and the corresponding facet of the master element including the master nodes become greater. This decrease is especially striking in case of slave node s_4 whose location is close to the origin of the local coordinate system of the master element (i.e. to the centre of the element).

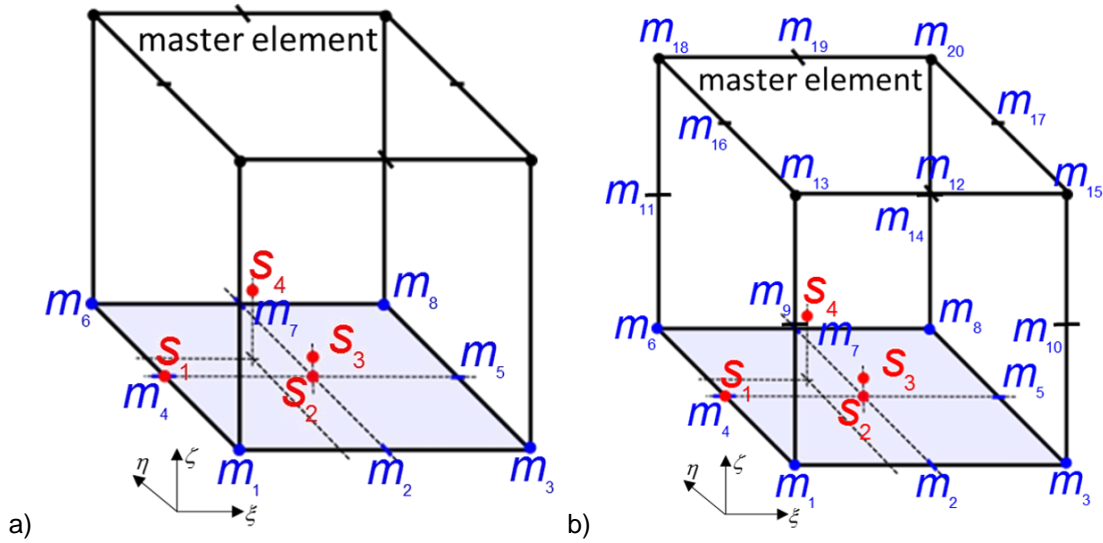


Fig. 47: Illustrative example to consider different slave node locations and different number of corresponding master nodes. a) Conventional approach with $L_k^{(master)} = 8$ b) New approach with $L_k^{(master)} = 20$.

number of master nodes	slave node $s_k(\xi, \eta, \zeta)$	stiffness of coupling γ_k
$L_k^{(master)} = 8$	$s_1(-1, 0, -1)$	$\gamma_1 = 1.0$
	$s_2(0, 0, -1)$	$\gamma_2 = 1.0$
	$s_3(0, 0, -0.9)$	$\gamma_3 = 0.8550$
	$s_4(-0.4, 0.3, -0.5)$	$\gamma_4 = 0.3750$
$L_k^{(master)} = 20$	$s_1(-1, 0, -1)$	$\gamma_1 = 1.0$
	$s_2(0, 0, -1)$	$\gamma_2 = 1.0$
	$s_3(0, 0, -0.9)$	$\gamma_3 = 1.0$
	$s_4(-0.4, 0.3, -0.5)$	$\gamma_4 = 1.0$

Tab. 8: Stiffness of coupling in case of the conventional approach where the number of master nodes is set to $L_k^{(master)} = 8$, and in case of the new approach where the number of master nodes is set to $L_k^{(master)} = 20$.

To discuss the behaviour of the stiffness of coupling as shown before, consider that the stiffness of coupling in case of $L_k^{(master)} = 8$ is a constant function equal to one, along a facet of the master element:

$$\tilde{\gamma} = \sum_{l=1}^8 N_l^{(master)}(\mathbf{r}_k^{(slave)}). \quad (111)$$

If the slave node fails to align with the facet comprising the corresponding master nodes, the stiffness of coupling become evaluated within the master element as:

$$\gamma'_k = \sum_{l=1}^{20} \tilde{\gamma} N_l(\mathbf{r}_k^{(slave)}). \quad (112)$$

Fig. 48 illustrates the stiffness of coupling where two local coordinates are kept constant, e.g. $\{\xi_c, \eta_c\} \in [-1, 1]$, and the third coordinate is varied as $-1 \leq \zeta \leq 1$. Hence, the stiffness of coupling become dependent on the ζ -coordinate only.

In contrast to the case of $L_k^{(master)} = 8$ corresponding master nodes, the stiffness of coupling becomes a constant function equal to one within the master element if $L_k^{(master)} = 20$ corresponding nodes are chosen (see Fig. 48).

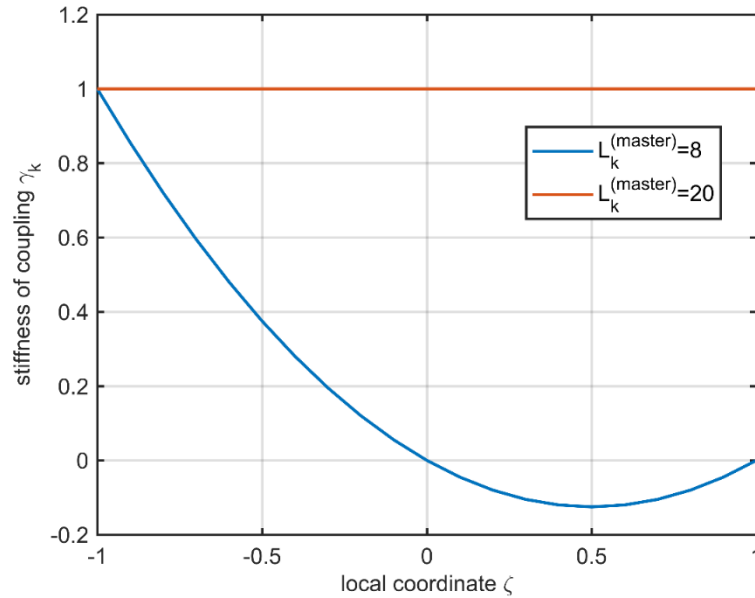


Fig. 48: Stiffness of coupling dependent only on the local coordinate ζ for the cases of $L_k^{(master)} = 8$ and $L_k^{(master)} = 20$ corresponding master nodes.

In such cases, e.g. in case of s_3 and s_4 , it is more suitable to use all nodes of the master element instead of just the nodes belonging to the sliding surface, i.e., setting the number of corresponding master nodes to $L_k^{(master)} = 20$ in this example (see Fig. 47b). For all slave nodes, the stiffness of coupling becomes equal to one, resulting in no artificial potential jumps along the sliding surface. This improvement is tested in the following with the previous numerical example involving a cylindrical structure.

To illustrate this simple technique, the two cases of equal mesh density (see section 5.2.2.1) and different mesh density (see section 5.2.2.2) in the two disjoint domains Ω_{stat} and Ω_{mov} are considered again. In both cases the transient simulation is carried out with a time step size of $\Delta t = 0.278 \text{ ms}$ which corresponds to a relative azimuthal displacement between the domains Ω_{stat} and Ω_{mov} of 1 degree. The numerical values of the z-component $J_z(t)$ of the current density are compared for both cases in Fig. 49 and, in detail, in Fig. 50 showing the stationary solution. The case of equal mesh density is referred to as δ_{40} and the case of different mesh densities as $[\delta_{120}, \delta_{80}]$. Indeed, the oscillations of the solutions become attenuated, if a larger set of master nodes is used. In case of equal mesh density, the oscillations still exist, but this is due to the mesh being coarse. If the mesh is refined, the oscillations decrease as indicated by the curve of the second case with different mesh densities and using the conventional approach of $L_k^{(master)} = 8$ master nodes per element. In case of different mesh densities and using a larger set of master nodes $L_k^{(master)} = 20$, the oscillations are completely eliminated and the solution is in a very good agreement with the stationary solution (see Fig. 50).

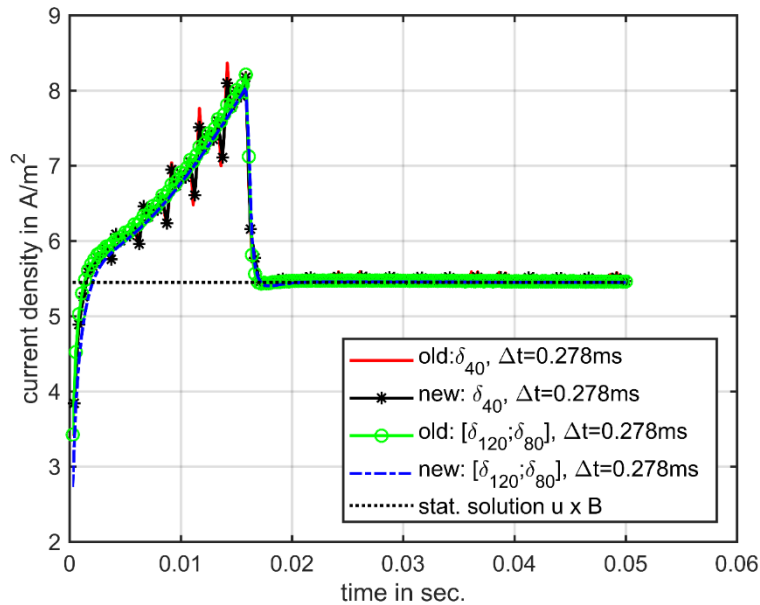


Fig. 49: Comparison of the current density for the conventional (old) and new coupling approach, $L_k^{(master)} = 8$ and $L_k^{(master)} = 20$ per element.

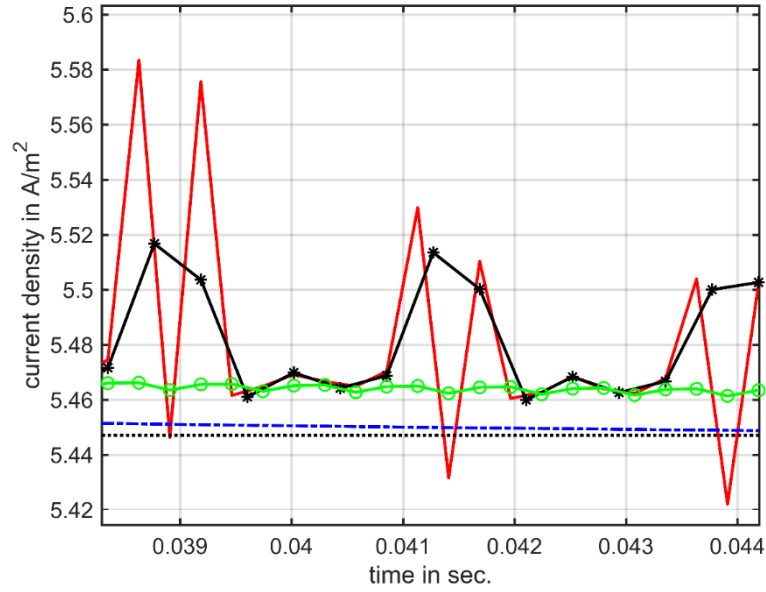


Fig. 50: Detailed view of the comparison of the current density at steady state for the conventional (old) and new coupling approach, $L_k^{(master)} = 8$ and $L_k^{(master)} = 20$ per element.

In the following, the stiffness of coupling γ_k is averaged over the time interval T for all slave nodes $s_1 \dots s_8$ of a particular slave element situated in the symmetry plane. A comparison of the stiffness of coupling is made between the cases of the conventional ($L_k^{(master)} = 8$) and new ($L_k^{(master)} = 20$) approaches. Fig. 51 shows the case of equal mesh density δ_{40} along the sliding surface. In case of the conventional approach, the stiffness of coupling is not balanced within the slave element. It is obvious to assume that this indicates an additional reason for larger oscillations as shown in previous numerical results and in particular in Fig. 49 and Fig. 50. As expected, refining the mesh results in a more balanced coupling of all slave nodes within one element as indicated in Fig. 52, although different mesh densities are used in the stationary and moving domains. Using a larger set of master nodes per element according to the new approach, the stiffness of coupling of each slave node becomes equal to one.

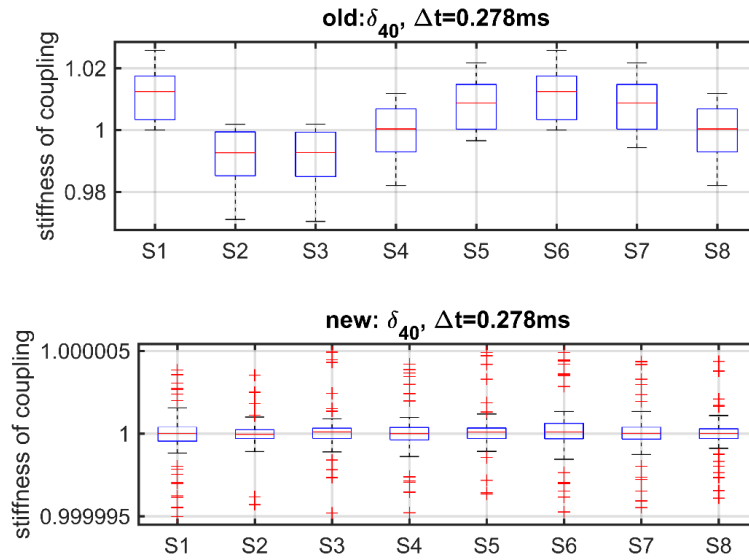


Fig. 51: Stiffness of coupling averaged over the period of time for the old and new coupling approaches, $L_k^{(master)} = 8$ and $L_k^{(master)} = 20$ at equal mesh density in Ω_{stat} and Ω_{mov} .

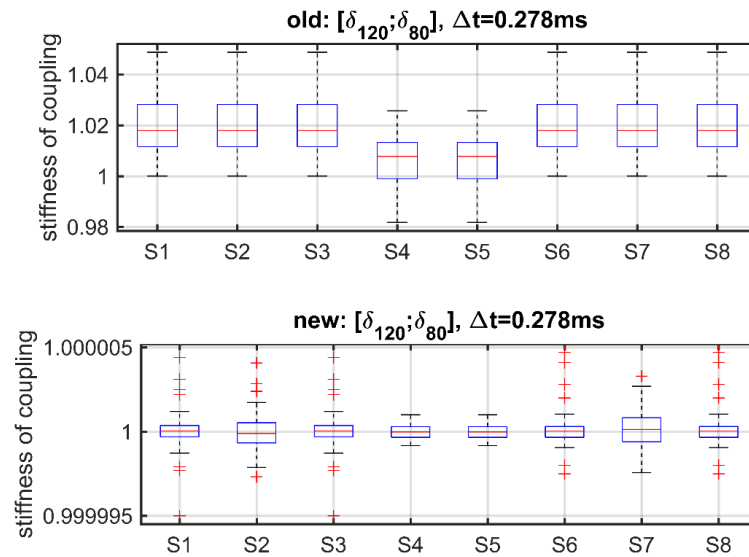


Fig. 52: Stiffness of coupling averaged over the period of time for the old and new coupling approaches, $L_k^{(master)} = 8$ and $L_k^{(master)} = 20$ at different mesh densities in Ω_{stat} and Ω_{mov} .

6 Discussion and conclusion

This thesis presents a powerful alternative to standard methods used in commercial finite element software packages to couple two disjoint domains with independent meshes. The main findings of the investigated non-conforming mesh method are recapitulated in this chapter. Besides a conclusion of present thesis, some proposals for future work are also given.

6.1 Recapitulation of obtained findings

The error analysis made while treating magneto-static problems showed that, on the one hand, the error decreases at similar rates as known from the classical finite element method. On the other hand, the error increases with greater relative displacement between two elements. When treating the case of different mesh densities between the two independent meshes, it has become obvious that the non-conforming mesh method is well suited to couple domains with different mesh topologies without loss of accuracy. A certain limit of the ratio between the meshes of the master and slave domain has been obtained. It has been understood that the master domain cannot be refined excessively. Contrarily, the slave domain can be discretized much finer than the master domain.

The treatment of motion induction (time transient problems) in case of planar and rotational movement has shown that the results are in a good agreement with the results obtained from references. However, the results have shown a dependence on the element width and time step length. Indeed, a limit on the ratio between element width and time step length (size of relative displacement) could be defined. Once a time step length or element width is chosen in such manner as to end up within this defined limit, the results become more accurate and stable after the transients are gone.

While analysing the rotational movement, a special problem arises in case of cylindrical sliding surfaces. The issue of geometrical errors, e.g. small gaps or overlaps between the finite elements along the sliding surface, causes instabilities and loss of accuracy. Hence, the coupling strategy for cylindrical structures has been improved. Here, an increased number of corresponding master nodes results in a significant improvement of the obtained results.

6.2 Suggestions

The topic of periodic boundary conditions has already been raised in case of static problems where no relative movement between two disjoint domains has been considered. The obtained results are promising, but a deeper analysis is still missing. Further, the investigated concept should be adopted to time transient problems to provide the possibility of problem model reduction by means of topological periodicities.

A difficult problem arises for dynamic analyses of electrical machines if eccentricity of the rotating rotor has to be taken into account. The solution of the issue of geometrical errors in case of cylindrical sliding surfaces raises the idea to adopt the coupling strategy further to be able to take account of eccentricity. An idea would be, to introduce a sliding volume instead of a sliding surface in the air gap. Here, the number of slave nodes have to be increased to all nodes of a slave element that belongs to that sliding volume. Of course, this approach has some limitations and restrictions regarding the degree of eccentricity, e.g. the rotor is not allowed to contact the stator. Apparently, this would arise a challenging issue. Initially the coupling elements are situated in the air gap and then have to assume the material properties of the elements situated in e.g. stator iron or rotor iron. However, it is believed that a small degree of eccentricity can be taken into account as long as the coupling between the two domains takes place in the air gap region.

6.3 Conclusion

The present thesis contributes to the topic of domain coupling and presents a clever and accurate alternative to popular methods in this field of research. The investigated non-conforming mesh method proposes a coupling strategy that uses the nodal potentials only to couple two disjoint domains with two independent meshes along a sliding surface. The coupling of the nodes pursue the principle of a master/slave interpolation.

Combining the non-conforming mesh method with the $\mathbf{T},\Phi-\Phi$ formulation, where the conducting medium is modelled with the aid of the current vector potential and the non-conducting medium with the magnetic scalar potential, reduces the number of unknowns significantly and, therefore, reduces computational costs. The latter is a crucial point in case of three-dimensional, time transient analysis of electromagnetic problems. Especially the combination of domain coupling methods with the $\mathbf{T},\Phi-\Phi$ formulation are not treated so far or have been less in focus over the past decades. Traditionally, the methods used for coupling utilize magnetic vector potential formulations with the drawback of a high number of degrees of freedom and increased computational burden.

When applying the non-conforming mesh method to three-dimensional applications, although of academic nature, the practicability to analyse the dynamical behaviour has been shown. Further, the limits of the investigated methods have been addressed as well as recommendations for use have been made. The non-conforming mesh method is applicable to a wide range of electromagnetic problems and promises to be a powerful tool for further research.

Appendix A: Source field calculation for complex conductor structures

The following discussion has been presented during a poster session in the biennial International Symposium on Electromagnetic Phenomena in Nonlinear Circuits (EPNC), Helsinki, 2016.

If the current density \mathbf{J}_0 occurs in massive conductors and is hence not a priori known, the corresponding static current flow problem could be solved in terms of a current vector potential \mathbf{T}_0 represented by edge basis functions to yield the approximation

$$\mathbf{T}_0 \approx \sum_{k=1}^{n_e} t_k \mathbf{N}_k . \quad (113)$$

In many practical cases, however, stranded conductors occur and, hence, the current density is known, it is constant over any cross section of the conductor.

In such cases one could integrate the Biot-Savart field over all edges of the finite element mesh to yield the values t_k . This is computationally very demanding in case of complex coil shapes since all the Biot-Savart volume integrals have to be evaluated numerically.

An alternative has been proposed in [56] to solve for a Coulomb-gauged nodal finite element representation of \mathbf{T}_0 with its curl given by \mathbf{J}_0 . This would still have to be integrated over all edges of the finite element mesh involving additional numerical burden.

If the current density is known, it is also possible to generate a tree in the graph formed by the finite element mesh and assign the value zero to t_k along the tree edges and compute the integral of the current density over the loops generated by each co-tree edge to yield the values t_k over the co-tree edges, see [57], [54]. In order to dispense with the necessity of identifying the loops, the authors in [58] have proposed to solve for the tree-gauged edge element representation of \mathbf{T}_0 with its curl given by \mathbf{J}_0 .

Another possibility is now to use the method of [58] without gauging the vector potential. It is well known that not using a gauge results in much better conditioned matrix than the one resulting in the gauged version [7]. The equations obtained by thus projecting the curl of \mathbf{T}_0 to \mathbf{J}_0 over the problem domain Ω are:

$$\sum_{k=1}^n t_k \int_{\Omega} \text{curl} \mathbf{N}_i \cdot \text{curl} \mathbf{N}_k d\Omega = \int_{\Omega} \mathbf{J}_0 \cdot \text{curl} \mathbf{N}_k d\Omega . \quad (114)$$

Although we have as many degrees of freedom as there are edges in the finite element mesh, the resulting system is well conditioned (although singular) and can be solved very efficiently by preconditioned conjugate gradient techniques.

The obtained equation system (114) requires the knowledge about the value and direction of the current density along the whole conductor of any shape. It is assumed that the information about the current density is given for further considerations. From the view point of the finite element mesh of the problem domain Ω where the projection of the curl of \mathbf{T}_0 to \mathbf{J}_0 and solving the current flow problem takes place, each integration point of the finite element mesh needs the value and direction of the current density \mathbf{J}_0 . If the integration point is within the conductor domain Ω_c , the position of the point has to be identified to determine the direction and value of the current density \mathbf{J}_0 . If the integration point is not within the conductor domain Ω_c , the current density \mathbf{J}_0 becomes zero. Therefore, the current density \mathbf{J}_0 can be obtained as

$$\mathbf{J}_0(\rho_i) = \begin{cases} \mathbf{J}_c, \rho_i \in \Omega_c \\ 0, \text{else} \end{cases} \quad (115)$$

where \mathbf{J}_c is the given current density of the conductor. An example to illustrate this mapping of the current density can be seen at Fig. 53. The value of the current density \mathbf{J}_c is given by the cross section A_c and by the given current I . The direction of the current density is obtained as the normalized normal vector of the conductor cross section $\mathbf{e}_{Ac} = \mathbf{e}_n / \|\mathbf{e}_n\|$. Therefore, the current density \mathbf{J}_c can be obtained as

$$\mathbf{J}_c = I / A_c \mathbf{e}_{Ac}. \quad (116)$$

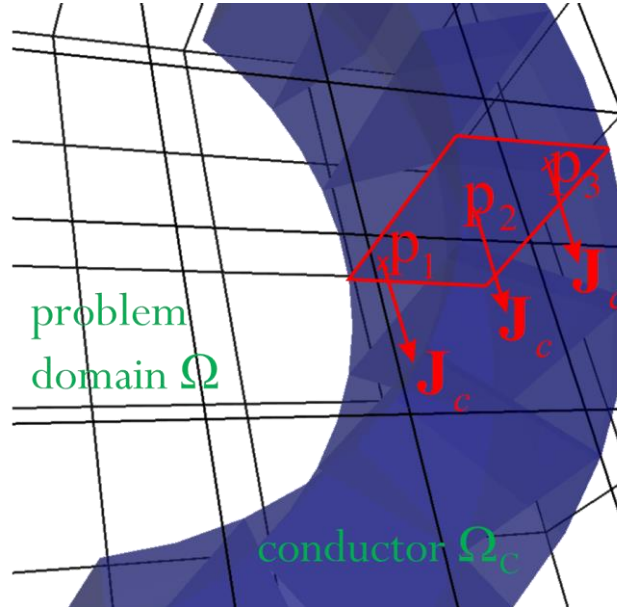


Fig. 53: Illustration of an arbitrary shaped conductor getting mapped onto the problem domain Ω . The current density \mathbf{J}_0 at integration points within the conductor domain Ω_c becomes \mathbf{J}_c , otherwise the current density \mathbf{J}_0 is zero.

Numerical example:

As an example, let us consider a stranded helical conductor shown in Fig. 54. The conductor consists of three windings of height $h_w=7.5mm$ with a slope of $s=10mm$ per turn. In total the helical conductor has a height of $h_c=37.5mm$ with an inner radius $R_i=10mm$ and an outer radius of $R_o=15mm$. The current density is assumed to be constant over any cross section of the winding. The helical conductor is nested in the centre of the problem domain of dimensions $a=40mm$; $b=50mm$; $h_p=60mm$.

The finite element mesh used is made of second order hexahedral elements, i.e. the shape of the winding is not modelled by the mesh. In order to obtain data of the current density \mathbf{J}_0 two data lines: *line 1* and *line 2* are taken parallel to the x -axis and z -axis in such manner that the current density along them is characteristic of the helical conductor

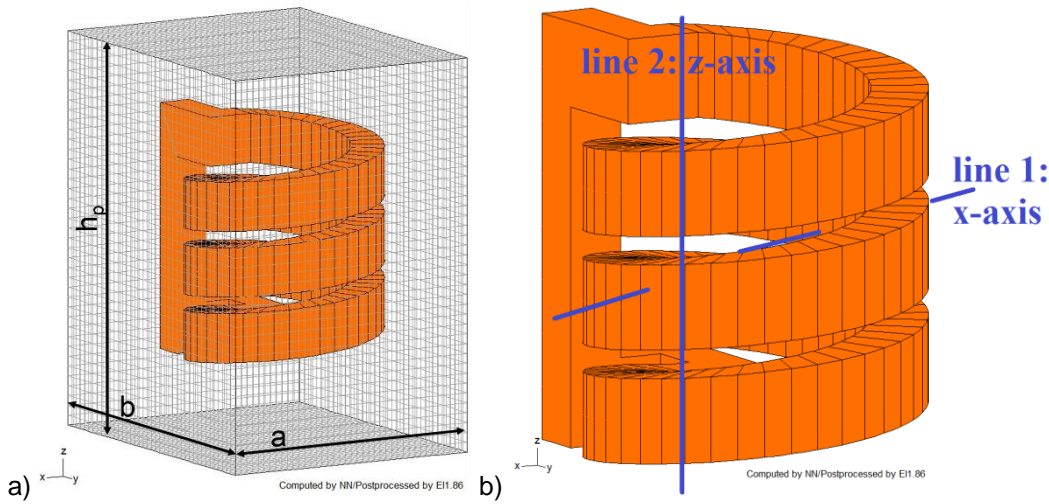


Fig. 54: Numerical example: a) Helical conductor within a hexahedral finite element mesh. b) Detailed view of the helical conductor showing the two data lines, parallel to the x and z -axis, respectively.

As the question about the computational costs to solve the equation system (4) is of great interest, the investigated problem model was solved for a different number of elements. The number of elements is chosen in such a way that the resulting mesh ranges from a very coarse to a very dense finite element grid. For solving the equation system (4), the incomplete Cholesky preconditioned conjugate gradient method (ICCG) has been used on an Intel Core i7-5820 (6x 3,60Ghz) architecture. In Tab. 9, the investigated problems with the number of elements, of degrees of freedom, of ICCG iterations and computational time are listed.

The current density computed in the finite element mesh with a number of 409600 elements and with a number of about 5.02 million degrees of freedom is represented by arrows in Fig. 55a and Fig. 55b illustrates the convergence time in logarithmic scale against the number of degrees of freedom. As Fig. 5 shows, the convergence time rises in a sub-quadratic manner, as the slope of the curve is about 1.5. The current density obtained for a dense mesh of 409600 elements along the two data lines (see Fig. 54), parallel to the x -axis and z -axis, respectively is shown in Fig. 56a for *line 1* and in Fig. 56b for data line: *line 2*. Both data lines run within the

range of the problem model boundaries. In both cases shown in Fig. 56a and Fig. 56b, the characteristics of the helical conductor can be clearly seen, as the current density \mathbf{J}_0 becomes \mathbf{J}_c inside the domain of the conductor and zero elsewhere. The value of the current density \mathbf{J}_0 remains nearly constant over the data lines.

Intel Core i7-5820 (6x 3,60Ghz)			
elements	DOF	ICCG iterations	time [sec.]
2560	34456	85	0,500
20480	260528	191	9,766
69120	862536	312	54,234
81920	1018640	216	44,016
163840	2024800	437	178,969
204800	2523248	380	194,750
245760	3021696	335	204,781
286720	3520144	305	219,984
327680	4018592	342	277,891
368640	4517040	311	286,375
409600	5015488	311	318,844

Tab. 9: Convergence behaviour depending on the number of degrees of freedom and number of elements.

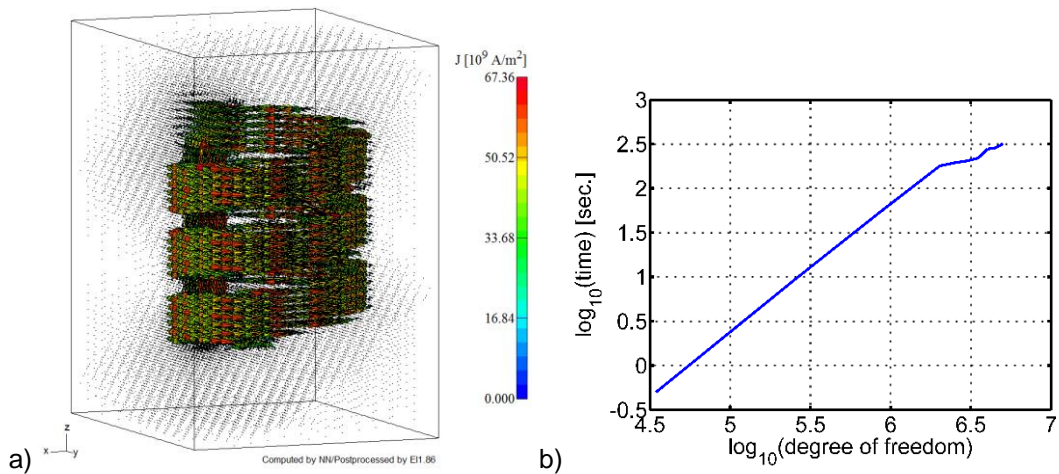


Fig. 55: a) Current density of the hexahedral mesh. b) Convergence time behaviour of the incomplete Cholesky preconditioned conjugate gradient method according to the degree of freedom.

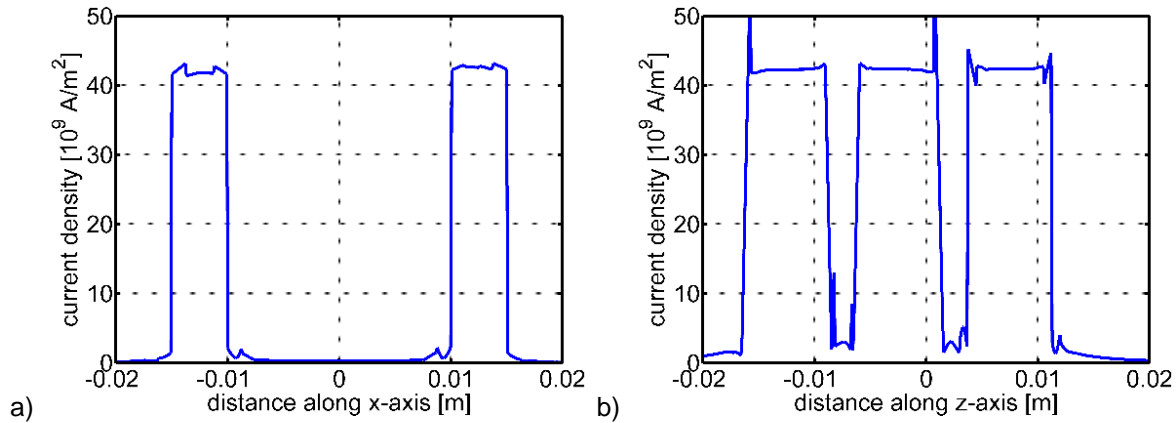


Fig. 56: a) Current density J_0 on the hexahedral mesh taken along *line 1*. b) Current density J_0 on the hexahedral mesh taken along *line 2*.

Discussion:

The current density distribution shown in Fig. 55. is in excellent agreement with the current density of the helical conductors and the good representation of the conductor is reaffirmed by the data taken along line 1 and line 2 shown in Fig. 56. As it can be seen in both figures Fig. 56a and Fig. 56b, the current density J_0 show peaks at the edges of the conductor boundaries, but remains constant within the conductor domain. It is assumed that this peak phenomenon at the end region comes from the density of the finite element mesh and therefore the ability of the finite element mesh of the problem domain to represent the shape of the conductor. This is an obvious restriction to the finite element mesh of the problem domain, that the finite element mesh needs to be as dense as necessary at the region where the conductor appears, in order to get the right representation of the conductor. Overall, the edge element representation of T_0 has been obtained at reasonable computational costs, and the method is applicable for any conductor shape as long as the current density of the conductor can be assumed to be given.

Bibliography

- [1] O. C. Zienkiewicz, R. L. Taylor and J. Z. Zhu, "The Finite Element Method: Its Basis and Fundamentals," *Elsevier Science*, 2013.
- [2] R. T. Fenner, "Finite Element Methods for Engineers," *World Scientific Publishing Company*, 2013.
- [3] H. R. Schwarz, "Methode der finiten Elemente," *B. G. Teubner Stuttgart*, 1991.
- [4] A. C. Polycarpou, "Introduction to the Finite Element Method in Electromagnetics," *Morgan & Claypool Publishers*, 2006.
- [5] O. Bíró and K. Richter, "CAD in Electromagnetism," *Advances in Electronics and Electron Physics*, vol. 82, pp. 1-96, 1991.
- [6] P. Olszewski, "Expansion of periodic boundary condition for 3-D FEM analysis using edge elements," *IEEE Transactions on Magnetics*, vol. 28, pp. 1084-1087, 1992.
- [7] O. Bíró, "Edge element formulations of eddy current problems," *Computer Methods in Applied Mechanics and Engineering*, vol. 169, no. 3-4, pp. 391-405, 1991.
- [8] J. Jin, *The finite element method in electromagnetics*, John Wiley&Sons, Inc, 2002.
- [9] O. Bíró and K. Preis, "On the use of the magnetic vector potential in the finite element analysis of three-dimensional eddy currents," *IEEE Transactions on Magnetics*, vol. 25, no.4, pp. 3145-3159, 1989.
- [10] I. Baksh, O. Bíró, and K. Preis, "Skin effect problems with prescribed current condition," in *Proceedings of the 14th International IGTE Symposium on Numerical Field Calculation in Electrical Engineering*, 2010.
- [11] O. Bíró, K. Preis, and K. R. Richter, "On the use of the magnetic vector potential in the nodal and edge finite element analysis of 3D magnetostatic problems," *IEEE Transactions on Magnetics*, vol. 32, no. 3, pp. 651-654, 1996.
- [12] R. Albanese and G. Rubinacci, "Solution of three dimensional eddy current problems by integral and differential methods," *IEEE Transactions on Magnetics*, vol. 24, no. 1, pp. 98-101, 1988.
- [13] P. J. Leonard, R. J. Hill-Cottingham, and D. Rodger, "3D finite element models and external circuits using the $\mathbf{A}\Psi$ scheme with cuts," *IEEE Transaction on Magnetics*, vol. 30, no. 5, pp. 3220-3223, 1994.
- [14] F. Henrotte and K. Hameyer, "An algorithm to construct the discrete cohomology Basis functions required for magnetic scalar potential formulation without cuts," *IEEE Transactions on Magnetics*, vol. 39, no. 3, pp. 1167-1170, 2003.
- [15] M. Urabe, "Galerkin's procedure for nonlinear periodic systems," *Archive for Rational Mechanics and Analysis*, vol. 20, no. 2, pp. 120-152, 1965.
- [16] J. N. Reddy, "Energy Principles And Variational Methods In Applied Mechanics", Second Edition, *John Wiley & Sons*, 2002.
- [17] A. Bossavit and I. D. Mayergoyz, "Computational Electromagnetism: Variational Formulations, Complementarity, Edge Elements", *Elsevier Science*, 1998.
- [18] E. Wang, T. Nelson and R. Rauch, "Back to elements-tetrahedra vs. hexahedra," in *Proceedings of the 2004 International ANSYS Conference*, 2004.
- [19] Z. Ren and N. Ida, "Solving 3D eddy current problems using second order nodal and edge elements," *IEEE Transactions on Magnetics*, vol. 36, no. 4, pp. 746-750, July 2000.
- [20] P. Dular, J. Y. Hody, A. Nicolet, A. Genon and W. Legros, "Mixed finite elements associated with a collection of tetrahedral, hexahedra and prisms," *IEEE Transactions on Magnetics*, vol. 30, no. 5, pp. 2980-2983, 1994.
- [21] Z. Ren, "T- Ω formulation for eddy current problems in multiply connected regions," *IEEE Transactions on Magnetics*, vol. 38, pp. 557-560, 2002.
- [22] Z. Ren, "Computation of magnetostatic field using second order edge elements in 3D," *Compel- The international Journal for computation and mathematics in electrical and electronic engineering*, vol. 18, no. 3, pp. 361-371, 1999.

- [23] K. Simonyi, "Foundations of Electrical Engineering: Fields-Networks-Waves", *Elsevier Science*, 2016
- [24] R. P. Feynman, R. B. Leighton and M. Sands, "The Feynman Lectures on Physics: The New Millennium Edition: Mainly Electromagnetism and Matter", Basic Books, no. 2. 2015.
- [25] J. D. Jackson, K. Mueller and M. Diestelhorst, „Klassische Elektrodynamik“, *de Gruyter*, 2013.
- [26] K. Preis, I. Bardi, O. Bíró, C. Magele, W. Renhart, K. R. Richter and G. Vrisk, "Numerical analysis of 3D magnetostatic fields," *IEEE Transactions on Magnetics*, vol. 27, no. 5, pp. 3798-3803, 1991.
- [27] J. Simkin and C. W. Trowbridge, "On the use of the total scalar potential on the numerical solution of fields problems in electromagnetics," *Int. Journal for Numerical Methods in Engineering*, vol. 14, no. 3, pp. 423-440, 1979.
- [28] Y. Saad, *Iterative Methods for Sparse Linear Systems*, Society for Industrial and Applied Mathematics, 2003.
- [29] O. Axelsson, *Iterative solution methods*, Cambridge university press, 1996.
- [30] M. Benzi, "Preconditioning techniques for large linear systems: A survey," *Journal of Computational Physics*, vol. 182, no. 2, pp. 418-477, 2002.
- [31] D.S Kershaw, "The incomplete Cholesky-conjugate gradient method for the iterative solution of systems of linear equations," *Journal of Computational Physics*, vol. 26, no. 1, pp. 43-65, 1978.
- [32] Z. Z. Bai, "Motivations and realizatons of Krylov subspace methods for large sparse linear systems," *Journal of Computational and Applied Mathematics*, vol. 283, pp. 71-78, 2015.
- [33] R. Plasser, Y. Takahashi and O. Bíró, "Comparison of various methods for the finite element analysis of nonlinear, periodic eddy-current problems," in *16th IGTE Symposium 2014*, 2014.
- [34] G. Koczka and O. Bíró, "Fixed-point method for solving non linear periodic eddy current problems with T, Φ - Φ formulation," *Compel- The international journal for computation and mathematics in electrical and electronic engineering*, vol. 29, no.6, pp. 1444-1452, 2010.
- [35] O. Bíró, and K. Preis, "Finite element calculation of time-periodic 3d eddy currents in nonlinear media," in *Selected papers of the 3rd Japan-Hungary Joint Seminar on Applied Electromagnetics in Materials and Computational Technolog*, pp. 62-74, Elsevier B. V., 1995.
- [36] W. Dahmen and A. Reusken, "Numerik für Ingenieure und Naturwissenschaftler," *Springer-Verlag*, 2006.
- [37] D. Rodger, H. Lai and P. Leonard, "Coupled elements for problems involving movement," *IEEE. Trans. Magn.*, vol. 26, no. 2, pp. 548-550, Mar 1990.
- [38] H. Lai, D. Rodger and P. Leonard, "Coupling meshes in 3d problems involving movements," *IEEE. Trans. Magn.*, vol. 28, no. 2, pp. 1732-1734, Mar 1992.
- [39] C. Golovanov, J. L. Coulomb, Y. Marechal and G. Meunier, "3D mesh connection techniques applied to movement simulation," *IEEE. Trans. Magn.*, vol. 34, pp. 3359-3362, Sep 1998
- [40] B. F. Belgacem and Y. Maday, "The mortar element method for three dimensional finite elements," *RAIRO-Modelisation mathematique et analyse numerique*, vol. 31. Jg., Nr. 2, pp. 289-302, 1997.
- [41] R. Becker, P. Hansbo and R. Stenberg, "A finite element method for domain decomposition with non-matching grids," *ESAIM: Mathematical Modelling and Numerical Analysis*, vol. 37, pp. 209-225, 2003
- [42] R. Stenberg, "On some techniques for approximating boundary conditions in the finite element method", *Journal of Computational and applied Mathematics*, vol. 63, pp. 139-148, 1995.
- [43] R. Stenberg, "Mortaring by a method of J. A. Nitsche," *Computational mechanics*, 1998.

-
- [44] P. Ponomarev, L. Aarniovuori and J. Keränen, "Selection of optimal slice count for multi-slice analysis of skewed induction motors," *IECON 2017 - 43rd Annual Conference of the IEEE Industrial Electronics Society*, Beijing, China, 2017, pp. 2149-2153.
- [45] R. Perrin-Bit and J. L. Coulomb, "A three dimensional finite element mesh connection for problems involving movement," *IEEE. Trans. Magn.*, vol. 31, pp. 1920-1923, 1995.
- [46] X. Shi, Y. Le Menach, J.-P. Ducreux and F. Piriou, "Comparison Between the Mortar Element Method and the Polynomial Interpolation Method to Model Movement in the Finite Element Method," *IEEE. Trans. Magn.*, vol. 44, pp. 1314-1317, 2008.
- [47] X. Shi, Y. Le Menach, "Comparison of slip surface and moving band techniques for modelling movement in 3D with FEM," *COMPEL – The international journal for computation and mathematics in electrical and electronic engineering*, vol. 25 No.1, pp. 17-30, 2006.
- [48] D. Rodger, T. Karaguler, and P. J. Leonard, "A formulation for 3D moving conductor eddy current problems," *IEEE Transactions on Magnetism*, vol. 25, 1989, pp. 4147-4149.
- [49] D. Rodger, and H. C. Lai, "A comparison of formulations for 3D finite element modelling of electromagnetic launchers," *IEEE Transactions on Magnetism*, vol. 37, 2001, pp. 135-138.
- [50] D. Rodger, H. C. Lai, and P. J. Leonard, "A comparison of finite-element models for 3-D rotating conductors," *IEEE Transactions on Magnetism*, vol. 38, 2002, pp. 537-540.
- [51] D. Rodger, P. J. Leonard, and T. Karaguler, "An optimal formulation for 3D moving conductor eddy current problems with smooth rotors," in *Proceedings of the IEEE International Magnetic Conference (INTERMAG)*, 1990.
- [52] K. Muramatsu, T. Nakata, N. Takahashi and K. Fujiwara, "K. Comparison of coordinate systems for eddy current analysis in moving conductors," *IEEE Transactions on Magnetism*, 1992, 28, 1186-1189.
- [53] T. Nakata, N. Takahashi, K. Fujiwara and A. Ahagon, "Periodic boundary condition for 3-D magnetic field analysis and its applications to electrical machines," *IEEE Transactions on Magnetism*, vol. 24, pp. 2694-2696, 1988.
- [54] O. Biro, K. Preis, G. Vrisk, K. Richter and I. Ticar, "Computation of 3D magnetostatic fields using a reduced scalar potential," *IEEE Transactions on Magnetism*, vol. 24, pp. 94-97, 1988.
- [55] O. Biro, P. Böhm, K. Preis, G. Wachutka, "Edge Finite Element Analysis of Transient Skin Effect Problems," *IEEE Transactions on Magnetism*, vol. 36, pp. 835-839, 2000.
- [56] V. P Bui., Y. Le Floch, G. Meunier and J.-L. Coulomb, "A New Three-Dimensional (3-D) Scalar Finite Element Method to Compute T0", *IEEE Transactions on Magnetism*, vol. 42, pp. 1035-1038 (2006).
- [57] J. P. Webb., B. Forghani, "A single scalar potential method for 3D magnetostatics using edge elements," *IEEE Transactions on Magnetism*, vol. 25, pp. 4126-4128 (1989).
- [58] O.-M. Midtgard, R. Nilssen, "Efficient Spanning Trees for a High-Order Edge Element T- Ψ Eddy Current Formulation," *IEEE Transactions on Magnetism*, vol. 34, pp. 2652-2655 (1998).
- [59] C. N. Ashtiani and D. A. Lowther, "Simulation of the Steady-State Reactances of a Large Water-Wheel Generator by Finite Elements," *IEEE Transactions on Power Apparatus and Systems*, vol. 103, pp. 1781-1787, 1984.
- [60] R. Arumugam, D. Lowther, R. Krishnan, and J. Lindsay, "Magnetic field analysis of a switched reluctance motor using a two dimensional finite element model," *IEEE Transactions on Magnetism*, vol. 21, pp. 1883-1885, 1985.
- [61] J. Berkery, R. Barton, and A. Konrad, "Automatic finite-element grid generation for motor design analysis," *IEEE Transactions on Magnetism*, vol. 20, pp. 1924-1926, 1984.
- [62] S. Ratnajeevan, and H. Hoole, "Rotor motion in the dynamic finite element analysis of rotating electrical machinery," *IEEE Transactions on Magnetism*, vol. 21, pp. 2292-2295, 1985.
-

- [63] E. Vassent, ; G. Meunier ; A. Foggia, and J. C. Sabonnadiere, , "Simulation of induction machine operation using a step-by-step finite-element method," *Journal of Applied Physics*, vol. 67, pp. 5809-5811,1990.
- [64] Z. Cendes, D. Shenton, and H. Shahnasser, "Magnetic field computation using Delaunay triangulation and complementary finite element methods," *IEEE Transactions on Magnetics*, vol. 19, pp. 2551-255, 1983.
- [65] Z. Cendes, and D. Shenton, "Adaptive mesh refinement in the finite element computation of magnetic fields," *IEEE Transactions on Magnetics*, vol. 21, pp. 1811-1816, 1985.
- [66] B. Davat, Z. Ren, and M. Lajoie-Mazenc, "The movement in field modelling," *IEEE Transactions on Magnetics*, vol. 21, pp. 2296-2298, 1985.
- [67] A. Demenko, "Movement simulation in finite element analysis of electric machine dynamics," *IEEE Transactions on Magnetics*, vol. 32, pp. 1553-1556, 1996.
- [68] N. Sadowski, Y. Lefevre, M. Lajoie-Mazenc, and J. Cros, "Finite element torque calculation in electrical machines while considering the movement," *IEEE Transactions on Magnetics*, vol. 28, pp. 1410-1413, 1992.
- [69] T. W. Preston; A. B. J. Reece, and P. S Sangha, "Induction motor analysis by time-stepping techniques," *IEEE Transactions on Magnetics*, vol. 24, pp. 471-474, 1988.
- [70] A. Abdel-Razek, J. Coulomb, M. Feliachi, and J. Sabonnadiere, "Conception of an air-gap element for the dynamic analysis of the electromagnetic field in electric machines," *IEEE Transactions on Magnetics*, vol. 18, pp. 655-659, 1982.
- [71] M. Feliachi, J. Coulomb, and H. Mansir, "Second order air-gap element for the dynamic finite-element analysis of the electromagnetic field in electric machines," *IEEE Transactions on Magnetics*, vol. 19, pp. 2300-2303, 1983.
- [72] H. D. Gersem, and T. Weiland, "A computationally efficient air-gap element for 2-D FE machine models," *IEEE Transactions on Magnetics*, vol. 41, pp. 1844-1847, 2005.
- [73] E. Schmidt, H. D. Gersem, and T. Weiland, "Application of a computationally efficient air-gap element within the finite element analysis of magnetic bearings," *IEEE Transactions on Magnetics*, vol. 42, pp. 1263-1266, 2006.
- [74] G. D. Kalokiris, T. D. Kefalas, A. G. Kladas, and J. A. Tegopoulos, "Special air-gap element for 2-D FEM analysis of electrical Machines accounting for rotor skew," *IEEE Transactions on Magnetics*, vol. 41, pp. 2020-2023, 2005.
- [75] I. Tsukerman, "Overlapping finite elements for problems with movement," *IEEE Transactions on Magnetics*, vol. 28, pp. 2247-2249, 1992.
- [76] S. Lepaul, J. K. Sykulski, C. S. Biddlecombe, A. P. Jay, and J. Simkin, "Coupling of motion and circuits with electromagnetic analysis," *IEEE Transactions on Magnetics*, vol. 35, pp. 1602-1605, 1999.
- [77] N. Boukari, Y. Lefevre, and P. Spiteri, "Modelling the movement of electrostatic motors in a 3D finite element code," *IEEE Transactions on Magnetics*, vol. 36, pp. 722-727, 2000.
- [78] G. Krebs, S. Clénet, A. Abakar, F. Locment, and F. Piriou, "Method to Connect Nonconforming Mesh in 3-D With the Overlapping Method," *IEEE Transactions on Magnetics*, vol. 45, pp. 1420-1423, 2009.
- [79] G. Krebs, S. Clénet, and I. Tsukerman, "Overlapping Finite Elements for Arbitrary Surfaces in 3-D," *IEEE Transactions on Magnetics*, vol. 46, pp. 3473-3476, 2010.
- [80] X. Shi, Y. Le Menach, J.-P. Ducreux, and F. Piriou, "Comparison of methods to simulate the movement of electrical machine in 3D FEM," *in Proc. Compumag Conf.*, vol. 3, pp. 80, 2005.
- [81] X. Shi, Y. Le Menach, J.-P. Ducreux, and F. Piriou, "A hybrid movement method to model electrical machines with end winding in 3D Finite Element Method," *12th Biennial IEEE Conference on Electromagnetic Field Computation*, pp. 12-12, 2006.
- [82] K. Muramatsu, Y. Yokoyama, and N. Takahashi, "3D magnetic field analysis using nonconforming mesh with edge elements," *IEEE Transactions on Magnetics*, vol. 38, pp. 433-436, 2002.

-
- [83] Y. Marechal, G. Meunier, J. L. Coulomb, and H. Magnin, "A general purpose tool for restoring inter-element continuity," *IEEE Transactions on Magnetics*, vol. 28, pp. 1728-1731, 1992.
- [84] Eastham, J. F.; Balchin, M. J.; Hill-Cottingham, R. J. & Leonard, P. J. Numerical analysis techniques applied to a model iron-cored compulsator *IEEE Transactions on Magnetics*, 1995, 31, 587-592
- [85] G. Hainsworth, D. Rodger, and P. J. Leonard, "3D finite element modelling of conducting support structures in coilguns," *IEEE Transactions on Magnetics*, vol. 31, pp. 2052-2055, 1995.
- [86] H. C. Lai, P. J. Leonard, D. Rodger, N. Allen, and P. Sangha, "3D finite element dynamic simulation of electrical machines coupled to external circuits," *IEEE Transactions on Magnetics*, vol. 33, pp. 2010-2013, 1997.
- [87] D. Rodger, E. Melgoza, and H. C. Lai, "A surface impedance method for moving conductors," *IEEE Transactions on Magnetics*, vol. 36, pp. 736-740, 2000.
- [88] F. Rapetti, A. Buffa, F. Bouillault, and Y. Maday, "Simulation of a coupled magneto-mechanical system through the sliding-mesh mortar element method," *Compel- The international Journal for computation and mathematics in electrical and electronic engineering*, vol. 19, pp. 332-340, 2000.
- [89] K. Roppert, S. Schoder, F. Toth, and M. Kaltenbacher, "Non-conforming finite elements," *Newsletter Int. Compumag Society*, vol. 25, pp.4-18, 2018.
- [90] B. Cockburn, K. Guido, D. Schötzau, and C. Schwab, "Local Discontinuous Galerkin Methods for the Stokes System," *SIAM Journal on Numerical Analysis*, vol. 40, pp. 319-343, 2002.
- [91] B. Cockburn, and C.-W. Shu, "The Local Discontinuous Galerkin Method for Time-Dependent Convection-Diffusion Systems," *SIAM Journal on Numerical Analysis*, vol. 35, pp. 2440-2463, 1998.
- [92] B. Cockburn, "Discontinuous Galerkin methods for convection-dominated problems," in Barth, T and Deconink, H. (Eds), *High-Order Methods for Computational Physics*, Vol. 9 of *Lecture Notes in Computational Science and Engineering*, Springer Verlag, Berlin, pp. 69-224, 1999.
- [93] P. Castillo, B. Cockburn, I. Perugia, and D. Schötzau, "An a priori error analysis of the local discontinuous Galerkin method for elliptic problems," *SIAM Journal on Numerical Analysis*, vol. 38, pp. 1676-1706, 2000.
- [94] P. Alotto, A. Bertoni, I. Perugia, and D. Schötzau, "Efficient use of the local discontinuous Galerkin method for meshes sliding on a circular boundary," *IEEE Transactions on Magnetics*, vol. 38, pp. 405-408, 2002.
- [95] P. Alotto, A. Bertoni, I. Perugia, D. Schötzau (Schotzau), "A local discontinuous Galerkin method for the simulation of rotating electrical machines," *Compel- The international Journal for computation and mathematics in electrical and electronic engineering*, vol. 20, pp. 448-462, 2001.
- [96] E. Ferrer, R. H.J. Willden, "A high order Discontinuous Galerkin – Fourier incompressible 3D Navier–Stokes solver with rotating sliding meshes", *Journal of Computational Physics*, vol. 231, pp. 7037, 2012.
- [97] S. Straßer, H.-G. Herzog, "Interior Penalty Discontinuous Galerkin Method for Magnetostatic Field Problems in Two Dimensions," *IEEE Transactions on Magnetics*, vol. 54, pp. 1-4, 2018.
- [98] H. De Gersem, M. Ion, M. Wilke, T. Weiland, and A. Demenko, "Trigonometric interpolation at sliding surfaces and in moving bands of electrical machine models," *COMPEL-The international journal for computation and mathematics in electrical and electronic engineering*, vol. 25, pp. 31-42, 2006.
- [99] E. Lange, F. Henrotte, and K. Hameyer, "Biorthogonal shape functions for nonconforming sliding interfaces in 3-D electrical machine FE models with motion," *IEEE Transactions on Magnetics*, vol. 48, pp. 855-858, 2012.
-

- [100] S. Böhmer, C. Krüttgen, B. Riemer, K. Hameyer, "Eddy currents and non-conforming sliding interfaces for motion in 3-D finite element analysis of electrical machines," *IEEE Transactions on Magnetics*, vol. 51, pp. 1-4, 2015.
- [101] S. Boehmer, E. Lange, and K. Hameyer, "Non-conforming sliding interfaces for relative motion in 3D finite element analysis of electrical machines by magnetic scalar potential formulation without cuts," *IEEE Transactions on Magnetics*, vol. 49, pp. 1833-1836, 2013.
- [102] F. Piriou, A. Razek, "A model for coupled magnetic-electric circuits in electrical machines with skewed slots", *IEEE Transactions on Magnetics*, vol. 26, pp. 1096-1100, 1990.
- [103] G. C. Hsiao, and W. L. Wendland, "Boundary integral equations," *Applied Mathematical Sciences*, Springer, 2008.
- [104] L. Kielhorn, T. Rüberg, and J. Zechner, "Simulation of electrical machines: a FEM-BEM coupling scheme," *COMPEL - The international journal for computation and mathematics in electrical and electronic engineering*, vol. 36, pp. 1540-1551, 2017.
- [105] R. Hiptmair, "Finite elements in computational electromagnetism," *Acta Numerica*, Cambridge University Press, vol. 11, pp. 237–339, 2002.
- [106] R. Hiptmair, "Symmetric Coupling for Eddy Current Problems," *SIAM Journal on Numerical Analysis*, vol. 40, pp. 41-65, 2002.

List of Publications

- [P1] G. J. Wallinger, O. Biro, "A coupling method for nonconforming meshes in the 3D FEM analysis of static fields," in *Proceedings of the 16th IGTE symposium on Numerical Field Calculation in Electrical Engineering*, pp.54, 2014.
- [P2] G. J. Wallinger, and O. Biro, "3D FEM analysis of static fields for non-conforming meshes with 2nd order node-based elements," in *Proceedings of the Conference on the Computation of Electromagnetic Fields (Compumag 2015)*.
- [P3] G. J. Wallinger, and O. Biro, "3D FEM analysis of static fields for non-conforming meshes with 2nd order node-based elements," *IEEE Transactions on Magnetics*, vol. 52, 2016, 1-4.
- [P4] G. J. Wallinger, O. Biro, "Periodic boundary conditions for 3D FEM using a non-conforming mesh," in *Proceedings of the 17th IGTE symposium on Numerical Field Calculation in Electrical Engineering* 2016.
- [P5] G. J. Wallinger and O. Bíró, "Comparison of two formulations taking account of 3D motion induced eddy currents," in *Proceedings of the 17th Biennial IEEE Conference on Electromagnetic Field Computation (CEFC)*, 2016.
- [P6] G. J. Wallinger and O. Bíró, "Non-conforming finite element method to simulate eddy currents due to motion using the $T, \Phi - \Phi$ formulation," in *Proceedings of the IEEE International Magnetic Conference (INTERMAG)*, 2018.
- [P7] G. J. Wallinger, O. Biro, "Calculation of motion induced eddy currents, utilizing the $T, \Phi - \Phi$ formulation," in *Proceedings of the 18th IGTE symposium on Numerical Field Calculation in Electrical Engineering* 2018.
- [P8] G. J. Wallinger and O. Bíró, "Improved coupling strategy to cover curved FE-facets in the non-conforming mesh method," in *Proceedings of the 18th Biennial IEEE Conference on Electromagnetic Field Computation (CEFC)*, 2018.
- [P9] G. J. Wallinger and O. Bíró, "An approach to calculate the source field of complex conductor structures," in *Proceedings of the International Symposium on Electromagnetic Phenomena in Nonlinear Circuits (EPNC)*, 2016.
- [P10] G. J. Wallinger and O. Bíró, "Improved coupling strategy to cover curved FE-facets in the non-conforming mesh method," *IEEE Transactions on Magnetics*, to be published, 2019.

List of figures

- Fig. 1: Illustration of a conducting domain ($\sigma \neq 0$) moving with velocity \mathbf{v} in a homogeneous (a) and inhomogeneous (b) magnetic field. 15
- Fig. 2: If a conducting domain ($\sigma \neq 0$) is exposed to a time varying magnetic field, eddy currents \mathbf{J}_{eddy} will flow in the conducting material causing a magnetic field \mathbf{B}_{eddy} . This field is then counteracting to the change of the exciting magnetic field. 16
- Fig. 3: Generalized topology of a magneto-static problem..... 17
- Fig. 4: Generalized topology for a quasi-static eddy current problem. 19
- Fig. 5: Different types of linear elements, regarding to the dimensionality of the considered problem. a) 1D line element b) 2D triangle element c) 2D quadrilateral element d) 3D tetrahedral element e) 3D triangular prism f) 3D hexahedral element. 23
- Fig. 6: Classification into nodal or edge based, second order hexahedral elements. a) Nodal finite element with 20 nodes. b) Hybrid finite element with $n_e=36$ edges (1 to 36) and $n_n=20$ nodes (37 to 56)..... 25
- Fig. 7: Illustration of the nodal shape functions N_i in case of three different node locations. a) 3D surface view of a left corner node: $N_1(-1,-1,-1) = 1$ b) 3D surface view of a side middle node: $N_2(0,-1,-1) = 1$ c) 3D surface view of a corner node $N_3(1,-1,-1) = 1$ d) Shape functions N_1, N_2 and N_3 along the local coordinate ξ , while keeping the other coordinates constant: $\eta = \zeta = -1$ 26
- Fig. 8: Illustrative, two dimensional example of a non-conforming finite element mesh with quadrilateral elements. The overall mesh is allowed to be non-conforming with hanging nodes along the sliding surface Γ_S . Master and slave nodes, m_i and s_k can be defined along Γ_S 35
- Fig. 9: Coupling situation of a slave node s_k in case of a two dimensional non-conforming mesh. a) Global position of the slave node at its space coordinates \mathbf{r}_k . b) Localisation of the slave node within the local coordinate system of the master element..... 36
- Fig. 10: Coupling coefficients and shape functions of corresponding master nodes in case of slave node s_k located at $\xi=0.6$ and $\eta=-1$ 36
- Fig. 11: Coupling situation in case of 3D problems. a) Non-conforming mesh along the sliding surface Γ_S . b) Top view of the coupling situation for two slave nodes in detail at the sliding surface..... 37
- Fig. 12: Problem model for the error analysis. a) 3D view of the cylindrical model with the non-matching meshes. b) Detailed view of the non-conforming mesh with equidistant elements along the sliding surface..... 42
- Fig. 13: Different mesh topologies considered for the error analysis. a) Equal number of elements in the two domains Ω_1 and Ω_2 . b) Different number of elements in the two domains Ω_1 : $2n$ and Ω_2 : n c) Different number of elements in the two domains Ω_1 : $3n$ and Ω_2 : n 42
- Fig. 14: Comparison of the magnetic scalar potential. a) conforming mesh b) non-conforming mesh with equal number of elements in both domains Ω_1 and Ω_2 43
- Fig. 15: Comparison of the magnetic scalar potential in case of different number of elements in both domains Ω_1 and Ω_2 . a) $\Omega_1: 2n$ and $\Omega_2: n$ b) $\Omega_1: 3n$ and $\Omega_2: n$ 44
- Fig. 16: Numerical values of the magnetic scalar potential along the circular line with radius $R_2=0.569m$ for $n=400$ elements. a) Comparison of the analytical solution with the non-conforming case with equal number of elements in both domains Ω_1 and Ω_2 .

- b) Numerical values obtained in the two cases with different number of elements in the two domains. First, $\Omega_1:2n$ and $\Omega_2:n$ (numerical $2n$) and second $\Omega_1:3n$ and $\Omega_2:n$ (numerical $3n$)..... 44
- Fig. 17: Error plotted as a function of the number of elements in logarithmic scale, both at R_1 (solid lines) and R_2 (dashed lines). The case of $\alpha=0$ corresponds to a conforming mesh, $\alpha=1.0$ to a maximally non-conforming one. The convergence rate indicated by all curves is almost the same with a slope close to -2 , indicating quadratic convergence..... 45
- Fig. 18: Error depending on the ratio δ between the number of elements n_{EL}^{master} in the master domain to n_{EL}^{slave} in the slave domain. In case of the ratio of mesh density is $\delta < 1.4$, reliable solutions can be obtained. If the ratio is increased further, incorrect solutions are obtained. Therefore it is suggested to use a ratio of $0.1 \leq \delta < 1.4$ 46
- Fig. 19: A detailed plot of the error ε_n depending on the ratio of mesh density. Apparently, the error is smallest if the ratio is near to one. As in detail shown, the error decreases in quadratic manner when increasing the number of elements. 47
- Fig. 20: Error depending on the relative movement between the domains Ω_1 and Ω_2 . The error is shown in the case of domain Ω_2 with radius R_1 48
- Fig. 21: Error depending on the relative movement between the domains Ω_1 and Ω_2 . The error is shown in the case of domain Ω_1 with radius R_2 48
- Fig. 22: Comparison of the distribution of the non-zero entries in the system matrix in case of a non-conforming and a conforming mesh. a) System matrix of the non-conforming mesh with a detail view of the main diagonal. b) System matrix in case of a conforming mesh. c) Additional coupling coefficients (non-zeros)..... 49
- Fig. 23: Illustration of (anti-) periodic boundary conditions in case of moving domains..... 51
- Fig. 24: Problem model of a rotating machine with six poles. a) 3D view of one-sixth of the machine with 60-degree azimuthal periodicity. b) Top view of the problem with (anti-) periodic boundary conditions. 51
- Fig. 25: Comparison of the magnetic flux density $|\mathbf{B}|$. a) Non-conforming mesh b) Conforming mesh 52
- Fig. 26: Comparison of numerical values calculated along a curved line with radius $R=0.09m$ and azimuthal range of 60 degrees. a) Magnetic flux density $|\mathbf{B}|$ b) Magnetic field intensity $|\mathbf{H}|$ 53
- Fig. 27: Conductor moving in the global coordinate system S at a velocity \mathbf{v} for a certain time Δt . The finite elements of the conductor are exposed to a change of the magnetic flux density. 56
- Fig. 28: Planar problem model to consider motion induced eddy currents. The dimensions of the iron plate are defined as $l_{plate}=3m$, $w_{plate}=1m$ and $d_{plate}=0.01m$. The cross section of the conductors is defined by $w_{cond}=5mm$ and $h_{cond}=41mm$. The two conductors are displaced to each other by $d_{cond}=20mm$ and the air gap between the conductors and iron plate is set to $d_A=1mm$ 60
- Fig. 29 Impressed current density $\mathbf{J}(t)$ is assumed to be a step function with ramp..... 61
- Fig. 30: Comparison of the current density in case of a coarse mesh with $n_E=600$ elements along the sliding surface. 62
- Fig. 31: Comparison of the current density in case of a fine mesh with $n_E=3000$ elements along the sliding surface..... 63

List of figures

Fig. 32: Comparison of the current density in case of $n_E=3000$ elements along the sliding surface and at last time step $t=48ms$ 64

Fig. 33: Comparison of the magnetic flux density in case of $n_E=3000$ elements along the sliding surface and at last time step $t=48ms$ 64

Fig. 34: Field plot of the induced eddy current in the iron plate. a) Current density in case of the stationary solution b) Current density in case of the transient solution with a non-conforming mesh along the sliding surface flowing the last time step at $t=48ms$ 65

Fig. 35: Field plot of the magnetic flux density in the iron plate. a) Magnetic flux density in case of the stationary solution b) Magnetic flux density in case of the transient solution with a non-conforming mesh along the sliding surface following the last time step at $t=48ms$ 65

Fig. 36: Model of a problem consisting of a copper shell with a cylindrical coil settled in the centre of the annulus. a) Top view with dimensions b) 3D view with symmetry plane at the bottom. 66

Fig. 37: Mesh topology with equal mesh density in both domains, stationary and moving. a) Top view of the mesh b) Front view of the mesh along the z-axis. 68

Fig. 38: Comparison of the current density for different time steps in case of $n_{EL}=40$ equidistant elements along the sliding surface. 70

Fig. 39: Comparison of the current density for different time steps in case of $n_{EL}=80$ and $n_{EL}=120$ equidistant elements along the sliding surface. 70

Fig. 40: Comparison of the magnetic flux density for different time steps in case of $n_{EL}=40$ (see a) and in case of $n_{EL}=80$ and $n_{EL}=120$ (see b). 71

Fig. 41: Time transient evolution of the magnetic flux density $|\mathbf{B}|$ on the left and of the current density $|\mathbf{J}|$ on the right. 73

Fig. 42: Mesh topology with different mesh density in both domains, stationary and moving. a) Overview of the mesh at the point of interest b) Detailed view of the mesh along the sliding surface. 74

Fig. 43: Comparison of the current density in case of different mesh topologies in the two domains Ω_{stat} and Ω_{mov} 75

Fig. 44: Comparison of the magnetic flux density in case of different mesh topologies in the two domains Ω_{stat} and Ω_{mov} 75

Fig. 45: Two disjoint domains Ω^M and Ω^S with non-conforming mesh along the sliding surface Γ_S . Master nodes m_l and slave nodes s_k can be defined along the interface Γ_S . 76

Fig. 46: Front view of two disjoint domains, showing in detail the problem of geometrical errors like small gaps and overlaps between the elements facets, in case of two elements displaced relatively to each other. 77

Fig. 47: Illustrative example to consider different slave node locations and different number of corresponding master nodes. a) Conventional approach with $L_k^{(master)} = 8$ b) New approach with $L_k^{(master)} = 20$ 78

Fig. 48: Stiffness of coupling dependent only on the local coordinate ζ for the cases of $L_k^{(master)} = 8$ and $L_k^{(master)} = 20$ corresponding master nodes. 79

Fig. 49: Comparison of the current density for the conventional (old) and new coupling approach, $L_k^{(master)} = 8$ and $L_k^{(master)} = 20$ per element. 80

-
- Fig. 50: Detailed view of the comparison of the current density at steady state for the conventional (old) and new coupling approach, $L_k^{(master)} = 8$ and $L_k^{(master)} = 20$ per element..... 81
- Fig. 51: Stiffness of coupling averaged over the period of time for the old and new coupling approaches, $L_k^{(master)} = 8$ and $L_k^{(master)} = 20$ at equal mesh density in Ω_{stat} and Ω_{mov} 82
- Fig. 52: Stiffness of coupling averaged over the period of time for the old and new coupling approaches, $L_k^{(master)} = 8$ and $L_k^{(master)} = 20$ at different mesh densities in Ω_{stat} and Ω_{mov} 82
- Fig. 53: Illustration of an arbitrary shaped conductor getting mapped onto the problem domain Ω . The current density \mathbf{J}_0 at integration points within the conductor domain Ω_c becomes \mathbf{J}_c , otherwise the current density \mathbf{J}_0 is zero. 87
- Fig. 54: Numerical example: a) Helical conductor within a hexahedral finite element mesh. b) Detailed view of the helical conductor showing the two data lines, parallel to the x and z-axis, respectively. 88
- Fig. 55: a) Current density of the hexahedral mesh. b) Convergence time behaviour of the incomplete Cholesky preconditioned conjugate gradient method according to the degree of freedom. 89
- Fig. 56: a) Current density \mathbf{J}_0 on the hexahedral mesh taken along *line 1*. b) Current density \mathbf{J}_0 on the hexahedral mesh taken along *line 2*..... 90

List of tables

Tab. 1: Electromagnetic field equations, the so-called Maxwell's equations in two ways of formulations, differential and integral. The boundary of the surface Γ is denoted by $\partial\Gamma$, $\partial\Omega$ denotes the bounding surface of the volume Ω and \mathbf{n} denotes the surface normal vector pointing outward of closed surfaces.....	13
Tab. 2: Summary of the equations and boundary conditions for the magneto-static boundary value problem.	18
Tab. 3: Summary of the equations and boundary conditions for the quasi-static, boundary value problem.	19
Tab. 4: Summary of the magneto-static boundary value problem in terms of the scalar potential Φ and the current vector potential \mathbf{T}_0	30
Tab. 5: Eddy current boundary value problem in terms of the $\mathbf{A}, \mathbf{V}-\mathbf{A}$ formulation. Here, the normal component of the magnetic flux density \mathbf{B} is prescribed by the tangential component of the magnetic vector potential \mathbf{A} . The outward surface normal vector of the conducting domain and non-conducting domain are related as $\mathbf{n}_c = -\mathbf{n}_n$..	32
Tab. 6: Eddy current boundary value problem in terms of the $\mathbf{T}, \Phi-\Phi$ formulation.	33
Tab. 7 Dimensions of the cylindrical problem.	66
Tab. 8: Stiffness of coupling in case of the conventional approach where the number of master nodes is set to $L_k^{(master)} = 8$, and in case of the new approach where the number of master nodes is set to $L_k^{(master)} = 20$	78
Tab. 9: Convergence behaviour depending on the number of degrees of freedom and number of elements.	89